

Dissertation
submitted to the
Combined Faculty of Mathematics, Engineering and Natural
Sciences
of Heidelberg University, Germany
for the degree of
Doctor of Natural Sciences

Put forward by
Brooke Polak
Born in: Winfield, Illinois, USA
Oral examination: 17.10.2024

THE SECRET LIVES OF YOUNG MASSIVE STAR CLUSTERS

BROOKE POLAK

REFEREES:

PROF. DR. RALF S. KLESSEN

PRIV. DOZ. DR. GENEVIÈVE PARMENTIER

Brooke Polak: *The Secret Lives of Young Massive Star Clusters*, © October 2024

ABSTRACT

Many aspects of star cluster formation and evolution are unconstrained. This thesis presents models of star cluster formation — including gas and stellar dynamics, sub-grid star formation, stellar evolution, and stellar feedback — from turbulent gas clouds of initial mass 10^4 , 10^5 , and $10^6 M_{\odot}$. The latter is one of the largest star-by-star cluster models to date and has provided many new insights into the formation and early evolutionary properties of young massive star clusters. First, I examine the global properties of each cloud, particularly noting the high star formation efficiency. In sufficiently dense and massive clusters, stellar feedback is unable to quench star formation as gravity overpowers it. Next, I identify a novel mechanism for the production of runaway stars in young clusters, the sub-cluster ejection scenario, in which a subset of stars in an infalling sub-cluster are ejected by a tidal interaction with the assembling cluster's center of mass. Lastly, I analyze the presence of dynamical mass segregation in the models, where massive stars are more centrally clustered than low-mass stars. These models have no primordial mass segregation by construction. Young clusters can undergo early dynamical mass segregation during core collapse when the crossing time is substantially reduced.

ZUSAMMENFASSUNG

Viele Aspekte der Sternhaufenbildung und -entwicklung sind noch ungeklärt. In dieser Dissertation präsentiere ich Modelle der Sternhaufenbildung, unter Berücksichtigung der Gas- und Stelldynamik, Sternentstehung und Sternentwicklung, und realistischer Modelle für stellares Feedback. Ich betrachte turbulente Gaswolken mit anfänglichen Massen von 10^4 , 10^5 und $10^6 M_{\odot}$. Letztere ist eine der größten Rechnungen in dieser Klasse und erlaubt viele neue Einblicke in die Bildung und frühen Entwicklungseigenschaften junger massereicher Sternhaufen. In der hier vorgelegten Arbeit untersuche ich zunächst die globalen Eigenschaften jeder Wolke, insbesondere die Sternentstehungseffizienz. In ausreichend dichten und massereichen Haufen ist stellares Feedback nicht in der Lage, die Sternentstehung zu unterdrücken, da die Eigengravitation überwiegt. Als nächstes identifiziere ich einen neuartigen Mechanismus zum Auswurf von Sternen in jungen Haufen, das Subcluster-Ejektionszenario, bei dem eine Untergruppe von Sternen in einem einfallenden Subcluster durch Gezeitenwechselwirkung mit dem Massenschwerpunkt des sich bildenden Haufens ausgeworfen wird. Schließlich analysiere ich die Eigenschaften der dynamischen Massen-Segregation, bei der massereiche Sterne stärker als massearme Sterne im Zentrum konzentriert sind. Die hier betrachteten Modelle haben von Anfang an keine primordiale Massen-Segregation, allerdings können junge Haufen während des Kernkollapses eine frühe Phase der Massen-Segregation durchlaufen, wenn die dynamische Zeitskala erheblich verkürzt ist.

ACKNOWLEDGMENTS

Above all, I am deeply grateful to my thesis advisors, Ralf Klessen and Mordecai-Mark Mac Low. Writing this thesis was cathartic, and it made me realize how much I've grown as a scientist under their guidance. I have learned so much from them, and because of that I can confidently spread my wings as an independent researcher. I'm also thankful to Simon Portegies Zwart and Simon Glover for their advice and invaluable scientific input.

This thesis wouldn't be possible without the support from the rest of the Torch team: Claude Cournoyer-Cloutier, Eric Andersson, Sabrina Appel, Aaron Tran, Sean Lewis, and Maite Wilhelm. The few times we got together were delightful, and working with them has made for a great and supportive atmosphere.

I am thankful for the endless love and support from my family. Thank you to my mom, my dad, and my stepdad Randy for always telling me how proud they are of me. I would like to thank my brother Kyle for always putting a smile on my face and a cold beer in my hand. I also want to thank my twin sister and best friend Paige for the daily phone calls, and for always being there for me since we were wombmates. I know I can always count on you, and for that I am forever grateful.

A special thanks to my friends Mary Budz and Maddie Corgiat. Mary has been inflating my ego since elementary school, and I couldn't be more grateful for her. Thank you for visiting me no matter where I move to and for the best memories. Maddie, I have you and our daily facetimes to thank for my sanity in lockdown Germany, without which, I wouldn't have survived. Thank you for the endless laughs.

Most of all, I want to thank my husband Jack for the perpetual love and support. Even when I'm the most stressed, you always find a way to make me forget my worries and enjoy life. Most importantly, thank you for always waking me up with a fresh iced coffee. I couldn't have done this without you.

PUBLICATIONS

The following publications are used in this thesis:

- I. *Massive Star Cluster Formation I. High Star Formation Efficiency While Resolving Feedback of Individual Stars*, A&A, accepted (2023), **Brooke Polak**, Mordecai-Mark Mac Low, Ralf S. Klessen, Jia Wei Teh, Claude Cournoyer-Cloutier, Eric P. Andersson, Sabrina M. Appel, Aaron Tran, Sean C. Lewis, Maite J.C. Wilhelm, Simon Portegies Zwart, Simon C.O. Glover, Steven Rieder, Long Wang, Stephen L.W. McMillan
- II. *Massive Star Cluster Formation II. Runaway Stars as Fossils of Sub-Cluster Mergers*, A&A, accepted (2024), **Brooke Polak**, Mordecai-Mark Mac Low, Ralf S. Klessen, Simon Portegies Zwart, Eric P. Andersson, Sabrina M. Appel, Claude Cournoyer-Cloutier, Simon C.O. Glover, and Stephen L.W. McMillan
- III. *Massive Star Cluster Formation III. Early dynamical mass segregation during cluster assembly*, A&A, submitted (2024), **Brooke Polak**, Mordecai-Mark Mac Low, Ralf S. Klessen, Simon Portegies Zwart, Eric P. Andersson, Sabrina M. Appel, Claude Cournoyer-Cloutier, Simon C.O. Glover, and Stephen L.W. McMillan

CONTENTS

| | | |
|-----------|--|-----------|
| I | STAR CLUSTER FORMATION THEORY | 1 |
| 1 | FUNDAMENTALS OF STAR CLUSTER FORMATION AND EVOLUTION | 3 |
| 1.1 | Introduction | 3 |
| 1.2 | Star Clusters | 6 |
| 1.2.1 | Formation | 6 |
| 1.2.2 | Properties | 9 |
| 1.3 | The interstellar medium | 10 |
| 1.3.1 | Composition | 11 |
| 1.3.2 | Thermal phases | 11 |
| 1.3.3 | Heating & Cooling | 12 |
| 1.3.4 | Turbulence & Gravity | 13 |
| 1.3.5 | Formation of GMCs | 14 |
| 1.3.6 | GMC Properties | 14 |
| 1.4 | Star formation in GMCs | 15 |
| 1.4.1 | Collapse conditions | 15 |
| 1.4.2 | Stellar initial mass function | 17 |
| 1.4.3 | Stellar evolution | 17 |
| 1.4.4 | Stellar feedback | 18 |
| 2 | SIMULATING STAR CLUSTER FORMATION | 21 |
| 2.1 | Introduction | 21 |
| 2.2 | Gas | 22 |
| 2.2.1 | Hydrodynamics | 22 |
| 2.2.2 | Gravity | 23 |
| 2.2.3 | Heating and cooling | 24 |
| 2.3 | Stars | 24 |
| 2.3.1 | Sub-grid star formation | 24 |
| 2.3.2 | Stellar Dynamics | 26 |
| 2.3.3 | Stellar evolution | 27 |
| 2.4 | Gas-star coupling | 28 |
| 2.4.1 | Gravity bridge | 28 |
| 2.4.2 | Stellar feedback | 28 |
| II | PUBLICATIONS | 31 |
| 3 | HIGH STAR FORMATION EFFICIENCY WHILE RESOLVING FEEDBACK OF INDIVIDUAL STARS | 33 |
| 3.1 | Abstract | 33 |
| 3.2 | Introduction | 33 |
| 3.3 | Methods | 37 |
| 3.3.1 | Standard TORCH | 37 |
| 3.3.2 | PETAR N-body | 38 |
| 3.3.3 | Stellar modifications | 40 |

| | | | |
|-------|--|-----|-----|
| 3.3.4 | Initial conditions | 41 | |
| 3.4 | Results | 45 | |
| 3.4.1 | Cluster formation overview | 45 | |
| 3.4.2 | Visualizing cluster morphology | 46 | |
| 3.4.3 | Star formation history | 47 | |
| 3.4.4 | Cluster evolution | 50 | |
| 3.5 | Discussion | 52 | |
| 3.5.1 | Limitations of comparing observed and modelled star formation efficiencies | 52 | |
| 3.5.2 | Observations | 53 | |
| 3.5.3 | Other simulations | 57 | |
| 3.6 | Conclusions | 61 | |
| 3.7 | Acknowledgements | 63 | |
| 3.8 | Data Availability | 64 | |
| 3.9 | appendix | 64 | |
| 3.9.1 | Stellar properties: Physical times | 64 | |
| 3.9.2 | Stellar modifications | 64 | |
| 4 | RUNAWAY STARS AS FOSSILS OF SUB-CLUSTER MERGERS | | 73 |
| 4.1 | Abstract | 73 | |
| 4.2 | Introduction | 73 | |
| 4.3 | Results | 75 | |
| 4.4 | Discussion | 84 | |
| 4.4.1 | Persistence of runaway groups through projection effects | 84 | |
| 4.4.2 | Fossils of cluster assembly history | 84 | |
| 4.4.3 | Observational examples | 85 | |
| 4.4.4 | Runaway binary stars | 86 | |
| 4.4.5 | Importance of initial conditions | 89 | |
| 4.4.6 | High peak stellar density | 90 | |
| 4.5 | Conclusions | 92 | |
| 4.6 | Acknowledgements | 93 | |
| 5 | EARLY DYNAMICAL MASS SEGREGATION DURING CLUSTER ASSEMBLY | | 95 |
| 5.1 | Abstract | 95 | |
| 5.2 | Introduction | 95 | |
| 5.3 | Results | 97 | |
| 5.4 | Discussion | 101 | |
| 5.4.1 | Time Scales | 101 | |
| 5.4.2 | Observational comparisons | 104 | |
| 5.5 | Conclusions | 106 | |
| 5.6 | Acknowledgements | 108 | |
| III | SUMMARY & FUTURE WORK | | 109 |
| 6 | SUMMARY & FUTURE WORK | | 111 |
| 6.1 | Summary | 111 | |
| 6.2 | Future Work | 113 | |

| | | |
|-------|--------------------------------------|-----|
| 6.2.1 | Towards realistic initial conditions | 113 |
| 6.2.2 | Efficient radiation transfer | 113 |
| 6.2.3 | Long-term dynamical evolution | 113 |

| | |
|--------------|-----|
| BIBLIOGRAPHY | 115 |
|--------------|-----|

LIST OF FIGURES

- Figure 1 Images showing each type of star cluster: the open cluster Pleiades in the Milky Way, the young massive cluster R136 in the 30 Dor H II region in the LMC, and the Milky Way globular cluster 47 Tucanae. *Credits: Davide De Martin, the ESA/ESO/NASA Photoshop FITS Liberator (Pleiades); NASA, ESA, CSA, STScI, Webb ERO Production Team (30 Dor); NASA, ESA/Hubble Heritage (47 Tuc).* 4
- Figure 2 Overview of the star cluster formation process. The colored surfaces represent gas in a molecular cloud of increasing density from blue to pink, with star forming gas in hot pink. The white dots are stars. 1. During global gravitational collapse of the cloud, turbulence creates a hierarchical structure of overdense filaments. 2. The overdense filaments collapse faster than the global cloud, creating sub-clusters tracing the dense substructure. 3. The sub-clusters dynamically merge to the center of mass and form a single star cluster. 4. The combined feedback of the star cluster eventually expels the unused gas. While this diagram is purely illustrative, the colored surfaces trace the gas from a star cluster formation simulation presented in this thesis. 7
- Figure 3 The Pillars of Creation (the Eagle nebula) images taken by JWST in mid-infrared (5.6-25.5 μm), and near-infrared (0.6-5.0 μm). Mid-infrared radiation is opaque to dust, so in the MIRI image we see the structure of the dense molecular gas. Near-IR is transparent to dust, and this wavelength reveals the prolific formation of young stars within the pillars. *Credit: NASA, ESA, CSA, STScI.* 8

- Figure 4 Measured values of the median mass and half-mass radius of clusters in the Milky Way and local galaxies. Error bars indicate the 16th and 84th percentiles. Lines of constant density $\rho(M_{\odot} \text{ pc}^{-3}) = 3M/8\pi R_{\text{hm}}^3$ and surface density $\Sigma(M_{\odot} \text{ pc}^{-2}) = M/2\pi R_{\text{hm}}^2$ are plotted as dashed and dotted lines, respectively. Data taken from Table 3 in Krumholz et al. (2019). 11
- Figure 5 Wall-clock time for an evolution step for PETAR and PH4+MULTIPLES given the number of stars. 39
- Figure 6 Slice plots of the three simulations in the x - y plane over time. The plane of the slices for a given cloud is the center of stellar mass in the final snapshot. Stellar positions are shown by white dots. The free-fall times t_{ff} are given in Table 3. The number of stars shows the amount of star particles in the domain, not the number sampled from the IMF. Due to our agglomeration of low-mass star particles, the number of stars sampled from the IMF is $\sim 10\times$ greater. 42
- Figure 7 Still of the interactive plot of the embedded M4, M5, and M6 clusters (left to right) at $1 t_{\text{ff}}$. The interactive plot file is available for download from the repository. 47

- Figure 8 Global properties of the clusters and gas over time for models M4 (*orange*), M5 (*maroon*), and M6 (*blue-violet*) in units of free-fall time t_{ff} of the initial cloud (given in Table 3). From top left to bottom right: (a) SFR, where the transparent lines show the SFR at each star formation event, and the solid lines give the SFR smoothed using a Gaussian filter with $\sigma = 0.005t_{\text{ff}}$. (b) Instantaneous and integrated SFEs of the clouds, where $\epsilon_{\text{inst}} = M_{\star}/(M_{\text{gas}} + M_{\text{sink}} + M_{\star})$ and $\epsilon_{\text{int}} = M_{\star}/M_{\text{cloud}} = \epsilon_{\star}$. (c) Most massive star formed. (d) Number of formed stars. *Dashed line*: actual number of stars that would form from sampling the IMF given the amount of gas mass collected for star formation by sink particles. *Solid line*: number of stars followed in TORCH after the sampled stellar population below $4 M_{\odot}$ has been agglomerated. *Dotted line*: number of stars above $20 M_{\odot}$ on the grid that are generating feedback. The number of stars can drop due to SN, mass loss, or exiting the grid. (e) 3D stellar velocity dispersion. (f) Half-mass radius of the entire star cluster. (g) Total mass (*dotted line*), mass of stars (*dashed line*) and gas (*solid line*) on the grid. (h) Virial parameter of stars (*dashed line*) and gas (*solid line*), where $\alpha_v = 0.5$ is the equilibrium value. (i) Fraction of mass bound for stars (*dotted line*) and gas (*solid line*). 48
- Figure 9 Size-line width coefficient versus surface density for the Firecracker cloud (Finn et al., 2019) and the M4, M5, and M6 clouds. The four red diamonds are observations, done using apertures (1–4) with radii $R = 6.4, 15, 26,$ and 37 pc. The other points are our simulations, with connected points corresponding to apertures (1–4) of radii $R = 5, 10, 15$ and 20 pc. The colors indicate how much stellar mass has been produced (with empty points indicating no star formation). The lines correspond to virial equilibrium and free-fall as labeled (see Fig. 2 of Ballesteros-Paredes et al., 2011). 56

- Figure 10 WARPFIELD evolution of shell radius versus time with different initial SFEs with the same parameters described in M6. In all cases, stellar feedback is inefficient in dispersing the surrounding dense cloud, and the shell eventually undergoes re-collapse. 60
- Figure 11 Global properties of the clusters and gas over time for models M4 (*orange*), M5 (*maroon*), and M6 (*blue-violet*) for comparison to Figure 8, where units of free-fall time (see Table 3) are used. From top left to bottom right: (a) SFR, where the transparent lines show the SFR at each star formation event, and the solid lines give the SFR smoothed using a Gaussian filter with $\sigma = 0.005t_{\text{ff}}$. (b) Instantaneous and integrated SFEs of the clouds, where $\epsilon_{\text{inst}} = M_{\star}/(M_{\text{gas}} + M_{\text{sink}} + M_{\star})$ and $\epsilon_{\text{int}} = M_{\star}/M_{\text{cloud}} = \epsilon_{\star}$. (c) Most massive star formed. (d) Number of formed stars. *Dashed line*: actual number of stars that would form from sampling the IMF given the amount of gas mass collected for star formation by sink particles. *Solid line*: number of stars followed in TORCH after the sampled stellar population below $4 M_{\odot}$ has been agglomerated. *Dotted line*: number of stars above $20 M_{\odot}$ on the grid that are generating feedback. The number of stars can drop due to SNe, mass loss, or exiting the grid. (e) 3D stellar velocity dispersion. (f) Half-mass radius of the entire star cluster. (g) Total mass (*dotted line*), mass of stars (*dashed line*) and gas (*solid line*) on the grid. (h) Virial parameter of stars (*dashed line*) and gas (*solid line*), where $\alpha_v = 0.5$ is the equilibrium value. (i) Fraction of mass bound for stars (*dotted line*) and gas (*solid line*). 65
- Figure 12 Fraction of the number of stars formed with agglomeration of stars below the mass on the x-axis over the total number of stars sampled by the IMF. We used $M_{\text{agg}} = 4 M_{\odot}$, which means the number of stars in the grid is 10% of the number that are formed by our IMF. 66
- Figure 13 Power of stellar feedback in the form of winds and FUV and EUV radiation for different stellar masses. Left of the vertical line shows the amount of feedback power lost per star by excluding feedback from stars below $20 M_{\odot}$. 68

- Figure 14 Power output of stellar feedback modes for each stellar mass regime. (*Top left*): Histogram showing the fractional stellar population of the three runs at one free-fall time, split into the mass regimes of 8–20 and 20–100 M_{\odot} . (*Top right*): Fraction of feedback power in each mass regime. (*Bottom*): Histograms showing the fraction of feedback power for FUV, EUV, and winds in each mass regime. Although there are more lower-mass stars, the feedback produced by them is less than 20% of the total feedback energy for all stars. 68
- Figure 15 Star formation efficiency over time for the fiducial M6 cloud with $T_w = 300,000$ K and $M_{\text{feedback}} \geq 20 M_{\odot}$ (*cool winds*), the M6 cloud with $T_w = 5,000,000$ K and $M_{\text{feedback}} \geq 20 M_{\odot}$ (*hot winds*), and the M6 cloud with $T_w = 5,000,000$ K and $M_{\text{feedback}} \geq 8 M_{\odot}$ (*hot winds, $M_{\text{fb}} = 8 M_{\odot}$*). 70
- Figure 16 Ejection velocity angular directions of M6 runaways stars with $\theta_{\vec{v}}$ and $\phi_{\vec{v}}$ binned in 9° and 18° angle bins, respectively. There are two distinctly peaked angular regions which are labeled as group 1 and group 2. The rectangles indicate the angular bins of runaways we selected for trajectory analysis. 76
- Figure 17 Mollweide map projection of the ejection directions of the runaway stars in M6. The colors correspond to (*top*) radial velocity from the cluster center of mass, (*middle*) star mass, and (*bottom*) star age. The highest values are plotted over lower values for visibility. 77
- Figure 18 Scatter plot of the runaway stars, showing the radial velocity and age colored by mass. Squares are group 1, diamonds are group 2, and dots are the rest of the runaways. These groups are the runaways selected by ejection direction only. The two groups are distinctly separate in both age and velocity. Group 2 contains two sub-groups ejected in the same direction but at slightly different times. For the purpose of demonstrating the SCES mechanism, we focus on the later forming sub-group in group 2. The red rectangles indicate the additional filtering of the runaway groups by age and velocity. 78

- Figure 19 Particle mass distributions of the entire star cluster (*grey*) and the runaway groups along with the Kroupa IMF power-law. Note that at the low-mass ($\leq 8M_{\odot}$) end, the particle masses are skewed higher than the sampled IMF due to the agglomeration of stars below $< 4M_{\odot}$. [79](#)
- Figure 20 (Movie online) Movie of the formation and ejection of runaway star group 1. The left plot shows the stars as they are forming in the cluster, and the right plot shows the gravitational potential of both the stars and gas. The trajectories of the runaway stars are shown as lines. Once each runaway star forms, it appears with a star marker. This plot shows the same variables as shown in Figures [21](#) and [22](#). [79](#)
- Figure 21 Trajectories of runaway star group 1 originating from a sub-cluster merging into the central cluster, with color indicating stellar velocity (light= v_{\max} , dark= v_{\min}). The dots are star particles at the given time, and the star markers indicate the runaways stars in the group as they form. The total number of stars in the cluster is listed in each panel. [80](#)
- Figure 22 Trajectories of runaway star group 1 originating from a sub-cluster merging into the central cluster, with color indicating stellar velocity (light= v_{\max} , dark= v_{\min}). The isosurfaces show four values of the gravitational potential of both the stars and gas: $|U_g| = 10^{47,48,49,50}$ erg with dark to light as lowest to highest. As the runaway stars form, they are plotted with star markers. The total number of stars in the cluster is listed in each panel. [81](#)

- Figure 23 Trajectories of runaway star group 2 originating from a sub-cluster merging into the central cluster, with color indicating stellar velocity (light= v_{\max} , dark= v_{\min}). The top row (analogous to Figure 21) shows dots as all star particles, and the star markers indicate the runaways stars in the group as they form. The bottom row (analogous to Figure 22) shows the same runaway star trajectories with the potential of gas and stars plotted as isosurfaces. The isosurfaces show four values of the gravitational potential of both the stars and gas: $|U_g| = 10^{47,48,49,50}$ erg with dark to light as lowest to highest. 82
- Figure 24 Histograms of runaway star directions from 1,000 different projections. (*top*) 2D histogram showing the 1,000 projections, sorted vertically and centered horizontally by peak number of runaway stars N_{run} , and wrapped around the x-axis. For every projection there is a strong peak. Looking at each row individually, a fainter peak can be seen to the right or left of the peak value. (*bottom*) The *black* histogram is the average value of the projections, while the *grey* area shows the range from maximum to minimum, with values given by the left axis. The *dashed line* shows the cumulative sum of the runaway stars per bin, with values given by the right axis. 87
- Figure 25 Radial velocity v_r relative to the center of mass over time and orbital properties of the SCES runaway singles and binaries. (*top*) Time evolution of all the runaways in group 1 and 2. (*middle-bottom*) The velocity (*solid*) and semi-major axes a_i (*dotted*) of each member in the two runaway binary stars formed in our simulation. Both are from group 1. The dark lines are the primary stars and the light lines are the companion stars. Orbital properties for each system are listed on the corresponding panel, calculated for the stable orbits after $t = 0.85$ Myr indicated by the vertical black line. 88

- Figure 26 Half-mass stellar density of our model over time. Regions of observed ρ_{hm} values in young clusters (< 10 Myr) are indicated by horizontal grey shaded regions. The dashed border lines show extragalactic clusters and the solid border lines show Milky Way clusters. The vertical shaded regions show the time windows when runaways are dynamically ejected at peak velocity in our M6 model. The observational data was taken from Portegies Zwart et al. (2010). 91
- Figure 27 The three rows with two grouped plots correspond to the M4, M5, and M6 models. The following descriptions apply to the two plots in each row. *Top*: Mass segregation ratio Λ over time for the N_{MST} most massive stars in each cluster. The vertical dotted white lines indicate the time of collapse, where R_{rms} reaches a minimum. The solid white lines correspond to the right vertical axis showing the stellar mass of the cluster. *Bottom*: Mass of the $N_{\text{MST}}^{\text{th}}$ most massive star in each cluster. The grey vertical lines indicate the formation of a new most-massive star ($N_{\text{MST}} = 1$). As these are often not in the core, the time of formation, particularly in M4, corresponds to a drop in the apparent mass segregation. Note that each cluster was run to $\approx 1.5t_{\text{ff}}$, leading to different absolute time scales. 97
- Figure 28 Mass segregation ratio Λ over time for all stars above a given mass threshold M_{Λ} shown on the color bar. Λ is only calculated if there are ≥ 5 stars with mass $\geq M_{\Lambda}$. The threshold for mass segregation is $\Lambda > 1$, above the *horizontal dashed line*. The *vertical dotted lines* indicate the time of collapse, where R_{rms} reaches a minimum. Note the variable time scales in each panel. 98
- Figure 29 Dynamical segregation time for a star with mass M over time based on the cluster's properties. The white line indicates the mass of the most massive star, which can decrease due to mass loss from stellar winds. The grey line shows the evolution of the cluster radius R_{rms} . Note that the dip in the evolution of R_{rms} indicates the time of collapse. 102

Figure 30 Mass segregation ratio Λ versus number of most massive stars N_{MST} for young Galactic clusters. Each grey line represents one snapshot in time for each of the M4, M5, and M6 clusters. 104

LIST OF TABLES

| | | |
|---------|---|-----|
| Table 1 | ISM Phases. | 12 |
| Table 2 | Spectral classes of stars. | 18 |
| Table 3 | Model parameters. | 43 |
| Table 4 | Control parameters. | 43 |
| Table 5 | Results. | 52 |
| Table 6 | Properties of observed super star clusters. | 54 |
| Table 7 | Runaway Group Filters. | 83 |
| Table 8 | Star cluster properties. | 106 |

LISTINGS

Part I

STAR CLUSTER FORMATION THEORY

FUNDAMENTALS OF STAR CLUSTER FORMATION AND EVOLUTION

*In the beginning the Universe was created.
This has made a lot of people very angry
and been widely regarded as a bad move.*

— Douglas Adams¹

1.1 INTRODUCTION

Stars are the building blocks of our Universe. The first generation of stars formed just 100 million years after the Big Bang, lighting up the Universe for the first time and ending the cosmic dark age. Their hot cores forged the elements that make up organic matter, and their energy provides the sustenance for life. Stars are the culmination of millions of years of gravity concentrating hydrogen gas into dense clouds. When a cloud is dense enough to trigger star formation, rarely is a solitary star produced. Current observations indicate that over 90% of stars are formed in groups with anywhere from tens to millions of members (Lada and Lada, 2003). These objects are called *star clusters*.

The canonical definition of a star cluster is a gravitationally bound group of at least 12 stars with little to no dark matter² (Krause et al., 2020). Thus they are distinguished from multiple stellar systems and galaxies. Groups of unbound stars meeting these criteria are called associations (Blaauw, 1964). Star clusters are observed in a wide range of masses, ages, and sizes, though they are typically divided into three categories³.

Open clusters (OCs) have stellar masses $\lesssim 5 \times 10^3 M_{\odot}$, ages $\lesssim 6$ Gyr, and metallicities of $\sim 1Z_{\odot}$. OCs have one stellar population, meaning all stars were formed at roughly the same time. OCs are typically found in the disks of galaxies.

Globular clusters (GCs) are old and massive, with stellar masses $\gtrsim 10^5 M_{\odot}$ and ages $\gtrsim 6$ Gyr. They have metallicities $< 1Z_{\odot}$, as they formed in the early universe from gas less polluted with metals. Most GCs have more than one main sequence track on their color magnitude diagram, and they contain anticorrelations in elemental

¹ *The Restaurant at the End of the Universe* (1980)

² The first star clusters likely formed in the early Universe within small dark matter halos that have since been stripped by the assembly of the host galaxy halo (see Trenti et al., 2015).

³ The properties listed here are meant to give a general sense of cluster characteristics, but there are plenty of overlaps and outliers in these categories.

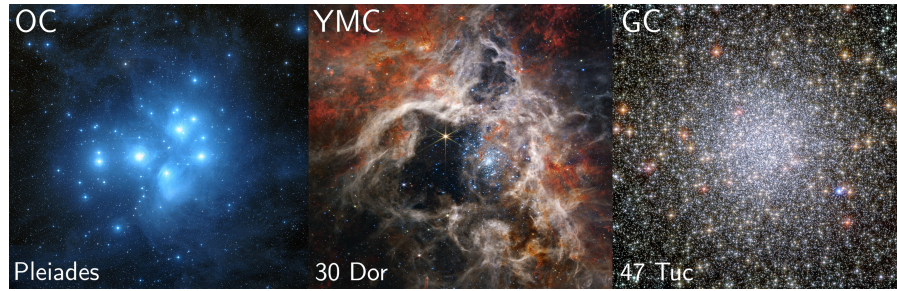


Figure 1: Images showing each type of star cluster: the open cluster Pleiades in the Milky Way, the young massive cluster R136 in the 30 Dor HII region in the LMC, and the Milky Way globular cluster 47 Tucanae. Credits: Davide De Martin, the ESA/ESO/NASA Photoshop FITS Liberator (Pleiades); NASA, ESA, CSA, STScI, Webb ERO Production Team (30 Dor); NASA, ESA/Hubble Heritage (47 Tuc).

abundances which both indicate multiple stellar populations. GCs are found in galactic bulges and halos.

Young massive clusters (YMCs) can be as massive as GCs but much younger, with masses $\gtrsim 10^4 M_{\odot}$ and ages $\lesssim 100$ Myr. They have metallicities of $\gtrsim 1Z_{\odot}$. No multiple populations have been confirmed in YMCs. Most are found in the galactic disk with some in the galactic center. The term *super-star clusters* (SSCs) is sometimes used for YMCs, and other times for just the highest density YMCs.

Examples of each cluster type are shown in Figure 1. Pleiades⁴ is an OC with mass $\sim 800 M_{\odot}$ and is 120 million years old (Pinfield et al., 1998). 30 Doradus (30 Dor), known as the Tarantula Nebula, is a star forming HII region in the Large Magellenic Cloud (LMC) hosting the YMC R136 at its center. R136 has a mass of $\sim 10^5 M_{\odot}$ (Selman and Melnick, 2013). R136 has two clusters of stars with different ages, 1 and 2.5 Myr, suggesting that it consists of two merging clusters (Sabbi et al., 2012). 47 Tucanae (47 Tuc) is the second brightest GC in the Milky Way after Omega Centauri. It has a mass of $\sim 10^6 M_{\odot}$ and is 11 billion years old (Heyl et al., 2017).

Globular clusters are some of the oldest objects in the Universe. The oldest GCs are over 13 billion years old, and because of this GCs have provided a key constraint to the age of the Universe. The properties of GCs are intricately tied to those of their host galaxies, and they

⁴ On a clear night, six of the Pleiades stars are visible from Earth. People with exceptional eyesight can see seven. As a result, Pleiades has found its way into the mythologies of many ancient civilizations. The ancient Greeks believed the stars to be seven daughters of the Titan Atlas. They were turned into stars by Zeus to comfort their father after he was forced (by Zeus) to carry the heavens on his shoulders. The ancient Egyptians believed that the Pleiades stars were in fact seven goddesses in the form of celestial cows grazing the night sky. They worshipped them in return for nourishment in the form of bread and beer. Aboriginal legend has it that Pleiades were originally seven sisters called the Karatgurrk that hoarded the secret of fire until they were tricked by a crow. This is how mankind was given the gift of fire. Most myths have an explanation for why one star is invisible to most.

can be used to directly probe the assembly history of galaxies (see, e.g., Adamo et al., 2020). The radiation from early star clusters is thought to be responsible for the re-ionization of the Universe, and in the modern Universe, their feedback has galactic scale impact on their hosts. The production of heavy elements in early embedded clusters contributed to the current generation of solar metallicity stars. Most young stars are still in their natal cluster where protoplanetary disks form. Thus, understanding the formation and evolution of star clusters is fundamental for galaxy theory, planet formation theory, and cosmology.

The origin of multiple populations in GCs is one of the greatest unresolved debates in modern astronomy. Though many hypotheses have been put forward, there has yet to be a complete formation framework that naturally leads to a second generation of star formation. The absence of multiple populations in young clusters begs the question: do globular clusters form in a fundamentally different way than young massive clusters? Are YMCs just young globular clusters forming in a high metallicity, modern Universe? Or are they simply the most massive open clusters forming from larger, denser clouds?

Observations provide constraints on the resolvable properties of star clusters. These are snapshots of the cluster frozen in time; theoretical models are needed to answer the question of how these star clusters formed and evolved to acquire the characteristics we observe.

The basis of our knowledge on star cluster formation and evolution comes from simulations, but these also have their limits. Star cluster formation presents a formidable computational challenge. A complete model must evolve the gas, stars, radiation, and the interaction between all three. The space and time scales for the global cloud and individual stars span many orders of magnitude, so approximations must be made.

Models usually increase computational efficiency by approximating sub-clusters of stars as a single particles, limiting the amount of stars to calculate the dynamics and feedback physics for. This is because computation time increases with number of particles as $\approx N^2$. State of the art cluster formation codes use new techniques to efficiently evolve each individual star. Most of these star-by-star models are still limited to small cluster sizes with $\lesssim 10^3$ particles. As a result, small open clusters can be accurately modelled, but young massive clusters remain out of reach.

The goal of this thesis is to bridge that gap and perform star-by-star simulations of YMC formation. I have taken the star cluster formation framework TORCH (Wall et al., 2020, 2019), previously limited to $\lesssim 10^3$ particles, and modified it to be capable of modelling $\gtrsim 125,000$ star particles. With the improved TORCH, I ran a suite of simulations of massive clusters forming from gas clouds with initial masses of 10^4 , 10^5 , and $10^6 M_\odot$ and radius $R = 11.7$ pc. These parameters were

chosen with the intent of determining whether YMC and OC formation are simply different mass regimes or if they entail different formation modes entirely.

In this chapter, I review the fundamental physics and components involved in star cluster formation and evolution. I begin with an overview of star cluster formation in Section 1.2.1, and then briefly discuss their properties in Section 1.2.2. Section 1.3 covers the relevant interstellar medium physics that lead to the formation of GMCs, the parents of star clusters. The process of star formation in GMCs is examined in Section 1.4. Chapter 2 presents the numerical methods used in TORCH to model the physics described in this chapter, as well as the modifications made to enable massive cluster modelling.

The results of this study begin in Chapter 3 which focuses on the global properties of the modeled clusters. Section 3.3 describes the simulation parameters and initial conditions of each cluster model, and goes into further detail on the methods used in this thesis. Section 3.4 provides a full analysis of the global time-evolved properties of the three cluster models, such as the star formation history and boundedness, and compares them to each other. These results are analyzed and compared to observations in Section 3.5, with the main results of this chapter summarized in Section 3.4.

Chapter 4 describes a new mechanism for producing runaway stars we discovered in our most massive cluster model. The sub-cluster ejection scenario (SCES), which results in stars being tidally ejected during sub-cluster mergers, is analyzed in Section 4.3. Observations of runaways that could be candidates of SCES are identified in Section 4.4, as well as observational signatures of SCES runaways. Section 4.5 summarizes the results of this chapter.

Chapter 5 analyzes the dynamical mass segregation in each modelled cluster. Section 5.3 finds that early dynamical mass segregation is achieved by the initial collapse of the sub-clusters which form a dense core with a small crossing time. Section 3.5 explores this mechanism for mass segregation and compares our findings to observations. The main results on mass segregation are listed in Section 5.5.

Chapter 6 concludes with the main results and future work of this thesis.

1.2 STAR CLUSTERS

1.2.1 Formation

Star clusters form in giant molecular clouds (GMCs) that are gravitationally collapsing. Turbulence in the cloud sets a pattern of dense substructures that collapse to form stars in small groups called *sub-clusters*. Feedback from the stars in the form of radiation and stellar wind begin to heat and expel the local gas near the sub-clusters. The

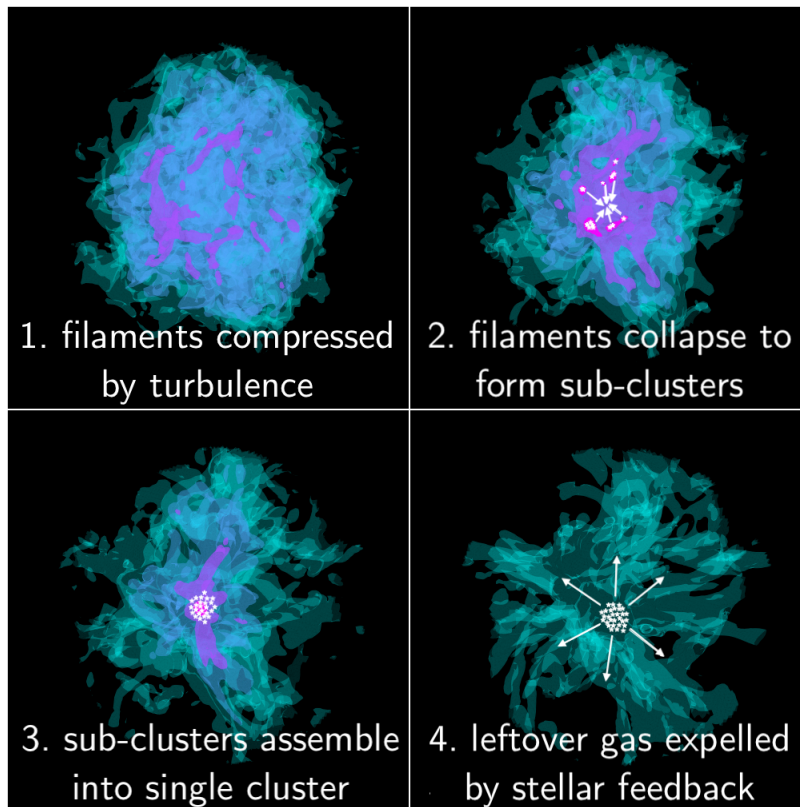


Figure 2: Overview of the star cluster formation process. The colored surfaces represent gas in a molecular cloud of increasing density from blue to pink, with star forming gas in hot pink. The white dots are stars. 1. During global gravitational collapse of the cloud, turbulence creates a hierarchical structure of overdense filaments. 2. The overdense filaments collapse faster than the global cloud, creating sub-clusters tracing the dense substructure. 3. The sub-clusters dynamically merge to the center of mass and form a single star cluster. 4. The combined feedback of the star cluster eventually expels the unused gas. While this diagram is purely illustrative, the colored surfaces trace the gas from a star cluster formation simulation presented in this thesis.

sub-clusters eventually merge dynamically into a single entity. Their combined feedback has a stronger effect on the gas left in the embedded young cluster. Eventually, massive stars will start to explode as supernova (SN) exerting a large force on the gas. The clearing of all the gas is called gas expulsion, and after this either a bound star cluster is left or the cluster is dispersed into an unbound association. The complete dispersal of a cluster into field stars comes much later and can be caused by interactions with the host galaxy or internal dynamics in the cluster. This is called the *global hierarchical collapse* scenario of star cluster formation (see Gómez and Vázquez-Semadeni, 2014; Vázquez-Semadeni et al., 2009, 2017).



Figure 3: The Pillars of Creation (the Eagle nebula) images taken by JWST in mid-infrared (5.6-25.5 μm), and near-infrared (0.6-5.0 μm). Mid-infrared radiation is opaque to dust, so in the MIRI image we see the structure of the dense molecular gas. Near-IR is transparent to dust, and this wavelength reveals the prolific formation of young stars within the pillars. *Credit: NASA, ESA, CSA, STScI.*

This picture of star cluster formation originated from simulations and is supported by observations. R136 appears to consist of two recently merged sub-clusters aged 1.5 Myr apart (Sabbi et al., 2012). An analysis of 17 young star forming regions ($\lesssim 5$ Myr) found all of them to be highly clustered (Kuhn et al., 2015, 2014). For a visual on the size and scale of the sub-clustering, Figure 5 of Kuhn et al. (2015) plots the stellar surface density for each of the 17 star forming regions.

Elmegreen and Falgarone (1996) originally established the hierarchical structure of GMCs. This becomes evident when looking at any picture of a star forming cloud. JWST images of the M16 star forming region M16, also called the Eagle nebula and the Pillars of Creation, are shown in Figure 3. in the mid-infrared and near-infrared. The left image was taken in mid-infrared (IR) and the right in near-infrared. Dust is opaque to mid-IR, so we can see the outer layer of the cold, dense, dusty molecular gas. In the near-IR, dust becomes transparent revealing the network of young stars forming within the dense pillars.

The young OC NGC 6611 has been forming in the Eagle nebula for around 2 million years (Hillenbrand et al., 1993). The feedback from this cluster has blown away the low density gas, revealing the filamentary structure of the parent GMC. This is what we expect from our picture of a young, forming star cluster.

The fundamental property describing the formation of a star cluster is the *star formation efficiency* (SFE). This parameter measures the percentage of the initial cloud mass that gets converted into stars,

$$\epsilon_{\star} \equiv \frac{M_{\star}}{M_{\text{cloud}}}. \quad (1)$$

Chapter 3 discusses the SFE and the affect it has on young clusters extensively. The SFE is defined this way primarily for modeled clusters, as observers cannot know the initial mass of the cloud. Instead, they calculate an instantaneous SFE,

$$\epsilon_{\text{inst}} \equiv \frac{M_{\star}}{M_{\star} + M_{\text{gas}}}, \quad (2)$$

which compares the current stellar mass to the current mass in stars and gas. The SFE has a strong positive correlation with the initial density of the cloud. This is because the main mechanism to quench star formation and disperse dense gas is stellar feedback. At a certain density, stellar feedback cannot overpower density. The SFE also plays a role in the lifespan of the cluster. Clusters forming from low density clouds will have lower SFE, but stellar feedback will be more effective on the low density gas. If gas expulsion occurs in a cloud with low SFE, that means the majority of the gravitational potential will be blown away with the gas, taking the young cluster with it.

1.2.2 Properties

The most fundamental characteristics of a star cluster are the age and mass of its stellar population. These can be determined by plotting the individual stars on a color-magnitude diagram (CMD). Color (B-V)⁵ is a proxy for effective temperature, and apparent magnitude is a measure of luminosity and therefore mass. These relations can be derived by approximating stars are black bodies, i.e., are in thermal equilibrium, with effective temperature T_{eff} . This means they radiate with intensity B_{ν} at frequency ν given by

$$B_{\nu} = \frac{2h\nu^3}{c^2} \frac{1}{e^{h\nu/k_b T_{\text{eff}}} - 1}, \quad (3)$$

where k_b is Boltzmann's constant and h is Planck's constant. Then, the effective temperature can be estimated with color using (Balles-teros, 2012)

$$T = 4600 \left(\frac{1}{0.92(B - V) + 1.7} + \frac{1}{0.92(B - V) + 0.62} \right). \quad (4)$$

The absolute magnitude V of an object is the magnitude it would have if it were 10 pc away. For an object with an apparent magnitude m at a distance d in pc, the absolute magnitude is given by $V = m - 5(\log_{10}(d/\text{pc}) - 1)$. We can calculate the luminosity of the object with V by the relation $V - V_{\odot} = -2.5 \log_{10} \left(\frac{\mathcal{L}}{\mathcal{L}_{\odot}} \right)$, using the luminosity

⁵ B-V color is calculated by subtracting the apparent magnitude in two filter bands.

and magnitude of the sun. Finally, we can calculate the star’s mass using the luminosity-mass relation

$$\frac{\mathcal{L}}{\mathcal{L}_{\odot}} = b \left(\frac{M}{M_{\odot}} \right)^a, \quad (5)$$

where a and b vary for different stellar masses. For main sequence stars with masses $2 < M/M_{\odot} < 55$, $a \approx 3.5$ and $b \approx 1$.

With these relations, we can use the CMD to get the total stellar mass. The mass at which the main-sequence turn-off occurs in the CMD gives the age of the stellar population (see Section 1.4.3). This method only works if the individual stars are resolved, so this is applied to clusters in the Milky Way, LMC, and M31. At distances $\gtrsim 1$ Mpc, the age of a cluster must be determined by fitting stellar population models as a function of age and mass to its observed luminosity (e.g., Adamo et al., 2010). Therefore, the properties of clusters in the Milky Way and neighboring galaxies are substantially better constrained.

A star cluster has no definite boundary, so the half-mass radius is often used as a way to define their size. This is simply the minimum radius that contains half of the cluster’s mass. Star clusters have half-mass radii of $R_{\text{HM}} \approx 0.2 - 20$ pc. The *cluster mass function* (CMF) is the distribution of all star cluster masses, and it is described by a power law of the form

$$dN/dM \propto M^{-2 \pm 0.2}. \quad (6)$$

There is ongoing debate as to whether there exists a truncation mass (see Krumholz et al., 2019). Star cluster masses range from $M_{\text{cl}} \approx 10^1 - 10^7 M_{\odot}$, and density ranges from $\rho \approx 10^{-1} - 10^{5.5} M_{\odot} \text{ pc}^{-3}$ (Krumholz et al., 2019).

Figure 4 shows measured values of the mass-radius relation of local star clusters. The points are median values, and the error bars indicate the 16th and 84th percentiles. Here, the term SSC refers to YMCs that are especially dense. Lines of constant volume and surface density are shown on the plot. The lack of low-mass clusters detected outside the Milky Way is a signature of observation bias. At such distances, only the brightest clusters, i.e., most massive, are detectable.

1.3 THE INTERSTELLAR MEDIUM

The interstellar medium (ISM) consists of the gas, dust, and radiation filling the space between stars in a galaxy. Star clusters form from GMCs, which are the densest phase of gas in the continuum of the ISM. Therefore, the dense substructure of the ISM sets the spatial distribution of star formation in a galaxy. Stars return energy and mass to the ISM during their lifecycle via radiation, outflows, and supernovae. Thus stars are another manifestation of the energy and

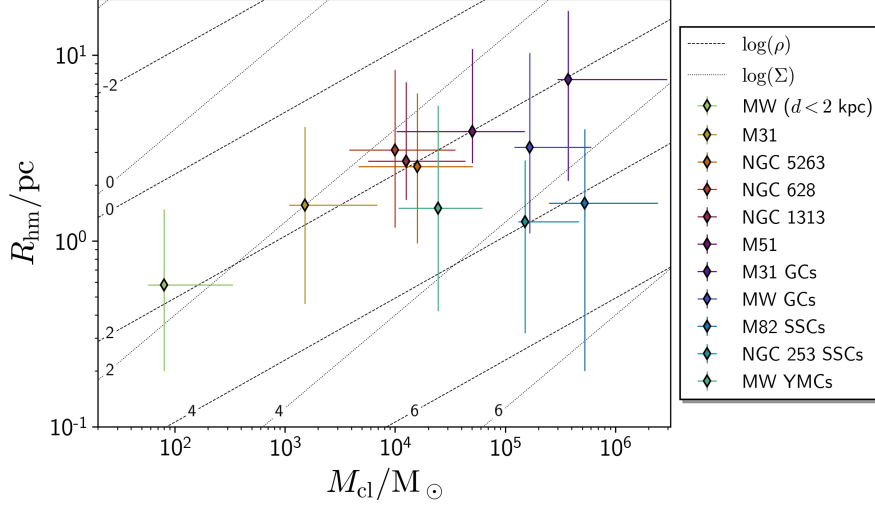


Figure 4: Measured values of the median mass and half-mass radius of clusters in the Milky Way and local galaxies. Error bars indicate the 16th and 84th percentiles. Lines of constant density $\rho(M_{\odot} \text{ pc}^{-3}) = 3M/8\pi R_{\text{hm}}^3$ and surface density $\Sigma(M_{\odot} \text{ pc}^{-2}) = M/2\pi R_{\text{hm}}^2$ are plotted as dashed and dotted lines, respectively. Data taken from Table 3 in Krumholz et al. (2019).

matter in the ISM. The physics governing the state of the ISM is the foundation of star formation in GMCs.

1.3.1 Composition

The mass in the ISM is composed mostly of hydrogen (70%) and helium (28%). The remaining mass is split evenly between gaseous metals⁶ and metals in dust grains. Dust grains are responsible for absorbing starlight and re-emitting an infrared black-body spectrum. Dust grains absorb photons with wavelength smaller than their physical size. The majority of extinction occurs in the UV indicating a higher prevalence of small dust grains (Mathis et al., 1977).

1.3.2 Thermal phases

The thermal and chemical state of the ISM are classified by five distinct phases listed in Table 1. Star formation takes place in the molecular gas phase, which is often in the form of discrete GMCs embedded in the CNM. The CNM and WNM comprise the classical two-phase ISM where two thermally stable phases exist for a wide range of pressures assuming thermal equilibrium (Field et al., 1969). The HIM phase is found in SNe blown bubbles, and is stable for long times at this temperature due to the low atomic cooling rate for $T > 10^6$ K

⁶ In astronomy, elements heavier than helium are referred to as metals.

(McKee and Ostriker, 1977). The last classical phase of the ISM is the WNM which contains over 90% of the ionized gas in the Galaxy (Hoyle and Ellis, 1963). The average dust temperature in the Milky Way is $T_d \approx 20$ K (Planck Collaboration et al., 2014).

Table 1: ISM Phases.

| Phase | T [K] | n [cm ⁻³] | χ_H |
|---------------------------|--------------|-----------------------|----------------|
| Hot ionized medium (HIM) | $\sim 10^6$ | $\sim 10^{-2}$ | 1.0 |
| Warm ionized medium (WIM) | $\sim 8,000$ | 0.2-0.5 | 1.0 |
| Warm neutral medium (WNM) | 6,000-10,000 | 0.2-0.5 | ~ 0.1 |
| Cold neutral medium (CNM) | 50-100 | 20-50 | $\sim 10^{-4}$ |
| Molecular gas | 10-20 | $> 10^2$ | $\sim 10^{-6}$ |

Listed values are temperature, number density, and ionization fraction of hydrogen. Table adapted from Klessen and Glover (2016).

1.3.3 Heating & Cooling

There are many heating and cooling processes that affect the thermal and ionization state of the ISM. We discuss only the relevant heating and cooling mechanisms at work in molecular clouds and embedded young clusters.

Cooling of interstellar gas occurs when atoms and molecules are collisionally excited to higher quantum energy states and then deexcite, releasing a line emission photon. This is called *line cooling*.

Permitted lines. At $T \simeq 10^4$ K, cooling is dominated by Lyman-series transitions. The Lyman-series of atomic hydrogen are transitions of the electron from energy level $n \geq 2$ to $n = 1$ which emit UV spectral lines. The transition from $n = 2 - 1$ is called the Ly- α line. Above $\sim 3 \times 10^4$ K, atomic hydrogen becomes rare and cooling is dominated by C, O, Fe, and Ne (Gnat and Ferland, 2012). At the low temperatures of $T \simeq 20$ K in molecular clouds, the collisional excitation of the rotational states of the CO molecule is particularly important due to their small energy separations. In fact, the detection of CO lines is the predominant method for detecting molecular clouds. CO cooling only dominates when there are no fine-structure emissions from C or C⁺, and this only occurs above $n \sim 1,000$ cm⁻³.

Fine structure lines. Due to the spin-orbit coupling, an electron with anti-parallel spin S and orbital angular momentum L is in a lower energy state than when they are parallel. This leads to a splitting of energy levels known as *fine structure splitting*. Fine structure splitting of the ground state occurs if the outermost electrons have both $L > 0$ and $S > 0$. Fine structure cooling in the ISM is mostly attributed to C, C⁺, and O.

Dust cooling. If the gas is hotter than the dust in the ISM, energy will transfer to the dust through gas-grain collisions. The dust grains will then emit this energy thermally, as they are efficient radiators.

The primary sources of heating within GMCs are cosmic rays and UV photons. The UV photons are emitted by forming stars embedded in the cloud, as incident UV photons from the interstellar radiation field (ISRF) cannot penetrate the dense gas.

Photoelectric effect. When UV photons interact with a dust grain, a photoelectron can be released. Only some of the photon's energy is needed to overcome the electron binding energy, and the rest is imparted to the electron as kinetic energy. These highly energetic electrons collisionally heat the gas.

Photoionization. The release of a bound electron from neutral atoms by the absorption of a photon with $E_\gamma \geq E_{\text{ion}}$.

Cosmic rays. Cosmic rays are high-energy fundamental particles (mostly protons) with velocities between 44% and 99.6% the speed of light. They heat the gas by ionization, excitation, and the scattering of free electrons.

Dynamical heating. Turbulent dissipation heats the gas in the collapsing regions of molecular clouds through shocks. If the magnetic field is strong, ambipolar diffusion dominates the turbulent heating (Li et al., 2012). Ambipolar diffusion is the motion of ions through neutral gas due to the electric field, and the collisions caused by this movement heats the gas.

1.3.4 Turbulence & Gravity

Turbulence is the flow of gas set by random motions at all scales. A flow is incompressible if the density of the material remains constant with subsonic velocities, while a compressible flow can be compressed to higher densities under a driving force. Classical descriptions of turbulence consider the simplified case of incompressible flow.

Kolmogorov (1941) found that turbulence driven at a large scale D will form eddies that interact to form smaller and smaller eddies, which eventually reach a length scale d at which viscosity begins to dissipate energy. This is known as the turbulent energy cascade. The energy distribution referred to as the *Kolmogorov spectrum* is a power-law of the form

$$E(k) \propto k^{-5/3}, \quad (7)$$

where $k = 2\pi/\ell$ is the dimensionless wavenumber. This describes the energy cascade in the *inertial range* of $1/D \ll k \ll 1/d$, where little dissipation occurs and energy is transferred via inertial forces to smaller scales. The energy distribution is set by the turbulent driving force at larger scales and by the viscosity at smaller scales.

The ISM, however, is highly compressible, has supersonic flows, and the driving turbulent forces are far from uniform. Supersonic turbulence produces shock waves that can dissipate energy across large scales. The gas in the ISM is also magnetized, so Alfvén waves with velocity $v_A = B/\sqrt{4\pi\rho}$ affect the turbulent eddies. The dominant form of turbulent driving in the ISM comes from supernova explosions. Mac Low and Klessen (2004) found that supernova driving alone can maintain the observed interstellar turbulence.

1.3.5 Formation of GMCs

The densest gas in the ISM is collected in GMCs of mostly molecules, whereas the rest of the ISM is mostly atomic. GMCs are massive (10^4 - $10^6 M_\odot$), cold (10 K), and dense ($\geq 10^2 \text{ cm}^{-3}$). In order for a molecular cloud to form, gas must become dense enough to shield molecules from photo-dissociation by the ISRF long enough to allow the population of molecules to grow. The most promising theory of molecular cloud formation is the colliding flow model. This occurs in the turbulent ISM when two flows in the WNM collide, triggering a thermal instability that leads to the formation of a colder and denser region of gas (Hennebelle and Pérault, 1999).

1.3.6 GMC Properties

The majority of the mass in GMCs is contained in H_2 molecules, but H_2 is not directly detectable. Cloud masses are instead determined by measuring CO emission, the second most abundant molecule in GMCs. A constant ratio of H_2 to CO is assumed. For example, the ratio of H_2 to ^{13}CO is $Y_{^{13}\text{CO}} = 5.0 \pm 2.5 \times 10^5$ (Dickman, 1978). The measured mass spectrum of Local Group molecular clouds can be described by a power law

$$\frac{N}{M} \propto M^{-\alpha}, \quad (8)$$

where α ranges from 1.5 – 2.9 (Rosolowsky, 2005). There is strong evidence for a mass cutoff at $10^{6.5} M_\odot$ in the inner Milky Way, and weak evidence for a similar cutoff in the Large Magellanic Cloud (LMC). However, there is no evidence for a mass cutoff in the outer Milky Way or M33. A molecular cloud is typically considered a GMC if its mass is $\geq 10^4 M_\odot$.

The densities of Milky Way GMCs are highly variable, with average molecular surface densities between $1 \leq \langle \Sigma_{\text{mol}} \rangle / M_\odot \text{ pc}^{-2} \leq 2,000$ (Colombo et al., 2019). Average cloud densities in other galaxies have been observed as high as $\langle \Sigma_{\text{mol}} \rangle = 6,000 M_\odot$ (Leroy et al., 2015). Galactic and extragalactic surveys find a strong correlation between GMC and host galaxy density, with the cloud surface density peaking at the galactic center and decreasing towards the galaxy edge.

A cloud is in virial equilibrium if gravity and kinetic energy are in equilibrium. The virial state of a cloud is defined in terms of the *virial parameter* ,

$$\alpha_v \equiv \frac{E_k}{|E_g|} = \frac{\sigma^2 R}{2GM}, \quad (9)$$

where $\alpha_v = 1/2$ is the equilibrium value. A cloud is bound and subject to collapse in a sub-virial state ($\alpha_v < 1/2$) and unbound in a super-virial state ($\alpha_v > 1/2$). Surveys find the virial parameter of clouds to scale with mass as $\alpha_v \propto M^{-0.5}$ (Miville-Deschênes et al., 2017). GMCS ($\geq 10^4 M_\odot$) tend to be in virial equilibrium or sub-virial (see Chevance et al., 2023).

A landmark survey done by Larson (1981) of Milky Way molecular clouds revealed three scaling relations. The *Larson scaling relationships* are:

$$\sigma \propto R^a \quad (10)$$

$$\sigma \propto M^b \quad (11)$$

$$n \propto R^c, \quad (12)$$

where σ is the velocity dispersion, R is cloud size, M is cloud mass, and n is number density. The original exponents found by Larson (1981) are $a = 0.38$, $b = 0.2$, and $c = -1.10$. The physical interpretations of these relations are that all molecular clouds (1) have turbulent gas flow (see Sect. 1.3.4), (2) are in virial equilibrium (using Eq. 9), and (3) have similar surface densities.

The exponents of Larson's relations have been corrected with improved observational instruments. Modern observations currently put the exponents at $a = 0.63 \pm 0.30$ (Miville-Deschênes et al., 2017), $b = 2.2 \pm 0.2$, and $c = 0.43 \pm 0.14$ (Grisdale et al., 2018). The second two relations describe general trends, but in reality, Galactic GMCS are much more complex. As discussed earlier, GMCS exist in a wide range of the surface densities and virial states. However, all surveys agree on the pervasiveness of turbulence in GMCS (Equation 10).

1.4 STAR FORMATION IN GMCS

1.4.1 Collapse conditions

We have discussed the role of gravity and turbulence in condensing the gas in GMCS until collapse into stars occurs. The self-gravity of the cloud must overcome the thermal and magnetic pressure supporting the cloud. The thermal and magnetic energies are given by

$$E_{\text{therm}} = nk_B T \quad (13)$$

$$E_{\text{mag}} = \frac{B^2}{8\pi}. \quad (14)$$

There is a critical length scale on which the self-gravity of a cloud overcomes the thermal pressure supporting the cloud and collapse is triggered. This threshold is defined for a spherical cloud⁷, and is called the *Jeans length* (Jeans, 1902)

$$\lambda_J = \sqrt{\frac{\pi}{G\rho}} c_s^2 = \sqrt{\frac{\pi}{G\rho} \frac{k_b T}{\mu m_H}} \propto \sqrt{\frac{T}{\rho}}, \quad (15)$$

where $c_s^2 = k_b T / \mu m_H$ is the isothermal sound speed, k_b is Boltzmann's constant, and μ is the mean molecular weight. Scales larger than λ_J are Jeans unstable and subject to gravitational collapse. Intuitively, colder and denser gas has a smaller Jeans length and is more prone to collapse due to lower thermal support and higher gravity. After the onset of collapse, when the gas reaches a critical temperature, fusion begins and a star is born.

The entire cloud does not have to be Jeans unstable for star formation to occur. Gravity and turbulence will fragment the cloud and compress filaments of gas that become jeans unstable and collapse to form stars. The analytic timescale for gravitational collapse is given by the *free-fall time*,

$$t_{\text{ff}} = \sqrt{\frac{3\pi}{32G\rho}}, \quad (16)$$

which describes the time for a test particle at the edge of a uniform density spherical cloud to reach the center.

There is a similar criteria for cloud collapse against magnetic pressure. Magnetic fields scale with density via a power law $|\mathbf{B}| \propto \rho^\kappa$ where $\kappa = 2/3$ in the flux-frozen limit of ideal MHD. Measurements of the magnetic field strength in ISM molecular clouds confirm this relation, and they find line of sight magnetic field strengths ranging from $B_{\text{LOS}} = 10 - 3,000 \mu\text{G}$ (Crutcher et al., 2010). These measurements are done using the Zeeman effect, where the presence of a magnetic field splits spectral lines⁸. The frequency shift is related to the field strength by $\Delta\nu \propto \mu_B B_{\text{LOS}}$ where μ_B is the Bohr magneton. The gravitational stability criteria for a spherical cloud with magnetic pressure is given by the *mass-flux ratio*

$$\left[\frac{M}{\Phi} \right]_c = \frac{\zeta}{3\pi} \sqrt{\frac{5}{G}} = 490 \frac{\text{g}}{\text{Gauss cm}^2}, \quad (17)$$

where the correction factor $\zeta = 0.53$ for a uniform sphere is used (Strittmatter, 1966).

⁷ The Jeans length assumes an isothermal, homogeneous, non-magnetized medium with no turbulence.

⁸ The Zeeman effect has been detected in the molecules HI, OH, and CN in the gaseous ISM.

1.4.2 Stellar initial mass function

The measured probability density for a star to form with a given stellar mass is called the *initial mass function* (IMF). The IMF is well described by a power law,

$$N(m)\Delta m = N_0 \left(\frac{m}{M_\odot} \right)^{-\alpha} \left(\frac{\Delta m}{M_\odot} \right), \quad (18)$$

where $\alpha = 2.35$ for $m/M_\odot = 0.4 - 10$ in the original work of Salpeter (1955). Further work done by Kroupa (2002) fit the IMF with a broken power law for different mass regimes. The Kroupa IMF in full form is given by

$$N(m) = \begin{cases} N_0 k_3 m^{-2.3} & \text{for } 1 \leq m/M_\odot < 150, \\ N_0 k_2 m^{-2.3} & \text{for } 0.5 \leq m/M_\odot < 1, \\ N_0 k_1 m^{-1.3} & \text{for } 0.08 \leq m/M_\odot < 0.5, \\ N_0 k_0 m^{-0.3} & \text{for } 0.01 \leq m/M_\odot < 0.08, \end{cases} \quad (19)$$

where N_0 is a global normalization constant and $k_0 = 1$, $k_1 = k_0 m_1^{-0.3}$, $k_2 = k_1 m_2^{-1.3}$, and $k_3 = k_2 m_3^{-2.3}$ with $m_1 = 0.08 M_\odot$, $m_2 = 0.5 M_\odot$, and $m_3 = 1 M_\odot$. The minimum mass for hydrogen burning is $0.08 M_\odot$. The IMF is very top heavy; $\approx 90\%$ of hydrogen burning stars are $\leq 1 M_\odot$. The average mass of the Kroupa IMF is $\bar{m} = 0.38 M_\odot$.

1.4.3 Stellar evolution

When gas collapses into a star, it first forms a dense core called a *protostar* surrounded by a protoplanetary disk. As material is accreted by the protostar, it collapses further, rotates faster, and heats up. The star is considered born when the protostar reaches the temperature required for hydrogen burning in the core: this marks the beginning of the star's life on the *main sequence* (MS).

Stars are divided into spectral classes that are determined by their initial mass, which are listed in Table 2. The lifecycle of a star is completely dependent on their mass. Stars of different classes have defined tracks on the *Hertzsprung-Russell diagram* (HRD), which plots stellar luminosity as a function of effective temperature. The HRD is equivalent to the CMD discussed in Section 1.2.2, but uses physical rather than observed values.

A star leaves the MS when all the hydrogen has been converted into helium in its core. The lack of H-burning support causes significant changes in the state of the star. Stars less than $0.6 M_\odot$ stay on the MS for longer than the age of the universe, so they're fate has never been observed. The time a star of a given mass spends on the main

Table 2: Spectral classes of stars.

| Spectral Class | T_{eff} [K] | M [M_{\odot}] | MS Lifespan |
|----------------|----------------------|---------------------|-----------------|
| O | 28,000 - 50,000 | 20 - 60 | 1 - 10 Myr |
| B | 10,000 - 28,000 | 3 - 18 | 11 - 400 Myr |
| A | 7,500 - 10,000 | 2.0 - 3.0 | 400 Myr - 3 Gyr |
| F | 6,000 - 7,500 | 1.1 - 1.6 | 3 - 7 Gyr |
| G | 4,900 - 6,000 | 0.85 - 1.1 | 7 - 15 Gyr |
| K | 3,500 - 4,900 | 0.65 - 0.85 | 17 Gyr |
| M | 2,000 - 3,500 | 0.08 - 0.05 | 56 Gyr |

sequence is well defined, so in an HR diagram, the mass at which the MS turnoff occurs tells us the age of the stellar population.

Stars of mass $0.6 - 10 M_{\odot}$ undergo rapid expansion to the sub-giant phase and become red giants with an inert helium core and hydrogen burning in outer shells. Convection brings fused material from the core to the envelope. The electron-degenerate helium cores of $0.6 - 2 M_{\odot}$ stars undergo a thermal runaway nuclear fusion of He into C producing a *helium flash*. The large amounts of energy produced expands the core, and as the star contracts again, it moves to the horizontal branch of the HR diagram and begins envelope he-burning with a CO core. More massive red giants do not undergo a He flash and burn their He core more slowly.

After the red giant branch, when all He in the core is consumed, stars move to the asymptotic giant branch (AGB) where they burn He and H in shells outside of their CO core. He fused in the H-burning shell will fall onto the He-burning shell, which rapidly increases the He-burning. This produces thermal pulses that result in stellar winds. Eventually, the envelope is stripped and a white dwarf forms.

The most massive stars ($8 - 40 M_{\odot}$) will continue fusing heavier elements until an iron core is formed. An Fe core produces no energy, so the core collapses as a Type II SN, leaving a neutron star or black hole remnant. A white dwarf that accretes enough mass to put it above the Chandrasekhar limit of $1.44 M_{\odot}$ will undergo runaway carbon fusion and explode as a Type Ia SN, leaving no remnant. Supermassive stars ($\gtrsim 40 M_{\odot}$) lose their envelopes through stellar winds, skipping the red giant phase, and undergo core-collapse Type Ib/c SN forming a black hole or neutron star remnant.

1.4.4 Stellar feedback

Stellar feedback – in the form of jets, winds, radiation, and SNe – has a significant effect on the evolution of a young star cluster. Each of these modes of feedback work to clear dense gas, which quells

further star formation. An open question remains as to in which environments feedback quenches star formation, or gravity overpowers feedback and star formation continues.

Analytical models of feedback energy assume spherical injection into a homogeneous medium. In reality, GMCs are highly clumpy and structured, which can alter the affect of feedback significantly. Realistic numerical models are needed to quantify the efficiency of feedback on quenching star formation in embedded clusters.

The dominant form of feedback from low-mass stars is jets and outflows. Jets and outflows contribute little to the total feedback energy budget and do not have sufficient energy to disperse GMCs. Jets and outflows do drive turbulence, however, which affects the structure of star forming gas (see Nakamura and Li, 2007). The vast majority of the feedback energy budget is injected by O-B type stars through radiation and stellar winds at times < 3 Myr, after which SN energy dominates.

1.4.4.1 Radiation

Stellar radiation interacts with the surrounding gas through heating, ionization, and radiation pressure. The radiative transfer equation for a beam with intensity I is given by,

$$\frac{\partial I}{\partial t} + \mathbf{n} \cdot \nabla I = -\kappa_{\nu} I + j_{\nu}, \quad (20)$$

where κ_{ν} and j_{ν} are the frequency dependant absorption and spontaneous emission coefficients, respectively. Ionizing EUV photons with $h\nu > 13.6$ eV will ionize the local atomic hydrogen, forming an HII region. The edge of the region is where ionization is balanced by recombination, and in a uniform medium this is defined by the *Strömgren radius*,

$$R_S = \left(\frac{3Q_{\text{ion}}}{4\pi n_{\text{H}}^2 \alpha_B} \right)^{1/3}, \quad (21)$$

where Q_{ion} is the emission rate of ionizing photons and α_B is the case B⁹ recombination constant (see Draine, 2011). The ionized gas creates a thermal pressure force on surrounding neutral gas. At the surface of a Strömgren sphere, this force is $F_{\text{ion}} = 8\pi n_{\text{ion}} k_b T R^2$. In reality, the surrounding medium is clumpy, and ionized gas will preferentially escape into low density regions while dense gas is accelerated more slowly.

Photoionizing radiation is the most important feedback mechanism in young clusters, except in very dense massive cluster where radiation pressure dominates. Given a luminosity \mathcal{L} , the radiation force

⁹ Case B excludes the ground state in the sum over all hydrogen states. This approximation is used in optically thick mediums, because recombinations to the ground state produce ionizing photons that are absorbed locally.

is $F_{\text{rp}} = (\mathcal{L}/4\pi R^2 c)(1 - e^{-\tau})$, where τ is the optical depth. The dust in dense structures of GMCs is optically thick to FUV radiation, so radiation pressure dominates in dense clouds. In cases of extremely high optical depth, the radiation pressure exerted by the reprocessed infrared radiation by dust can become important.

1.4.4.2 Stellar winds

The surface of O stars drive winds at $\sim 10 - 3000 \text{ km s}^{-1}$ forming hot wind-blown bubbles. The structure of a bubble consists of four layers: stellar wind (R_1), shocked stellar wind (R_c), shocked interstellar gas (R_2), and the ambient ISM. The wind termination shock radius (R_1) in an ambient medium of density ρ_0 is given by,

$$R_1 = 0.74 \left(\frac{\dot{M}}{\rho_0} \right)^{0.3} v_w^{0.1} t_w^{0.4}, \quad (22)$$

where \dot{M} is the stellar mass loss rate, v_w is the terminal wind velocity, and t_w is the age of the wind (see Weaver et al., 1977).

The wind deposits energy defined by the mechanical luminosity

$$L_w = \frac{1}{2} \dot{M} v_w^2. \quad (23)$$

O and B stars lose mass at rates $\dot{M} \approx 10^{-8} - 10^{-6} M_\odot \text{ yr}^{-1}$. A wind bubble expanding into a clumpy medium can lose energy through turbulent mixing and rapid cooling at the border.

1.4.4.3 Supernovae

Massive stars ($> 8 M_\odot$) die explosive deaths as core-collapse SNe, releasing 100 times as much energy as the Sun produces in its 10 billion year lifetime. The core-collapse produces a shock wave ejecting the stellar surface at $\sim 10^4 \text{ km s}^{-1}$. The energy in the shocked shell induces nucleosynthesis of elements heavier than Fe. SNe are the most energetic source of feedback injected in GMCs and the surrounding ISM.

Supernovae become important at times $\gtrsim 3 \text{ Myr}$ after the onset of star formation, as this is the lifetime of the most massive stars. Exploding SNe within the cluster will greatly accelerate the expulsion of any gas left embedded in the cluster. If the majority of star formation occurs at early times, SNe may not affect the overall star formation efficiency. There is also some debate as to how many SNe actually explode while embedded in the cluster, as massive stars are frequently ejected from their natal cluster as runaway stars (Fujii and Portegies Zwart, 2011; Hoogerwerf et al., 2000; Poveda et al., 1967).

*Je me détourne avec effroi et horreur
de cette plaie lamentable des fonctions
continues qui n'ont point de dérivées.*

*I turn with terror and horror from
this lamentable scourge of continuous
functions with no derivatives.*

— Charles Hermite¹

2.1 INTRODUCTION

Capturing the vastly different temporal and spatial scales of the copious physical processes in star cluster formation presents a daunting computational challenge. Most models make considerable approximations for the sake of computational capability. For example, many do not model individual stars but rather model sub-clusters of stars with combined feedback and dynamics. This can dramatically change the morphology and efficiency of star formation. Star-by-star models that do follow individual stars are often limited to low and intermediate mass clusters. In this chapter, I present the numerical framework and methods I used to simulate star-by-star high-mass clusters forming from their natal gas clouds.

The TORCH framework (Wall et al., 2020, 2019) uses the Astrophysical MUltipurpose Software Environment (AMUSE) (Pelupessy et al., 2013; Portegies Zwart and McMillan, 2018) which bridges the gap between physical scales by coupling several discrete codes. The MHD code FLASH (Fryxell et al., 2000) models the gas dynamics, sub-grid star formation via sink particles, and stellar feedback in the form of ray-tracing radiation (Baczynski et al., 2015), stellar winds, and SNe. The stellar evolution is tracked by SEBA (Portegies Zwart and Verbunt, 1996).

For this thesis, I have coupled the stellar dynamics code PETAR (Wang et al., 2020a) to TORCH, which also models binary evolution with higher order perturbations. This upgrade increased the manageable number of stars in TORCH from 10^3 to 10^5 . With this updated framework, we ran one of the largest star-by-star models of cluster formation to date.

In the following sections, I describe the numerical methods used in each of the coupled codes in TORCH. They are categorized by: gas

¹ *Correspondance d'Hermite et de Stieltjes (1905)*

(Sect. 2.2), stars (Sect. 2.3), and the interactions coupling gas and stars (Sect. 2.4).

2.2 GAS

2.2.1 Hydrodynamics

Solving the equations of gas dynamics is a fundamental component of simulating star formation in a GMC. The Euler equations of compressible gas dynamics are,

$$\frac{\partial \rho}{\partial t} + \nabla \cdot (\rho \mathbf{v}) = 0 \quad (24)$$

$$\frac{\partial \rho \mathbf{v}}{\partial t} + \nabla \cdot (\rho \mathbf{v} \mathbf{v}) + \nabla P = \rho \mathbf{g} \quad (25)$$

$$\frac{\partial \rho e}{\partial t} + \nabla \cdot [(\rho e + P) \mathbf{v}] = \rho \mathbf{v} \cdot \mathbf{g}, \quad (26)$$

where ρ is density, \mathbf{v} is velocity, P is pressure, $e = u + v^2/2$ is the sum of thermal energy u and kinetic energy per unit mass, and \mathbf{g} is the gravitational acceleration. These three equations describe the conservation of mass, momentum, and energy. Together with the equation of state of an ideal monatomic gas,

$$P = (\gamma - 1)\rho u, \quad (27)$$

where the ratio of specific heats $\gamma = 5/3$, this complete set of partial differential equations can be solved numerically to model hydrodynamics. The Euler equations above ignore the magnetic field for simplicity, but note that `FLASH` solves the full equations of ideal MHD.

Applying numerical methods to solve this system of equations requires spatially dividing the simulation volume. This is done in Eulerian codes by decomposing the domain into a grid of cells. These grid codes then calculate the properties and flow of the gas in each cell over time. The cell size must be small enough to resolve the gas dynamics on scales of the modeled physical process. `FLASH` is an adaptive mesh refinement code (AMR). This means that the Cartesian grid can further refine on cells of interest, doubling the spatial resolution in that cell. This allows for efficient computation of multiscale problems that require a wide range of resolution, as the computation time in a grid code scales linearly with number of cells.

The timestep in a grid code is set by the Courant-Friedrichs-Lewy (CFL) condition (Courant et al., 1967). Solving equations in a mesh with a finite difference scheme introduces a numerical diffusion that must be limited by setting the timestep according to,

$$\text{CFL} = \mathbf{v} \frac{\Delta t}{\Delta x} \leq 1, \quad (28)$$

where Δx is the grid cell size and v is the fluid velocity. Intuitively, this prevents information from propagating across more than one cell boundary in a single time step.

In the finite volume method (FVM), the state of cell i is defined as an average over the cell's volume,

$$\mathbf{U}_i = \frac{1}{V_i} \int_i \mathbf{U}(\mathbf{x}) dV, \quad (29)$$

where the Euler conservation laws have been rewritten in matrix form,

$$\frac{\partial \mathbf{U}}{\partial t} + \nabla \cdot \mathbf{F} = \mathbf{S}. \quad (30)$$

\mathbf{U} , \mathbf{F} , and \mathbf{S} are the state, flux, and source vectors. The volume integral of the flux term in Equation 30 is converted into a surface integral using the divergence theorem and evaluates to the flux of variables across cell boundaries. The flux at cell boundaries represents a *Riemann problem*: an initial value problem of a conservation equation with two piecewise constant initial states that meet at a discontinuity.

The Godunov scheme (Godunov and Bohachevsky, 1959) is an FVM that uses the solution to the Riemann problem at each cell boundary to update cell values after a time interval. The Godunov update formula is:

$$\mathbf{U}_i^{n+1} = \mathbf{U}_i^n + \frac{\Delta t}{\Delta x} [\mathbf{F}_{i-\frac{1}{2}}^* - \mathbf{F}_{i+\frac{1}{2}}^*], \quad (31)$$

with time indexed by n and cells indexed by i . The $\mathbf{F}_{i\pm\frac{1}{2}}^*$ terms are the solutions to the Riemann problem at the cell boundaries. These solutions are calculated with the HLLD Riemann solver (Miyoshi and Kusano, 2005) in FLASH. HLLD is a variant of the original Harten-Lax-van Leer (HLL) solver. HLLD is more accurate than HLL, particularly when solving the equations of ideal MHD.

Solving the Riemann problem at cell boundaries requires interpolation of the cell-centered values to the cell edge. We use the third-order piecewise parabolic method (PPM; Colella and Woodward, 1984). The PPM method uses the values of nearby cells to create a parabolic extrapolation to cell boundaries with a limiter to avoid over/undershoots. If a cell is detected to be within a discontinuity, a linear interpolation is instead used in the zone where the edge values are set equal to the linear interpolations of neighboring cells. This preserves the steepness of the advected discontinuity.

2.2.2 Gravity

The gravitational potential is described by Poisson's equation,

$$\nabla^2 \phi = 4\pi G \rho. \quad (32)$$

We can approximate the spatial derivative of the potential with

$$\frac{\partial^2 \Phi}{\partial x^2} \approx \frac{\Phi_{i+1} - 2\Phi_i + \Phi_{i-1}}{h^2}, \quad (33)$$

where h is the grid spacing and i is the cell index. There are now N equations for the N unknown values of Φ_i , which is a solvable linear set of equations. In matrix form, this set of equations is given by

$$\mathbf{A}\Phi = 4\pi G h^2 \rho, \quad (34)$$

where \mathbf{A} is different depending on whether the problem is in 1D, 2D, or 3D.

Solving this equation directly is computationally expensive, so `FLASH` uses the multigrid method. The basic idea of the multigrid method is to solve Poisson's equation on a coarse mesh to compute a better initial guess for a faster convergence to the solution on the fine mesh. Prolongation and restriction matrices are defined to map the solutions between the different resolution grids. The `FLASH` multigrid solver is detailed in Ricker (2008).

2.2.3 Heating and cooling

We apply heating from stellar radiation by dust absorption and photoelectric electrons, described in see Sect. 2.4.2.1). We also apply a background FUV heating of $0.17G_0$, where $G_0 = 1.6 \times 10^{-3} \text{ erg cm}^{-2}$ is the Habing (1968) flux. We estimate the local visual extinction as $A_v \approx \lambda_J n_H / N_H$ (Seifried et al., 2011; Walch et al., 2015), giving a fraction of background FUV radiation that heats the gas of $f_{bg} = e^{-3.5A_v}$. The cosmic-rays background heating rate per unit volume is given by $\Gamma_{cr} = (20 \text{ eV}) \zeta n_H$ with an ionization rate of $\zeta = 10^{-17} \text{ s}^{-1}$ (Galli and Padovani, 2015).

Atomic, molecular, and dust cooling all contribute to the cooling rate of the gas. `TORCH` uses a piecewise power law for the atomic cooling (Fig. 1, Joungh and Mac Low, 2006), tabulated values for the molecular cooling (Seifried et al., 2011), and dust cooling following the method of Goldsmith (2001) with the cooling equation from Hollenbach and McKee (1989).

2.3 STARS

2.3.1 Sub-grid star formation

The free-fall time (Eq. 16) and Jeans length (Eq. 15) are the characteristic time and length scales for collapse. These scales are much smaller than any reasonable timestep and grid resolution in an entire cluster

formation model. A sub-grid star formation model is needed, and in FLASH this is done via sink particles (Federrath et al., 2010).

The Truelove et al. (1997) criterion requires the Jeans length (Eq. 15) to be resolved by at least four grid cells to avoid artificial fragmentation. This also sets a critical density above which artificial fragmentation occurs. Therefore, the sink accretion radius and threshold density in FLASH is set to $r_{\text{sink}} = 2.5\Delta x$ and $\rho_{\text{sink}} = \frac{\pi c_s^2}{4G r_{\text{sink}}^2}$. The sink density is acquired by solving for ρ in the Jeans length equation.

There are several sink-formation checks done to ensure sink particles only trace gas that is actually star forming and in a state of collapse. These checks find gas within the sphere of radius r_{sink} surrounding cells with gas above ρ_{sink} and ensures that it is:

- maximally refined,
- is converging ($\nabla \cdot v < 0$),
- has a minimum central gravitational potential,
- is bound,
- is Jeans unstable,
- and is not within r_{sink} of another sink.

If these criteria are met, a sink particle is formed with this gas and placed in the center of mass. A sink can further accrete gas from cells within its accretion radius with $\rho \geq \rho_{\text{sink}}$ if the mass is gravitationally bound to the sink. Accretion conserves mass, linear momentum, and angular momentum. The sink's position is moved to the center of mass of the sink+accreted gas system. Sinks are dynamically evolved.

Upon the formation of each sink, a list of stellar masses for the sink to form is sampled from the Kroupa IMF (Eq. 19). This is done by binning the range of sampled stellar masses ($0.08 - 100 M_{\odot}$) into i bins and taking a Poisson sampling of the number of stars in each bin following Sormani et al. (2017). The probability distribution P for a sampling of n stars of total mass M is given by

$$P_i = e^{-\lambda_i} \lambda_i^{n_i} / n_i!, \quad (35)$$

where $\lambda_i = f_i M / \langle m_i \rangle$, f_i is the fraction of total mass in bin i , and $\langle m_i \rangle$ is the average mass in bin i . The number of stars in each bin are given the Poisson sampling, and the mass of the stars are assigned from directly sampling the Kroupa IMF in each bin. The list of stellar masses is then randomized. The sampling size used is $10^4 M_{\odot}$. The advantage of a Poisson sampling is that it can be sampled by any amount of sinks and still reproduce the sampled stellar mass distribution.

With the stellar mass list complete, sinks then form stars going down the list until the sink's mass is depleted. Stars are placed in a

uniform spherical distribution within the sink’s accretion radius. The stellar velocities are set by adding the sink velocity to an isotropic velocity sampled from a Gaussian distribution with $\sigma = c_s$.

2.3.2 Stellar Dynamics

The gravitational force on particle i due to other particles is

$$\mathbf{F}_{g,i} = \sum_{j=0, j \neq i}^N \frac{Gm_i m_j}{r_{ij}^2} \hat{\mathbf{r}}_{ij}. \quad (36)$$

The direct N-body method calculates this quantity accurately by summing over all particle pairs i, j . This results in a computational complexity of $\mathcal{O}(N^2)$. This algorithm quickly becomes infeasible at large N .

The force in Equation 36 can be approximated by using the Barnes-Hut algorithm (Barnes and Hut, 1986), which is much more efficient at order $\mathcal{O}(N \log N)$. In this algorithm, an octree is formed by recursively dividing the domain into cubical cells until only 1 or 0 particles are in each cell. The parent nodes of the tree store the total mass and center of mass of all its child nodes. To calculate the force on a given particle, the algorithm traverses the tree starting at the root node. If the ratio of the node cell width s to the distance between the body and center of mass of the cell d is below a given threshold $s/d < \theta$, then the force of the total mass in that node is added to the total force on the body. Otherwise, the algorithm traverses down the tree until this criteria is met. The algorithm does this for every branch of the root node. Lowering θ increases the accuracy and the computation time, as more nodes will be traversed.

The stellar dynamics code, *PETAR* (Wang et al., 2020a), used in *TORCH* combines both the tree and direct methods to achieve maximum efficiency and accuracy. A changeover radius r_{out} is set, such that for each particle, the gravitational force of other particles within r_{out} are summed with direct N-body and outside that radius are calculated using the Barnes-Hut tree algorithm. The changeover radius is mass dependent such that more massive stars have a larger interaction radius. *PETAR* uses a 4th order Hermite integrator for the direct N-body calculation. This is a predictor-corrector scheme, which extrapolates the acceleration of a particle with a third-order polynomial to get a predicted position and velocity. The predictions are then used in the force calculation to get new accelerations which are interpolated with a fourth-order polynomial to get corrected terms for the position and velocity. The prediction and correction terms are added to get the updated positions and velocities.

Stellar dynamics must also resolve the motion of stars in binaries and higher order systems. This requires the simulation timestep to be much smaller than the orbital time of the binary, which can be on

the order of days. This is unfeasible for star cluster dynamics with timescales of millions of years. `PETAR` solves this issue by defining another radius, `r_bin`, which with to apply the slow-down algorithmic regularization (SDAR; Wang et al., 2020b) for binary evolution and perterbations. SDAR combines the slow-down (SD) method developed by Mikkola and Aarseth (1996) and the algorithmic regularization (AR) method (Mikkola and Tanikawa, 1999; Preto and Tremaine, 1999). SD reduces the integration time for weakly perturbed binaries by scaling down the effective orbital period. This is done by modifying the total Hamiltonian \mathcal{H} of a binary system as

$$\mathcal{H}_{\text{SD}} = \frac{1}{\kappa} \mathcal{H}_{\text{B}} + (\mathcal{H} - \mathcal{H}_{\text{b}}), \quad (37)$$

where \mathcal{H}_{b} is the Hamiltonian of the binary components and κ is the scaling factor such that $T_{\text{bin}} \rightarrow T_{\text{bin}}/\kappa$. The secular the motion of the binary is reproduced, but orbital phase information is lost and large errors occur for highly eccentric orbits. The AR method works to conserve the angular momentum and energy lost in the SD method by applying a time transformation function to the phase-space Hamiltonian.

The short-range forces combine the Hermite and SDAR algorithms, while the long-range force is calculated with the treecode. The long and short-range forces are combined in `PETAR` using the P^3T method (Oshino et al., 2011) of Hamiltonian splitting. The Hamiltonian is split into long and short-range components $\mathcal{H} = \mathcal{H}_{\text{L}} + \mathcal{H}_{\text{S}}$. The new components of the Hamiltonian are defined as

$$\mathcal{H}_{\text{S}} = \sum_{i=1}^N \frac{p_i^2}{2m_i} - \sum_{i<j}^N \frac{Gm_i m_j}{r_{ij}} W(r_{ij}), \quad (38)$$

$$\mathcal{H}_{\text{L}} = \sum_{i<j}^N \frac{Gm_i m_j}{r_{ij}} [1 - W(r_{ij})], \quad (39)$$

where $W(r_{ij})$ is a changeover function ensuring smooth transitions across the changeover boundary between long and short range forces. The changeover function is an eighth-order polynomial (see Eq. 15 of Wang et al., 2020a).

2.3.3 Stellar evolution

Stellar evolution is handled by `SEBA` which evolves stars in `TORCH` from the zero-age main sequence to their stellar death. `SEBA` updates the stellar parameters which are used in the stellar feedback routines (described in Sect. 2.4.2). The stellar wind properties include the mass loss rate and terminal wind velocity (Kudritzki and Puls, 2000; Vink et al., 2000). The radiation properties are the emission ratea and average energy of EUV and FUV photons, respectively. `SEBA` also informs `TORCH` when a star has gone SN.

2.4 GAS-STAR COUPLING

2.4.1 Gravity bridge

The gravitational interaction between stars and gas+sinks is handled with a gravity bridge (Fujii et al., 2007) modified for TORCH in Wall et al. (2019). It is a "kick-drift-kick" leapfrog integration scheme:

1. kick: $v'_n = v_n + \frac{\Delta t}{2} a_n$
2. drift: $x_{n+1}, v'_{n+1} = \text{evolve}(x_n, v'_n, \Delta t)$
3. kick: $v_{n+1} = v'_{n+1} + \frac{\Delta t}{2} a_{n+1}$,

which is done separately for the stars and gas+sinks. The `evolve` step is done by `PETAR` for the stars and `FLASH` for the gas+sinks. For stars, a is the gravitational acceleration due to the gas+sinks using the potential calculated by `FLASH`. For the gas+sinks, the acceleration due to stars is done by a cloud in cell mapping of the stellar masses onto the grid and computing their potential with the same multigrid solver. Using the same solver for all bridge calculations properly conserves momentum.

2.4.2 Stellar feedback

Here I go through the stellar feedback routines in TORCH. These methods are discussed extensively in Wall et al. (2020), and they are abridged here for brevity.

2.4.2.1 Radiation

Radiative feedback from stars affects the gas through ionization, heating and radiation pressure. Radiative transfer is done by the `FERVENT` ray-tracing module (Baczynski et al., 2015) following EUV and FUV frequency bins. EUV photons are responsible for ionizing hydrogen. The fractional hydrogen ionization x due to EUV photons is given by

$$\frac{x}{t} = C_{\text{cl}} n_e x_0 + k_{\text{ion}} x_0 - \alpha_B n_e x, \quad (40)$$

where $C_{\text{cl}}(T)$ is the collisional ionization rate and x_0 is the neutral hydrogen fraction. The rate of photon ionization k_{ion} is given by

$$k_{\text{ion}} = \frac{N_\gamma}{n_{\text{H}_1}(1-x)V\delta t}, \quad (41)$$

where V is the cell volume and δt is the ionization timestep. We are only following the ionization of hydrogen, so we can approximate x with a forward finite difference equation given by

$$\frac{x_{n+1} - x_n}{\delta t} = k_{\text{ion}}(C_{\text{cl}} n_{\text{H}} - k_{\text{ion}}) x_{n+1} - (C_{\text{cl}} + \alpha_B) n_{\text{H}} x_{n+1}^2. \quad (42)$$

The cross section for ionizing photons is given by (Osterbrock and Ferland, 2006)

$$\sigma_{\text{H}} = \sigma_0 \left(\frac{\nu_{\gamma}}{\nu_{\text{ion}}} \right)^{-3}, \quad (43)$$

where $\sigma_0 = 6.304 \times 10^{-18} \text{ cm}^2$ (Draine, 2011). The energy of the ionized electron ($E_e = E_{\gamma} - E_{\text{ion}}$) is added to the cell as heat. After calculating how many EUV photons ionize hydrogen, the rest are subject to absorption by dust. Hydrogen absorption is calculated first because the cross section for H is $\sim 6,000\times$ larger than for dust.

FUV photons in our model have energies in the range 5.6 – 13.6 eV and are subject to absorption by dust. Most FUV photons are not energetic enough to ionize hydrogen, but they impart radiation pressure which is the dominant mechanism for clearing out dense gas around young OB stars. FUV photons are able to penetrate further into the gas than EUV photons due to their smaller cross section. We only allow dust to exist in gas $< 3 \times 10^6 \text{ K}$ where dust would not be destroyed. The dust cross section is given by $\sigma_{\text{d}} = 10^{-21} \text{ cm}^2 \text{ H}^{-1}$, giving an optical depth of $\tau_{\text{d}} = n_{\text{H}} \sigma_{\text{d}} \Delta r$. Here Δr is the path length of the ray. The number of photons absorbed by dust is given by $N_{\text{d}} = N_{\gamma}(1 - e^{-\tau_{\text{d}}})$. The momentum of absorbed photons $h\nu/c$ is added to the gas. Normalizing to the Habing (1968) flux, the FUV flux through a cell is $G = N_{\text{d}} E_{\gamma} / G_0 \Delta x^2 \delta t$. The heating of the gas per unit volume by the corresponding emitted photoelectric electrons is given by $\Gamma_{\text{pe}} = n_{\text{H}} G \epsilon$. We use a heating efficiency function ϵ from Weingartner and Draine (2001), detailed in Eq. 21 of Wall et al. (2020).

Absorbed photons that do not ionize heat the dust, which has a constant fractional density of 0.01 to the gas density. The dust heating rate is taken from Goldsmith (2001) assuming the dust is always optically thin, and the dust temperature is solved with Newton's root-finding method.

2.4.2.2 Stellar winds

Stellar winds deposit density, kinetic energy, and temperature into grid cells within the injection radius. This depends on the radius of the wind termination shock (Eq. 22). If $\Delta x \geq R_1$, the injection radius is set to $6\sqrt{3}\Delta x$, otherwise it is just Δx .

To inject the wind, an overlap fraction ϕ of the spherical injection region and each cell it envelops is calculated and normalized to the volume of the injection region. The injected density and kinetic into a cell is given by

$$\Delta\rho = \phi \frac{\dot{M}\Delta t}{V_{\text{cell}}} \quad (44)$$

$$\Delta E_{\text{w}} = \phi \frac{L_{\text{w}}\Delta t}{V_{\text{cell}}}. \quad (45)$$

The final velocity of the cell is given by $\mathbf{v} = (\Delta\rho\mathbf{v}_w + \rho_{\text{old}}\mathbf{v}_{\text{old}})/(\rho_{\text{old}} + \Delta\rho)$, according to momentum conservation. Mass-loading of the stellar winds is done to lower the temperature of the bubble and raise the CFL timestep (Eq. 28). The wind velocity is lowered such that the pre-shock temperature satisfies

$$T_s = 1.38 \times 10^7 \text{ K} \left(\frac{v_w}{10^3 \text{ km s}^{-1}} \right)^2 < T_{\text{ML}} \quad (46)$$

where T_{ML} is the desired mass-loaded temperature. Mass is added to the injected wind to conserve energy.

2.4.2.3 *Supernovae*

TORCH models Type Ia and Type II supernovae. Following Simpson et al. (2015), the energy input of the supernova is mapped onto the grid using a cloud-in-cell linear interpolation onto a $3 \times 3 \times 3$ cube centered on the SN location. Mass thermal energy, and kinetic energy are evenly divided among all injection cells except in the central cell where all energy is injected thermally. The injection cube is then mapped onto overlapping grid cells.

Part II

PUBLICATIONS

HIGH STAR FORMATION EFFICIENCY WHILE RESOLVING FEEDBACK OF INDIVIDUAL STARS

3.1 ABSTRACT

The mode of star formation that results in the formation of globular clusters and young massive clusters is difficult to constrain through observations. We present models of massive star cluster formation using the TORCH framework, which uses the Astrophysical Multi-purpose Software Environment (AMUSE) to couple distinct multiphysics codes that handle star formation, stellar evolution and dynamics, radiative transfer, and magnetohydrodynamics. We upgraded TORCH by implementing the N-body code PETAR, thereby enabling TORCH to handle massive clusters forming from $10^6 M_{\odot}$ clouds with $\geq 10^5$ individual stars. We present results from TORCH simulations of star clusters forming from 10^4 , 10^5 , and $10^6 M_{\odot}$ turbulent spherical gas clouds (named M4, M5, M6) of radius $R = 11.7$ pc. We find that star formation is highly efficient and becomes more so at a higher cloud mass and surface density. For M4, M5, and M6 with initial surface densities $2.325 \times 10^{1,2,3} M_{\odot} \text{ pc}^{-2}$, after a free-fall time of $t_{\text{ff}} = 6.7, 2.1, 0.67$ Myr, we find that $\sim 30\%$, 40% , and 60% of the cloud mass has formed into stars, respectively. The end of simulation-integrated star formation efficiencies $\epsilon_{\star} = M_{\star}/M_{\text{cloud}}$ for M4, M5, and M6 are 36% , 65% , and 85% . Observations of nearby clusters similar in mass and size to M4 have instantaneous star formation efficiencies of $\epsilon_{\text{inst}} \leq 30\%$, which is slightly lower than the integrated star formation efficiency of M4. The M5 and M6 models represent a different regime of cluster formation that is more appropriate for the conditions in starburst galaxies and gas-rich galaxies at high redshift, and that leads to a significantly higher efficiency of star formation. We argue that young massive clusters build up through short efficient bursts of star formation in regions that are sufficiently dense ($\Sigma \geq 10^2 M_{\odot} \text{ pc}^{-2}$) and massive ($M_{\text{cloud}} \geq 10^5 M_{\odot}$). In such environments, stellar feedback from winds and radiation is not strong enough to counteract the gravity from gas and stars until a majority of the gas has formed into stars.

3.2 INTRODUCTION

Globular clusters (GCs), which are found in every massive galaxy, are some of the most ancient objects in the Universe. They serve as fossils that can reveal the elusive environment and physics of the early

phases of galaxy assembly (Adamo et al., 2020; Brodie and Strader, 2006; Krumholz et al., 2019; Portegies Zwart et al., 2010; Renaud et al., 2017). Yet because of their age, many aspects of cluster formation and evolution at high redshift are challenging to constrain through observation, and little is known about the efficiency and timescale at which gas is converted into stars to create such massive bound clusters.

Though the progenitors of GCs are too old to observe, there are younger star clusters that are as massive as GCs and currently forming in nearby galaxies. These young massive clusters (YMCs) have masses $M \geq 10^4 M_{\odot}$ and ages < 100 Myr (Portegies Zwart et al., 2010). The discovery of these objects has indicated that the mode of extreme star formation that forms massive star clusters still occurs today. Notably, even more of these clusters are being discovered with JWST, as many YMCs in starburst galaxies are too embedded to have been seen by *Hubble* (Whitmore et al., 2023). Although it has been suggested that YMCs are the present day analogs to young GCs, this is debated in the literature (see Renaud 2020).

Theory suggests that, despite the abundance of GCs, $\leq 1\%$ of clusters survive to become GCs (Fall, 2006; Fall et al., 2005; Fall and Zhang, 2001). The conditions that lead to bound star clusters as massive as GCs remain a mystery, and observations of forming YMCs are sparse. Star formation must be fast and efficient enough to form bound stars that can survive the epoch of stellar feedback and the dispersal of the natal gas (Lada and Lada, 2003). The plethora of GCs suggests these conditions were very common in the early Universe.

The process of star formation in a cluster begins with the global gravo-turbulent collapse of giant molecular clouds (GMCs; Larson, 1981). As the collapse proceeds, fragmentation creates overdense clumps within the GMC that begin to form stars (Klessen and Glover, 2016; Mac Low and Klessen, 2004; McKee and Ostriker, 2007). The feedback from these stars, in the form of stellar winds, jets, and radiation, begins to clear out dense gas in and around the forming sub-clusters, slowing down the local (sub-cluster scale) and global (cloud scale) star formation rate (SFR; e.g., Girichidis et al., 2020; Lewis et al., 2023). Eventually, massive stars explode as supernovae (SNe), further dispersing gas. However, it has been argued that the efficiency at which stellar feedback slows global star formation diminishes with higher gas surface density (Grudić et al., 2018b). The sub-clusters eventually merge if they are mutually gravitationally bound, forming a final cluster cleared of all natal gas (Krause et al., 2020).

Many details of star cluster formation remain poorly understood due to the difficulty of modelling such a complex process. Stellar evolution and binary dynamics need to be resolved on timescales of years and distance scales of an AU, while the magnetohydrodynamics (MHD) of the collapsing gas covers regions several parsecs

across, with crossing times of thousands to millions of years. Because of this, most computational star cluster formation models are limited and must make considerable approximations. Many simulations do not form individual stars: some apply stellar feedback as a combined source in the center of the cloud (Dale et al., 2005; Rahner et al., 2019), and others use sink particles representing sub-clusters e.g., Bate et al., 1995; Federrath et al., 2010 or extract the properties and feedback of individual stars from the sink particles (e.g., Grudić et al., 2018; Howard et al., 2017; Kim et al., 2017; Sormani et al., 2017; Su et al., 2018). Other simulations do form single stars, but they do not resolve the stellar feedback of each individual star particle (Colín et al., 2013; Li et al., 2019), instead including feedback from just the sink particles that created the stars. Simulations of dwarf galaxies can capture star cluster mass functions and formation times, but they do so without collisional dynamics of star particles and are therefore unable to accurately capture dynamical properties such as velocity dispersion and size (Andersson et al., 2024; Lahén et al., 2019, 2024).

Modelling individual stars is important, as this can change the efficiency and location of stellar feedback injection. Dynamical processes often eject high-mass stars (Fujii et al., 2022a; Fujii and Portegies Zwart, 2011), and the location of massive stars directly affects how and when gas is dispersed. Gas dispersal stops star formation. Models of sub-cluster feedback may overestimate the strength of feedback, as they do not allow for spatial separation between the stars in the sub-cluster. This lack of separation also changes the morphology of the gas, affecting the number of low-density channels in the gas that can vent thermal energy from the sub-cluster. The degree to which the sub-cluster and star-by-star approaches differ must be constrained.

There are a few models that do evolve individual stars with both stellar feedback and higher order gravitational dynamics (Cournoyer-Cloutier et al., 2021, 2023; Fujii et al., 2022a, 2021, 2022b; Grudić et al., 2021; Lewis et al., 2023; Wall et al., 2020; Wilhelm et al., 2023). While these models include most of the relevant physics, they lack the computational efficiency to simulate star clusters forming from clouds of masses $> 10^5 M_{\odot}$, and instead the models focus on simulating star clusters forming from low-mass clouds $\leq 10^5 M_{\odot}$. This leaves a sizeable gap compared to the observed mass range of GMCs. While clusters with mass $< 10^5 M_{\odot}$ are comparable to Local Group observations, YMC and GC formation is out of their reach. Furthermore, most star formation takes place in GMCs of mass $\geq 10^5 M_{\odot}$ (McKee and Williams, 1997; Murray and Rahman, 2009).

The goal of this work is to model the formation of massive clusters from their initial GMCs while following the formation of individual stars and their feedback. We aim to answer how and in what conditions YMCs can form while remaining bound throughout the onset of gas expulsion. We also seek to understand how efficient the process

of star formation is in a cluster, what the timescale is over which star formation occurs, and whether the clusters formed from these massive clouds survive and remain bound or quickly disperse. We plan to compare our results to those that use a sub-cluster formation and feedback model.

To do this, we used the TORCH framework (Wall et al., 2020, 2019). TORCH employs the Astrophysical Multipurpose Software Environment (AMUSE) framework to couple separate physics codes that handle MHD, radiative transfer, stellar evolution, and N-body dynamics. TORCH uses the MHD code FLASH (Dubey et al., 2014; Fryxell et al., 2000), which accounts for the evolution of the gas and the formation of sink particles and stars. Stellar feedback in the form of winds and SNe is included, and the effect of ionizing and non-ionizing radiation is followed using a ray-tracing approach (Baczynski et al., 2015). The star formation model samples the Kroupa (2002) initial mass function (IMF) to form stars from sink mass reservoirs (Wall et al., 2019). SEBA (Portegies Zwart and Verbunt, 1996) tracks stellar evolution from the zero-age main sequence, and, in the original version of TORCH, PH4 (McMillan et al., 2012) + MULTIPLES (Portegies Zwart and McMillan, 2018) handled the stellar dynamics.

In that version (Wall et al., 2020, 2019), TORCH could not handle the hundreds of thousands of stars that form in massive GMCs $> 10^5 M_{\odot}$. In this work, we solve this problem by making three updates: 1) We replace the combination of the N-body code PH4 and the higher-order interactions MULTIPLES with the code PETAR (Wang et al., 2020a); 2) we agglomerate stars with masses $< 4 M_{\odot}$ into summed-mass dynamic star particles with masses of $\geq 4 M_{\odot}$; and 3) we mass load the stellar winds to reduce the peak temperatures beyond their termination shocks. These modifications enabled TORCH to then model clouds with an initial mass of up to $10^6 M_{\odot}$ that form hundreds of thousands of individual stars.

We present simulations of star clusters forming from turbulent spherical clouds with masses of 10^4 , 10^5 , and $10^6 M_{\odot}$. Each of these clouds is almost identical in terms of their initial properties, with only mass and density scaled between them. Our study investigates whether the formation of YMCs parallels that of low-mass clusters or if it varies significantly with initial cloud mass and density.

This paper is the first in a series exploring the results of these simulations. In this paper, we describe the TORCH code, the new features integrated into TORCH for handling massive GMCs, and the initial conditions of our three clouds in Sect. 3.3. We analyze the time evolution of global gas and stellar properties in Sect. 3.4. In Sect. 3.5, we discuss the results of our analysis, and in Sect. 3.6 we conclude with a summary of the most important results. We provide a data repository containing a sampling of the simulation data corresponding to the panels in Figure 6, the HTML file of the three-dimensional in-

teractive plot shown in Figure 7, and the code used to generate the interactive plot.

3.3 METHODS

3.3.1 *Standard TORCH*

TORCH¹ is built upon the AMUSE framework, which couples multiple autonomous astrophysical codes. We chose codes that allowed efficient calculation of the disparate physical processes at work in star cluster formation.

The TORCH framework incorporates the adaptive mesh refinement MHD code FLASH v4.6.2 (Dubey et al., 2014; Fryxell et al., 2000) with a number of enhancements to the base version of FLASH. The base FLASH handles the MHD and sink particle formation and evolution. The modifications to FLASH presented in Wall et al. (2020, 2019) include heating and cooling, ionization, radiation transfer (using ray-tracing; see Baczynski et al., 2015), and feedback injection from stars. Stellar feedback is implemented in FLASH in the form of ionizing extreme ultraviolet (EUV) and non-ionizing far ultraviolet (FUV) radiation in the form of radiative heating and radiation pressure, as well as mechanical feedback from stellar winds and SNe. FUV rays are terminated when their flux drops below $F_{\text{ray}} \leq 16.9 G_0 e^{-3.5 A_v}$, where A_v is the visual extinction and G_0 is the Habing flux. This cutoff is $10\times$ the applied background FUV field of $F_{\text{ext}} = 1.69 G_0 e^{-3.5 A_v}$ (Draine, 1978). This limits the number of low energy rays on the grid for computational efficiency. We used the HLLD Riemann solver (Miyoshi and Kusano, 2005) in FLASH paired with third-order piecewise parabolic method reconstruction (Colella and Woodward, 1984).

To avoid artificial fragmentation, the Jeans length,

$$\lambda_J = \sqrt{\pi c_s^2 / (G\rho)}, \quad (47)$$

must be resolved by at least four cells (Truelove et al., 1997). We used a refinement criterion of 12 cells per Jeans length along with a derefinement criterion of 24 cells per Jeans length. As density increases during collapse, the Jeans length decreases until this criterion is no longer met at the highest level of AMR refinement. Sink particles were used to collect the gas that exceeds this density. The Truelove criterion sets the sink radius to $R_{\text{sink}} = 2.5\Delta x_{\text{min}}$ and gives the sink threshold density during the entire run as

$$\rho_{\text{sink}} = \frac{\pi c_s^2}{G\lambda_J^2} = \frac{\pi c_s^2}{G(5\Delta x_{\text{min}})^2}, \quad (48)$$

¹ TORCH version used for this work: <https://bitbucket.org/torch-sf/torch/commits/tag/massive-cluster-1.0>

where c_s was evaluated using the initial temperature of the gas. (If the gas heats during the run, the dense gas will be better resolved, making this a worst-case limit for the required density resolution.)

On each time step, the mass of gas within a distance R_{sink} of a sink particle that satisfies the criteria outlined in Federrath et al. (2010) is added to that sink’s mass reservoir for creating stars. When a sink forms, it randomly samples the Kroupa IMF (Kroupa, 2002) and stores a long list of potential star masses to form see also Sormani et al., 2017. Each time step, the sink forms as many stars from this mass list as possible until its current mass reservoir is depleted. It again forms one or more stars the next time it has accreted enough mass for at least the next star on the list. This is the standard stellar mass sampling method used in TORCH (Wall et al., 2019). Star positions are randomly sampled from a uniform spherical distribution within the sink’s accretion radius. Star velocities are set by the sink velocity added to an additional isotropic velocity dispersion with a Gaussian distribution having a standard deviation of the local sound speed.

Star particles are initially formed as zero-age main sequence stars, neglecting pre-main sequence evolution. Subsequent stellar evolution is tracked with SEBA (Portegies Zwart and Verbunt, 1996), which passes the evolutionary properties informing stellar feedback to FLASH. The N-body dynamics of the stars are calculated using PETAR (Wang et al., 2020a), which is discussed further in the next section. Stars dynamically interact with the gas in FLASH through the AMUSE hierarchical coupling (Portegies Zwart et al., 2009) based on the gravity-bridge algorithm of Fujii et al. (2007).

3.3.2 PETAR *N*-body

TORCH was first designed to use the N-body code PH4 (McMillan et al., 2012) to handle direct stellar dynamics, paired with MULTIPLES (Portegies Zwart and McMillan, 2018) to track binary orbital evolution and higher order perturbations. For TORCH runs using an initial cloud of $10^4 M_{\odot}$ and producing only a few thousand stars, this works well. However, the computational cost becomes unfeasible when pushing to higher initial cloud masses that produce far more than 10^4 stars with over a few hundred binary systems. This is because MULTIPLES is a serial Python code, so with many interacting stars computation times become impractical. To speed up TORCH, we replaced PH4 and MULTIPLES with PETAR (Wang et al., 2020a).

PETAR is a state-of-the-art gravitational dynamics code optimized for solving the stellar dynamics of systems with millions of stars. It accomplishes this by dividing gravitational interactions into three regimes: distant interactions calculated with a Barnes and Hut (1986) tree and handled by the framework for developing parallel particle simulation codes (FDPS; Iwasawa et al., 2020, 2016), nearby inter-

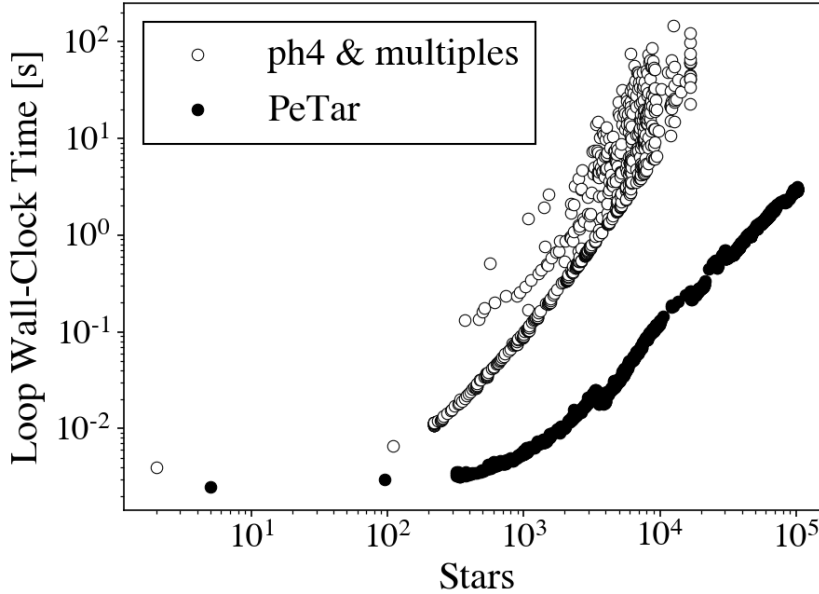


Figure 5: Wall-clock time for an evolution step for PETAR and PH4+MULTIPLES given the number of stars.

actions solved with a fourth-order Hermite direct N-body integrator (Makino and Aarseth, 1992), and close interactions (binaries and higher order systems/perturbations) solved using the Slow Down Algorithmic Regularization (SDAR) technique (Wang et al., 2020b). For each particle, the force from neighboring particles is solved depending on what distance regime they are in, with a mass-dependent factor to increase the distance over which massive particles are considered close neighbors. The SDAR feature for handling higher-order dynamics is the novel component of PETAR, enabling it to handle large numbers of binaries and higher order systems in parallel.

In Figure 5, we plot the wall-clock time per evolution step for each of the N-body codes considered. For reproducibility, this test was done with the parameters $r_{\text{out}} = 0.001$ pc, $r_{\text{bin}} = 100$ AU for PETAR and the stellar interaction radius $r_{\text{int}} = 15 R_{\odot}$ for MULTIPLES. PETAR is significantly faster and consistently performs well as the number of stars increases. The variability in the performance of PH4 and MULTIPLES is due to MULTIPLES taking longer if there are many third-body perturbations in a given step. We note that this test was done with single stars only; the scaling for a run with primordial binaries will be different.

When running PETAR in TORCH, the time step of the long distance particle tree must be set (dt_{soft}), as well as the changeover radius between direct N-body and tree method for force calculations (r_{out}). If the user sets these two parameters, all other parameters are set automatically. In TORCH, the MHD code sets the global time step for

all worker codes based on the Courant condition. The tree time step was set as the nearest power of two in code units below the requested time step, as a power of two is required by PETAR (like most N-body codes). This sets `dt_soft`. For M5 and M6 we set the outer radius `r_out` to 0.001 pc, the standard value used in PETAR simulations. We used a softening length of $\ell = 15 R_{\odot}$ and a binary search radius of $r_{\text{bin}} = 16.5 \text{ AU}$. For M4 we used a larger $r_{\text{out}} = 10 r_{\text{sink}} = 7.8 \text{ pc}$ to ensure accurate force calculations given the small number of stars and low stellar density. This corresponds to $r_{\text{bin}} = 0.63 \text{ pc}$.

The code handling stellar mergers within PETAR is not active within the AMUSE framework, which results in star particles that approach within each others' softening radius and should merge instead ending up with identical positions, leading to a halt in code execution. We have implemented code to check for particles in this state, and merge them. We intended to use SEBA to update the stellar mass of the surviving star, but later testing revealed that the surviving star's mass remained unchanged. One star in the merger is removed meaning that stellar mass is unphysically lost. The effect of this error is negligible due to low merger rates: there are 0, 2, and 4 mergers in M4, M5, and M6, respectively. All of these mergers involve stars $< 7 M_{\odot}$. M5 and M6 lose only $8.4 M_{\odot}$ and $22 M_{\odot}$ of stellar mass due to unphysical mergers over the course of the simulations.

3.3.3 *Stellar modifications*

We made three alterations to the star formation and evolution procedures that vary from standard TORCH to accommodate the several orders of magnitude increase in number of stars formed when increasing the initial cloud mass from $10^4 M_{\odot}$ to $10^6 M_{\odot}$.

- I. We agglomerated low-mass star particles below $M_{\text{agg}} = 4 M_{\odot}$ as they formed until their summed mass is $\geq M_{\text{agg}}$. Then, a star particle is formed with a mass equal to the sum of the low-mass stars. This reduces the strain on the N-body calculations by reducing the number of dynamical star particles by 90%.
- II. We mass-loaded stellar winds to raise the Courant time step by limiting the temperature of wind-blown bubbles to $T_w = 3 \times 10^5 \text{ K}$, which significantly sped up the simulations. This resulted in smaller, cooler, momentum-conserving bubbles instead of hot energy-conserving bubbles. The primary effect of wind feedback in cluster formation is to clear out extremely dense gas in order to allow ionizing radiation to form expanding HII regions. In this dense gas even hot stellar wind bubbles cool quickly, so there is little change in behavior in this regime.
- III. We only injected feedback from stars above $20 M_{\odot}$ to reduce the cost of ray-tracing. Massive stars output most of the ionizing

radiation and mechanical wind energy in clusters: by setting this limit we lost less than 20% of the total feedback energy. Stars below the feedback cutoff mass did not go SN within the time frame of our simulations (≤ 10 Myr).

We further explain and examine the effects of these modifications in Appendix 3.9.2, including providing a quantitative analysis of the amount of total energy lost by excluding feedback for stars $< 20 M_{\odot}$ in the M6 model.

3.3.4 Initial conditions

The initial properties of our three clouds are listed in Tables 3 and 4. We chose to keep the radius of all three clouds constant at $R_{\text{cl}} = 11.7$ pc. The radius was kept the same to have the same spatial distribution of star formation for each run. Constant radius allows the cell resolution and size of sink particles to be the same between the three simulations, and it facilitates directly comparing the morphology and dynamics of the forming clusters.

Consequently, the average initial densities of the clouds are 1.5, 15, and $150 M_{\odot} \text{ pc}^{-3}$, or 10^{-22} , 10^{-21} , and $10^{-20} \text{ g cm}^{-3}$. The column densities of these clouds are $2.325 \times 10^{1,2,3} M_{\odot} \text{ pc}^{-2}$, respectively. Assuming a 9:1 number ratio of H:He, resulting in a mean molecular weight of $\mu = 1.3$, this gives total particle number densities of $n = 46, 460, \text{ and } 4600 \text{ cm}^{-3}$. Each cloud has a column density consistent with observations. Observations show a strong positive correlation between the mass and density of GMCs in PHANGS galaxies (Sun et al., 2022), suggesting mass and density should be varied together.

The initial clouds must be in pressure equilibrium with their surroundings to avoid unphysical shocks from pressure imbalances at their surfaces. The M4 and M5 clouds are in the pressure regime where there is a stable two-phase medium at solar metallicity and Milky Way background UV field (Field et al., 1969; Wolfire et al., 2003), meaning there is a set of temperatures for the cloud and background for a given cloud density where the cold dense cloud and the warm ambient medium are both in thermal equilibrium at equal pressure. The cloud temperatures for the M4 and M5 clouds are $T_{\text{cl}} = 103 \text{ K}$ and 28 K , respectively, and the corresponding background temperatures and number densities are $T_{\text{amb}} = 9,000$ and $4,000 \text{ K}$, and $n_{\text{amb}} = 3$ and 1 cm^{-3} . The M6 cloud, however, is at a high enough pressure that a two-phase medium no longer exists. Only the cold phase can be in thermal equilibrium. This means that the low-density envelope of the M6 cloud is inherently not in thermal equilibrium. To minimize the pressure imbalance with the core, we therefore raised the background density to $n_{\text{amb}} = 100 \text{ cm}^{-3}$. Both the cloud and background medium for M6 are at a temperature of $T_{\text{cl}} = T_{\text{amb}} = 50 \text{ K}$.

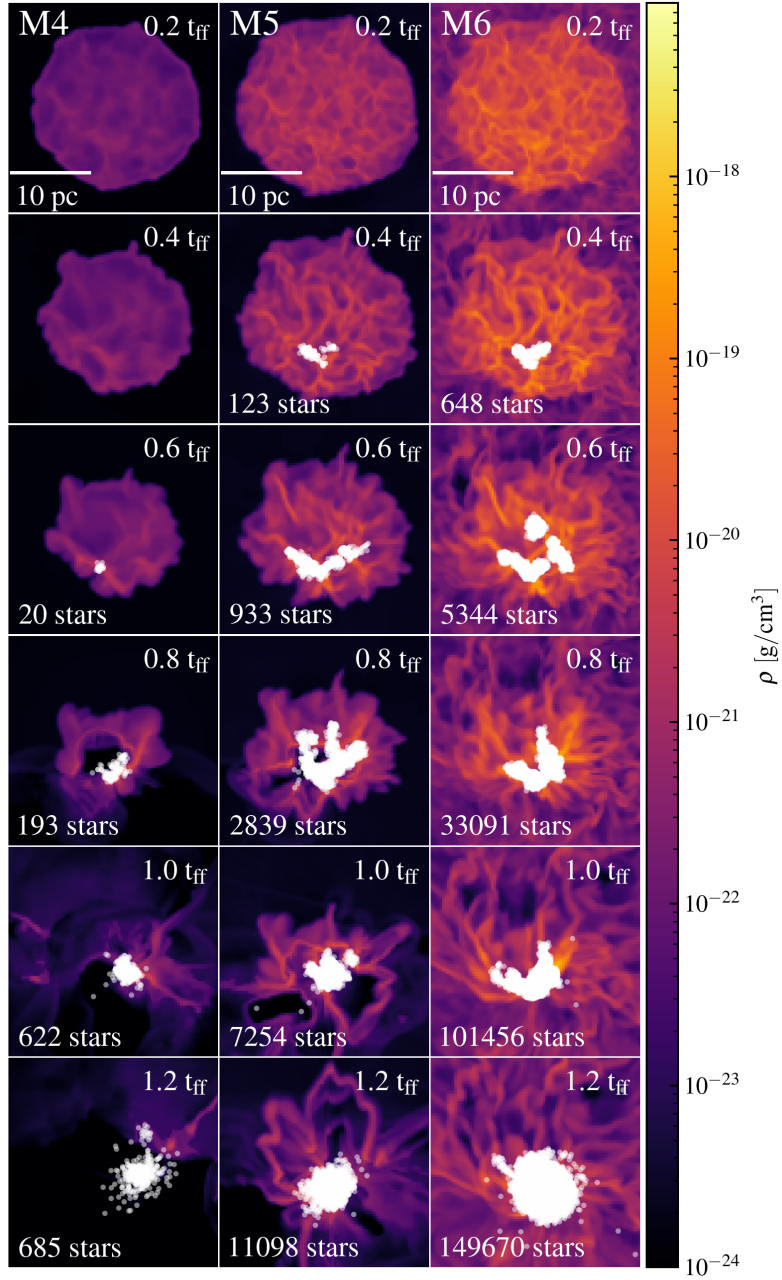


Figure 6: Slice plots of the three simulations in the x - y plane over time. The plane of the slices for a given cloud is the center of stellar mass in the final snapshot. Stellar positions are shown by white dots. The free-fall times t_{ff} are given in Table 3. The number of stars shows the amount of star particles in the domain, not the number sampled from the IMF. Due to our agglomeration of low-mass star particles, the number of stars sampled from the IMF is $\sim 10\times$ greater.

Table 3: Model parameters.

| Parameter | M4 | M5 | M6 |
|---|----------|--------|----------|
| $M_{\text{cl}} [M_{\odot}]$ | 10^4 | 10^5 | 10^6 |
| $\rho_c, \bar{\rho} [M_{\odot} \text{pc}^{-3}]$ | 2.8, 1.5 | 28, 15 | 280, 150 |
| $\Sigma [M_{\odot} \text{pc}^{-2}]$ | 23.25 | 232.5 | 2325 |
| $\lambda_J [\text{pc}]$ | 10.0 | 3.2 | 1.0 |
| $t_{\text{ff}} [\text{Myr}]$ | 6.7 | 2.1 | 0.67 |

Rows: Cloud mass, cloud central and average volume density, initial column density, Jeans length (Eq. 47) at initial temperature, and free-fall time.

Table 4: Control parameters.

| Parameter | Value | Units |
|-------------------------|---------------------|--------------------|
| R_{cloud} | 11.7 | pc |
| R_{box} | 20.0 | pc |
| α_v | 0.15 | - |
| Δx_{min} | 0.3125 | pc |
| Δx_{max} | 1.25 | pc |
| R_{sink} | 0.78125 | pc |
| ρ_{sink} | 8×10^{-21} | g cm^{-3} |
| M_{sink} | 246 | M_{\odot} |
| M_{feedback} | 20 | M_{\odot} |
| $M_{\text{n-body}}$ | 4 | M_{\odot} |
| M_{IMF} | 0.08–100 | M_{\odot} |

Rows: Radius of cloud, half-width of box, virial parameter, minimum cell width, maximum cell width, sink radius, sink threshold density, initial sink mass, minimum feedback star mass, agglomeration mass of low-mass stars, mass sampling range of IMF.

The initial conditions described in the rest of this section and summarized in Table 4 apply to all three clouds. The clouds have a Gaussian density profile (Bate et al., 1995; Goodwin et al., 2004) with the standard deviation set such that the ratio of the cloud’s central to edge density is 3:1. The simulation domain is a cube of half-width $R_{\text{box}} = 20$ pc with outflow boundary conditions. The outflow boundaries do allow gas flow onto the grid from ghost zones if the velocity at the edge of the grid is directed inward. The inflow of gas from the boundary is minimal: more gas exits the simulation than enters in all of our runs. Inflow was allowed, though, to prevent vacuums from forming at the boundaries. We used three refinement levels, yielding cell sizes that range from $\Delta x_{\text{min}} = 0.3125$ pc to $\Delta x_{\text{max}} = 1.25$ pc. Refinement and derefinement of the grid was determined by the Jeans criterion described in Sect. 3.3.1 and based on temperature and pressure gradients. The latter trigger refinement when the adapted Löhner (1987) estimator² of temperature or pressure exceeds 0.98 and trigger derefinement when the estimators drop below 0.6. We are interested in global formation properties of clusters rather than the fragmentation of the cloud or the origin of the IMF, so we find the chosen resolution to be sufficient.

We initially imposed a Kolmogorov, 1941 turbulent velocity spectrum on all the gas in the domain. The peak Mach numbers for the turbulent spectrum are $\text{Ma} = 30.3$ for M6, $\text{Ma} = 12.9$ for M5, and $\text{Ma} = 2.1$ for M4. The same random seed was used to generate the turbulent velocity spectrum for all three clouds. This ensured the same turbulent collapse patterns, minimizing differences in the formation, location, and morphology of dense cores. From the edge of the cloud to the domain boundary, we linearly tapered the magnitude of the turbulent velocities from 100% to 25%. This tapering does not affect the low-density ambient background of the M4 and M5 cloud, but helps with stability in the M6 cloud by mixing the border of the cloud, where there is a small pressure jump.

The sink accretion radius and threshold density, derived in Sect. 3.3.1, are $r_{\text{sink}} = 2.5\Delta x_{\text{min}} = 0.78$ pc and $\rho_{\text{sink}} = 8.35 \times 10^{-21}$ g cm⁻³. This gives an initial sink mass resolution of $m_{\text{sink}} = 245 M_{\odot}$, meaning that when a sink initially forms it will accrete and form approximately m_{sink} worth of stellar mass, given the sink’s threshold density and accretion radius. The IMF sampling mass range is 0.08–100 M_{\odot} . The lower end is the hydrogen-burning limit, while the upper end is the most massive star thought to form in a star cluster with stellar mass $\approx 10^4 M_{\odot}$ (Weidner et al., 2009). This is the expected stellar mass limit for a cluster similar to M4, so we chose this value as a fixed parameter for consistency between the three clusters.

² This is a modified second derivative which is normalized by the average of the gradient over a computational cell.

The critical virial ratio for stability is $\alpha_v = E_{\text{kin}}/|E_{\text{pot}}| = 0.5$, below which collapse occurs. Massive clouds tend to be sub-virial, with clouds of $10^6 M_\odot$ observed to have virial parameters of $\alpha_v \approx 0.05 - 0.35$ (Kauffmann et al., 2013), though some surveys see super-virial massive clouds (see Fig. 2 of Chevance et al., 2023). We note that these values have been converted from the different virial parameter definition in Kauffmann et al., 2013. Therefore, we chose a fiducial virial parameter value of $\alpha_v = 0.15$ for our models to promote rapid onset of collapse.

Magnetic fields are prevalent in the interstellar medium (Crutcher et al., 2003) and affect the collapse of GMCs and subsequent star formation. Although they are not the dominant factor in determining how star formation proceeds within a cloud, their presence has been shown to alter the fragmentation of cores (Peters et al., 2011; Price and Bate, 2008) and slow down the global evolution of the cloud (Heitsch et al., 2001). With a strong enough field, clouds can be supported against gravitational collapse (Heiles, 1976), although generally observed magnetic fields are not strong enough to inhibit collapse (Klessen and Glover, 2016). The critical value of the mass-to-flux ratio for a cloud to be supported by magnetic fields against gravitational collapse is given by (Mouschovias and Spitzer, 1976; Mouschovias, 1991)

$$\left[\frac{M}{\Phi}\right]_c = \frac{\zeta}{3\pi} \sqrt{\frac{5}{G}} = 490 \frac{\text{g}}{\text{Gauss cm}^2}, \quad (49)$$

where G is the gravitational constant and a correction factor $\zeta = 0.53$ for a uniform sphere is used (Strittmatter, 1966).

In our simulations, each cloud's initial magnetic field $\vec{B} = B_z \hat{z}$ is uniform in z and decreases radially in the x - y plane, following the mid-plane density $\rho(x, y, z = 0)$ as

$$B_z(x, y) = B_0 \exp[-(x^2 + y^2) \ln(3)/R_{\text{cl}}^2], \quad (50)$$

with $B_0 = 0.185, 1.85, 18.5$ —G for the M4, M5, and M6 clouds, respectively. These values match observations for M5 and M6, while the field is a factor 10 weaker for M4 (Crutcher et al., 2010). The integrated magnetic flux $\Phi = 2\pi B_0 R_{\text{cl}}^2 / (3 \ln(3))$, so all clouds have an initial mass-to-flux ratio $M_{\text{cl}}/\Phi = 4.5 \times 10^4 \text{ g Gauss}^{-1} \text{ cm}^{-2}$ much larger than Equation (49). The initial magnetic fields are thus weak and do not inhibit collapse in any of our simulations.

3.4 RESULTS

3.4.1 Cluster formation overview

At the onset of the simulation, each cloud begins to gravitationally collapse. Turbulent velocities fragment the cloud and create overdense

hubs and filaments. Because the same random seed was used in all three clouds to generate the initial turbulent velocity spectrum, the web of dense gas is the same for each cloud. This means that the spatial distribution of star formation is similar for all three clouds. This can be seen in the time evolution of the three clouds in Figure 6. The first stars all form in the largest over-density in the middle of the bottom of the cloud. Then, more stars form along the filaments of the dense cloud forming a V shape. The M5 and M6 clusters in particular look very similar in terms of sub-clustering and merging. The M4 cluster forms significantly fewer stars and therefore fewer sub-clusters.

By a free-fall time t_{ff} , the sub-clusters in M4 and M5 have mostly merged, forming a single central spherical cluster. The M6 model is still forming stars in various sub-clusters and has not assembled its main central cluster yet. By looking at the spatial distribution of sub-clusters and the density of the gas, one can see that stellar feedback becomes most efficient once the sub-clusters have merged into a single cluster. Whether feedback is only strong enough to disperse gas when clustered or this is coincidental with the timing of feedback needs further examination, but this is outside of the scope of this introductory paper. Low density bubbles begin to occupy a significant fraction of the cloud volume once the central star cluster has been assembled.

Once most of the stars have formed, the efficiency of stellar feedback for dispersing the natal gas varies greatly for the three cloud masses. The final row in Figure 6 shows the M4, M5, and M6 systems at $1.2t_{\text{ff}}$. At this point, only the M4 and M5 clusters have blown large bubbles. The feedback from the M6 cluster has hardly slowed the collapse of the densest gas, and rapid star formation continues. The M4 cloud has dispersed nearly all of the remaining gas, and star formation has halted completely.

3.4.2 *Visualizing cluster morphology*

The complex 3D structure of star clusters is hard to visualize using 2D plots. Figure 7 shows a still of an interactive plot of the M4, M5, and M6 simulations after one free-fall time generated with Plotly (Plotly Technologies Inc., 2015). After downloading the HTML file available in the online version of this paper, readers can zoom, pan, and rotate for a complete look at the morphology of each cluster. The color is an isosurface of the gas density in log scale, and the points are stars with sizes scaled to their stellar radius. This tool makes it clear just how non-spherical these clusters are. Comparing the still of the interactive plot to the slice plots in Figure 6, one can already extract much more information on the system's morphology.

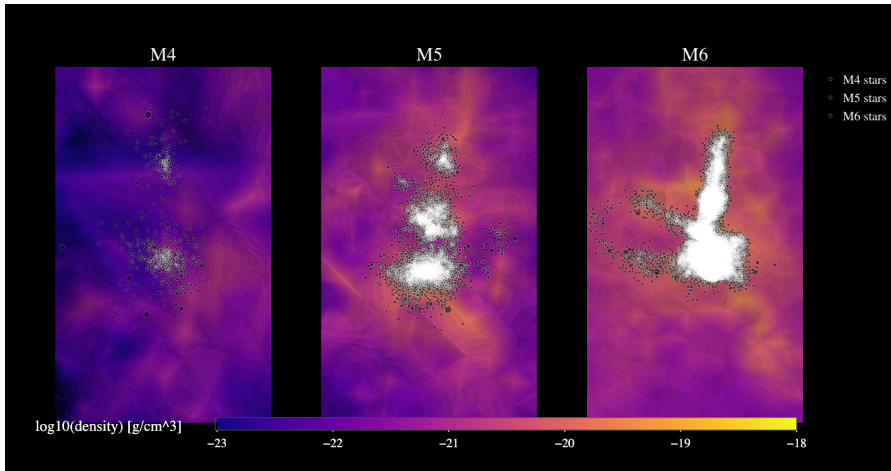


Figure 7: Still of the interactive plot of the embedded M₄, M₅, and M₆ clusters (left to right) at $1 t_{\text{ff}}$. The interactive plot file is available for download from the repository.

Zooming into the core of each cluster shows the immense stellar density of the M₆ cluster, whereas in the M₄ cluster one can easily distinguish individual stars. The gas is also far less dense in the M₄ system compared to M₅ and M₆.

The shape of the M₆ cluster is highly irregular. Stemming from the largest cluster, one can see a row of sub-clusters forming along a filament. Branching perpendicularly off this filamentary cluster are two more star forming filaments in a configuration resembling the letter “F.” The M₅ cluster has a shape congruous to the shape of M₆, but with fewer stars bridging the gaps between clusters in the main filament. The M₅ cluster also has only one finger perpendicular to the main filament, which contains many fewer stars than the fingers of the M₆ cluster. The M₄ cluster is much less dense, with its few stars outlining the same core filament cluster seen in M₅ and M₆. However, in M₄ sub-clusters can no longer be distinguished. The M₄ sub-clusters already merged into a singular central cluster.

3.4.3 Star formation history

The global properties of the star clusters that form from the M₄, M₅, and M₆ clouds over the period of star formation are shown in Figure 8 as a function of time in units of the global free-fall time of the cloud t_{ff} (see Table 3). For reference, this same figure is shown as a function of physical time in Appendix 3.9.1. We analyze these properties and discuss how they compare across the three clouds to assess the effect of the initial cloud mass and density on the resultant cluster properties. Table 5 highlights the final properties of the clusters formed in the three models.

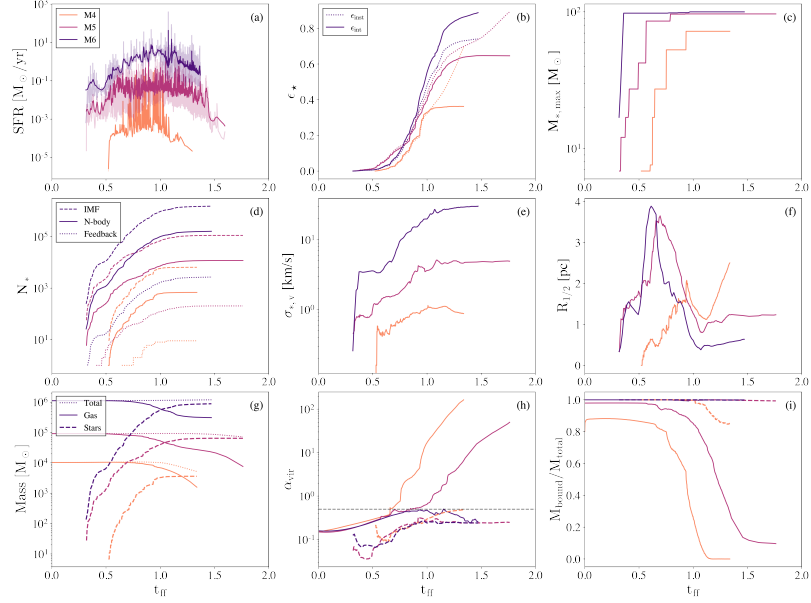


Figure 8: Global properties of the clusters and gas over time for models M4 (orange), M5 (maroon), and M6 (blue-violet) in units of free-fall time t_{ff} of the initial cloud (given in Table 3). From top left to bottom right: (a) SFR, where the transparent lines show the SFR at each star formation event, and the solid lines give the SFR smoothed using a Gaussian filter with $\sigma = 0.005t_{\text{ff}}$. (b) Instantaneous and integrated SFEs of the clouds, where $\epsilon_{\text{inst}} = M_{\star}/(M_{\text{gas}} + M_{\text{sink}} + M_{\star})$ and $\epsilon_{\text{int}} = M_{\star}/M_{\text{cloud}} = \epsilon_{\star}$. (c) Most massive star formed. (d) Number of formed stars. *Dashed line:* actual number of stars that would form from sampling the IMF given the amount of gas mass collected for star formation by sink particles. *Solid line:* number of stars followed in TORCH after the sampled stellar population below $4 M_{\odot}$ has been agglomerated. *Dotted line:* number of stars above $20 M_{\odot}$ on the grid that are generating feedback. The number of stars can drop due to SN, mass loss, or exiting the grid. (e) 3D stellar velocity dispersion. (f) Half-mass radius of the entire star cluster. (g) Total mass (*dotted line*), mass of stars (*dashed line*) and gas (*solid line*) on the grid. (h) Virial parameter of stars (*dashed line*) and gas (*solid line*), where $\alpha_{\text{v}} = 0.5$ is the equilibrium value. (i) Fraction of mass bound for stars (*dotted line*) and gas (*solid line*).

Our results suggest that star formation in a GMC is a fast and efficient process regardless of initial cloud mass and density, with all three clouds converting at least 30% of their initial gas into stars within an initial free-fall time. Star formation becomes faster and more efficient as the mass and density of the GMC increases.

Stars begin forming in the M5 and M6 clouds at $t = 0.3 t_{\text{ff}}$, while in the M4 run it is delayed until $t = 0.5 t_{\text{ff}}$. Because of the turbulent field, regions of the clouds have locally shorter free-fall times leading to star formation earlier than the global free-fall time. The duration of star formation is the shortest for the M4 cloud, lasting $t_{\text{sf}} = 0.7 t_{\text{ff}}$. The M5 cloud forms stars for a longer period in terms of its initial free-fall time, $t_{\text{sf}} = 1.3 t_{\text{ff}}$. M6 is still forming stars $1.3 t_{\text{ff}}$ after the onset of SF.

The SFR (Fig. 8(a)) increases with cloud mass. The peak SFR for the M4, M5, and M6 clouds are $\text{SFR}_{\text{peak}} = 0.4, 5.5,$ and $392 M_{\odot} \text{ yr}^{-1}$ respectively. The average SFRs also increase with mass, with values of $\text{SFR}_{\text{ave}} = 0.02, 0.06,$ and $1.5 M_{\odot} \text{ yr}^{-1}$.

The integrated star formation efficiency (SFE; Fig. 8(b)) we discuss here is given by the ratio of stellar mass formed to the initial gas mass of the cloud $\epsilon_{\star} = M_{\star}/M_{\text{cloud}}$. The instantaneous SFE is the ratio of stars to the total mass on the grid at that point in time $\epsilon_{\text{inst}} = M_{\star}/(M_{\text{gas}} + M_{\text{sink}} + M_{\star})$.

For all three clouds, the instantaneous and integrated SFE closely follow each other at early times. In the M4 track, they diverge at $t \sim 1 t_{\text{ff}}$: ϵ_{inst} increases from 35 to 70%, while ϵ_{\star} levels out due to gas expulsion. When all gas is fully expelled from the domain all three values will converge to $\epsilon_{\text{inst}} = 100\%$. The instantaneous SFE for M5 is beginning to increase toward 100% as the integrated SFE levels out. The ϵ_{inst} for M6, however, levels out $\approx 10\%$ lower than ϵ_{\star} . This is due to the higher background density and some inflow from the boundary. Inflow is expected to occur for systems like M6, so this suggests observed SFEs of massive embedded clusters may be lower than the conversion ratio of gas to stars from the original cloud. For consistency, the best estimate for simulated SFE is the final integrated SFE value, and this is the value we use for all further comparisons to observations. We delve into the limitations of comparing observed and modelled SFEs in Sect. 3.5.1.

The M4 cloud is representative of typical GMCs at the solar circle, and its integrated SFE lies just over the top of this range at 36%. Typical SFE values of nearby clusters in the Milky Way lie between 0.1–0.3 (Lada and Lada, 2003). In the higher mass clouds of M5 and M6, the SFE is much higher. The M5 cloud converted 65% of its gas into stars, and the M6 cloud converted 89% of gas into stars. This suggests that the SFE in high-mass, high-density environments can be much higher than seen in low-mass local clusters.

The free-fall time becomes so short in these high-mass clouds that the stellar feedback simply does not act quickly enough to stop star formation before most of the gas has formed into stars. Free-fall times of dense environments that are shorter than the development times for winds and SNe have indeed been shown to result in high SFE (Dekel et al., 2023). However, the more crucial factor may be that the total force budget of feedback from winds and radiation is not enough to surpass the gravity from gas and stars in dense, high-mass embedded clusters. This force-balance argument is supported by our results presented in Sect. 3.5.1 where the stellar feedback in a 1D model of M6 fails to expel gas from the embedded cluster’s potential well. Regardless of free-fall time, in high density clouds the total feedback energy won’t equal gravity until over half the cloud mass is converted to stars. However, if the free-fall time becomes so long ($t_{\text{ff}} \geq 10$ Myr) that SNe become a dominant form of feedback during the primary epoch of star formation, the energy from frequent SNe may start to overpower gravity and affect the SFE. We have not explored this regime, as such a high free-fall time for a $10^6 M_{\odot}$ cloud is rare.

Figure 8(c) shows the mass of the most massive star that has formed from random draws from the IMF. By a free-fall time, each cloud has already formed the most massive star in its cluster. We find that the mass of the most massive star increases with cluster mass. For the M5 and M6 clouds, the most massive star is at the maximum sampling mass of $100 M_{\odot}$, while the M4 cloud’s most massive star is around $70 M_{\odot}$. This is a stochastic effect; as more stars are sampled from the IMF, you will eventually sample the most massive star in the distribution. This reproduces the effect suggested by Weidner et al. (2009) and Yan et al. (2023) that the cluster mass limits the most massive star mass. In each cloud, it is interesting to note that each instance of the formation of a very massive star, that is, above $40 M_{\odot}$, correlates with a slowing of star formation indicated by a reduction in the SFE slope.

The M6 cloud forms from IMF sampling $\sim 10^6$ stars, M5 forms $\sim 10^5$ stars, and M4 forms $\sim 10^4$ stars, shown in Figure 8(d). With agglomeration, the number of stars in the simulation are about 10% of these numbers, so the improved version of TORCH with PETAR can simulate clusters of $> 10^5$ individual stars.

3.4.4 Cluster evolution

The evolution of the global properties of the formed star clusters occurs quite similarly for all three clouds, but the magnitude of their values depends greatly on the cloud’s initial mass.

The stellar velocity dispersion (Fig. 8(e)) generally increases with initial cloud mass. The velocities of stars increase at a slow pace be-

fore leveling out after $1 t_{\text{ff}}$. For the M4 cluster, the velocity dispersion levels out at just 1.0 km s^{-1} . At late times, the velocities of the stars begin to slightly decrease in M4. This decrease correlates to the increasing half-mass radius of M4, indicating the star cluster is expanding and the stellar velocities are slowing. The M5 cluster reaches a velocity dispersion of 5 km s^{-1} and the M6 cluster has a velocity dispersion of 20 km s^{-1} . The deeper potential wells of the higher mass clusters, going as the square root of the mass for these similar sized objects, drive the higher velocity dispersions, although the measured dispersion increases somewhat faster with mass than the potential well depth. In the case of M6, the potential well depth exceeds the sound speed of ionized gas, preventing gas from escaping even after ionization. For M6, the average sound speed in cells where the gas is fully ionized is $c_{\text{ion}} = 16.4 \text{ km s}^{-1}$.

The evolution of the half-mass radius $R_{1/2}$ of all the stars in the cluster (Fig. 8(f)) seems to be split into a high and low-mass regime. The M5 and M6 clusters follow the same track closely. From $0.3 t_{\text{ff}}$ to $1.0 t_{\text{ff}}$, $R_{1/2}$ increases to a peak of $\sim 3.75 \text{ pc}$ at $\sim 0.6 t_{\text{ff}}$ then goes down to $\sim 1 \text{ pc}$ (M5) and $\sim 0.5 \text{ pc}$ (M6) and begins to level out. The similarities in the evolution of the two clusters are most likely due to the fact that both clouds at early times form enough stars for distinct sub-clusters to form and merge. The sub-clusters have formed in the same places so both clusters peak at roughly the same $R_{1/2}$. All of the stars in M5 and M6 remain bound, suggesting the clusters are relaxing into gravitational equilibrium. Longer runs following just the stars after gas dispersal will ultimately be needed to demonstrate this. M6 is a smaller and denser cluster than M5, likely due to the much deeper potential well of M6. Similar stellar densities are observed in the super-star clusters (SSCs) of starburst NGC 253 (Rico-Villas et al., 2020) with sizes of $R < 1.7 \text{ pc}$ and stellar masses of $10^{4-6} M_{\odot}$.

The M4 cluster grows slightly differently. It increases to a peak of $R_{1/2} = 2 \text{ pc}$ at $1 t_{\text{ff}}$, decreases to $R_{1/2} = 1 \text{ pc}$, then linearly increases to 2.5 pc by $1.3 t_{\text{ff}}$. The M4 cluster is expanding, but 85% of its stars remain bound, so complete dissolution has not yet occurred (Fig. 8(i)).

The onset and duration of gas dispersal from the star clusters depends strongly on the initial mass and density of the cloud. Figure 8(g-i) shows the time evolution of the mass, virial parameter, and bound mass fraction of the gas and stars. With these three plots we can track the degree of gas dispersal. From the mass plot we see that by the end of star formation, the M4 and M5 clusters have expelled a significant fraction of the initial cloud. Only 10% of the original gas mass remains in M4 and $< 10\%$ in M5. Both M4 and M5 are well on their way to full gas expulsion, as in both clusters $< 10\%$ of the gas still on the grid is bound. The gas in the M4 and M5 systems become super-virial by a free-fall time. The gas in M5 takes $\sim 10\%$ longer to become unbound, but progresses identically to the M4 gas. The gas in

Table 5: Results.

| Run | M_* | N_* | ϵ_* | $\langle \text{SFR} \rangle$ | SFR_{pk} |
|-----|---------|-----------|--------------|------------------------------|--------------------------|
| M4 | 3,628 | 6,488 | 0.36 | 0.022 | 0.4 |
| M5 | 64,733 | 112,661 | 0.65 | 0.063 | 5.535 |
| M6 | 845,815 | 1,468,969 | 0.85 | 1.530 | 392.0 |

Column values and units: Stellar mass [M_\odot], number of stars formed from IMF sampling (number of stars in the simulation after agglomeration of stars $< 4 M_\odot$ is $\sim 10\%$ of this value), integrated SFE [M_*/M_{cloud}], average SFR [$M_\odot \text{ yr}^{-1}$], peak SFR [$M_\odot \text{ yr}^{-1}$].

M6 differs significantly as it remains sub-virial even beyond one free-fall time. The potential well created by the massive cluster is enough to keep the remaining gas infalling, suggesting star formation is not yet quenched in the M6 cluster.

The only star cluster that is starting to disperse is the M4 cluster (Fig. 8(i)). The other two star clusters remain fully bound. The stars in M5 and M6 remain sub-virial, while the stars in M4 just reach virial equilibrium by the final simulation time (Fig. 8(h)). The dispersal time of the gas and stars increases with initial cloud mass as there is more gravity for the stellar feedback to counteract. Although massive clusters have more stars injecting feedback, the increasing gravity overpowers the feedback. At high densities, where the potential well depth exceeds the sound speed of ionized gas, ionization feedback cannot disperse gas, while the short free-fall time assembles dense gas more quickly than feedback can work against gravity.

3.5 DISCUSSION

3.5.1 *Limitations of comparing observed and modelled star formation efficiencies*

We compare the SFEs of our modelled clusters to observations by using the integrated quantity ϵ_* , the stellar mass divided by the initial cloud mass. This is the total fraction of cloud mass that has been converted into stars. However, this value is impossible to calculate for observed clusters, as the only information available is how much gas and stars are present within a certain area. Thus, observations of star clusters only quote the instantaneous value ϵ_{inst} . There is a 3–4 order of magnitude spread in the observed SFE and SFR of Galactic GMCs (Lee et al., 2016).

A proper comparison between simulated and observed SFEs requires accounting for the amount of ongoing star formation, and determining whether the embedding gas is collapsing or dispersing.

Comparisons done without accounting for the evolutionary stage of the cluster are misleading. The apparent SFE ranges from 0–100% over the lifetime of every star cluster that reaches a gas-free state, which may explain the spread in observed SFE. This issue is starting to be explored. Geen et al. (2017) suggest techniques for converting observed to integrated SFEs, although conclude that this is non-trivial and find errors up to a factor of 10. They find overall higher observed SFEs than integrated SFEs when they applied observational techniques to their simulations. On the other hand, Grudić et al. (2019) find lower observed than integrated SFEs in their models due to the inaccuracies of techniques for estimating stellar mass. One example of this comes from using only the young stellar population as a tracer for stellar mass, which underestimates the total stellar mass. They also discuss variability in observed SFEs due to the changing SFE over the course of a GMC lifetime, from first star formation to gas dispersal.

Further studies must be dedicated to outlining a systematic way to convert between observed SFEs and the final integrated SFEs we define in our models. Until then, direct comparisons should be interpreted with caution.

3.5.2 Observations

Galactic surveys of embedded clusters in the Milky Way typically find the SFE to be $\lesssim 30\%$ (Lada and Lada, 2003), with some studies finding lower values of $\lesssim 8\%$ (Evans et al., 2009; Peters et al., 2011). The M4 cloud, which is a good representative of galactic GMCs³, agrees well with this SFE albeit at the high end of observed values. This could be due to the low virial parameter used, which is appropriate for M6 but lower than the average observed value of $\alpha_v = 1$ seen in clouds similar to M4. The missing radiative feedback from stars $< 20 M_\odot$ could also be a factor causing the high SFE of M4 given the low-density of the cloud. Feedback contributions from low-mass stars could be a key factor in quenching star formation in Milky Way-like clouds.

The higher mass clouds similar to M5 and M6, however, have SFEs well above 30%. While there are no Milky-Way analogs to the M6 cloud, there are a few for M5. There is the W43 GMC with $1.32 \times 10^5 M_\odot$ of gas within $R \sim 10$ pc (Lin et al., 2016), similar to the M5 cloud with $R = 11.7$ pc. The W49 star forming region has a central YMC with stellar mass $\gtrsim 5 \times 10^4 M_\odot$ and gas mass $\sim 2 \times 10^5 M_\odot$ and $\sim 1.1 \times 10^6 M_\odot$ within 6 and 60 pc respectively (Galván-Madrid et al., 2013). This gives a current SFE of 20% in the inner region. W49 has ongoing star formation, and its embedded gas cloud is twice as massive and 15 times as dense as our M5 model. Based on our results

³ See Rice et al. (2016) for a catalog of Milky-Way molecular cloud properties.

Table 6: Properties of observed super star clusters.

| galaxy | NGC 5253 | NGC 253 | NGC 4945 |
|--------------------------|---------------------------------|--------------|----------------|
| type | dwarf | starburst | starburst |
| $M_{\star} [M_{\odot}]$ | $1.1^{+0.7}_{-0.2} \times 10^6$ | 10^{4-6} | $10^{4.6-5.7}$ |
| R [pc] | 28×52 | $0.34 - 1.7$ | $1.4 - 4.0$ |
| ϵ_{inst} | $61^{+84}_{-16}\%$ | $30 - 90\%$ | $> 50\%$ |
| N_{SSC} | 1 | 12 | 27 |

Characteristics of super star clusters in the galaxies NGC 5253 (Turner et al., 2015), NGC 253 (Leroy et al., 2018; Rico-Villas et al., 2020), and NGC 4945 (Emig et al., 2020).

for M5 and the fact that SFE increases with density, we predict W49 will exceed the SFE found for M5 of $\epsilon_{\star} = 65\%$.

Though conditions required to form the M6 cloud are not observed in the Milky Way, they are present in other galaxies. Starburst galaxies have been observed to host SSCs with SFEs of $\epsilon_{\text{inst}} \approx 50 - 80\%$. These SSCs cover a size and mass range comparable to our models (see Table 6).

Additionally, the disks of gas-rich high redshift galaxies can be violently unstable and are thought to form clouds similar to M6 (see Tacconi et al., 2020). We can now directly observe the high redshift environment of forming GCs with JWST. (Li et al., 2024) predicts JWST will find feedback-free starbursts (Dekel et al., 2023), which are massive galaxies at $z \gtrsim 10$ with high SFEs due to dense gas with free-fall times ≤ 10 Myr forming stars effectively free of stellar feedback. Recent JWST observations uncovered “younger” populations of GCs in galaxies at redshift $z = 0.38$ (Harris and Reina-Campos, 2023), and others are expected to observe GCs up to $z = 1$ without lensing (Reina-Campos and Harris, 2024).

With lensing, clumps that are likely proto-GCs can be observed at redshift $z > 1$ (Adamo et al., 2023; Claeysens et al., 2023). One such proto-GC candidate was found through lensing at $z \sim 6$ with $\lesssim 10^6 M_{\odot}$ and a core radius of $R_c < 13$ pc (Vanzella et al., 2019). Another more massive bound YMC 3 Myr old was found at $z = 2.37$ with $\sim 10^7 M_{\odot}$, and $R \sim 8$ pc (Vanzella et al., 2022b). A strongly lensed galaxy at $z = 4$ contains three bound YMCs each younger than < 30 Myr with masses between $(0.7-4.0) \times 10^6 M_{\odot}$ and radius estimates of 3–20 pc (Vanzella et al., 2022a). The Sunrise arc is a strongly lensed $z \approx 6$ galaxy found to contain six YMCs with masses $\sim 10^{6-7} M_{\odot}$, radii of $\sim 1-20$ pc, and ages 1–30 Myr (Vanzella et al., 2023). Most of these recently discovered YMCs or proto-GCs are analogous in size and mass to the M6 cluster or larger. Dense regions of prolific star formation that form these objects seem pervasive in the early

Universe, and more will surely be discovered as more JWST data arrives. Due to their similar properties, we argue that these clusters formed in the same manner as M6.

Another situation that can form GMCs similar to M6 is major galaxy mergers with small mass ratios. Tidal interactions of major galaxies are linked to bursts in star formation (Barton et al., 2000; Ellison et al., 2008; Larson and Tinsley, 1978; Lonsdale et al., 1984; Renaud et al., 2019). Since most massive galaxies are believed to undergo at least one merger in their lifetime, this is not a rare occurrence. Galaxy mergers have been suggested as the progenitors of YMCs and younger GCs (Ashman and Zepf, 1992; van den Bergh, 2001). We note that this only applies to major galaxy interactions: minor galaxy interactions with large mass ratios produce little to no enhancement of the overall SFR (Cox et al., 2008; Tress et al., 2020).

In the interacting Antennae galaxies, the Firecracker cloud, which resembles M6, was observed by Whitmore et al. (2014). Finn et al. (2019) constrains its mass and characteristic radius to $(1-9) \times 10^6 M_{\odot}$ and 22 pc. The Firecracker cloud is in the very early stages of star formation, as it is estimated to have only formed $M_{\star} \lesssim 10^4 M_{\odot}$. This is less than 10% of the expected stellar mass of the final star cluster (Johnson et al., 2015). These observations show that progenitor clouds similar to M6 can form before any significant amount of star formation occurs.

A survey of the molecular clouds in the Antennae galaxies done by Wei et al. (2012) revealed two populations of MCs, with a distinct break in the differential mass function at $\log(M_{\text{cloud}}/M_{\odot}) = 6.5$. Clouds above this mass were found in the regions of intense star formation, while the lower mass clouds were in more dormant regions. The large velocities seen in the high SF regions suggest compression by shocks, supporting the idea that galaxy mergers lead to high-mass GMCs that become sites of extreme star formation.

Finn et al. (2019) measured the velocity dispersion in the Firecracker cloud and found it to be neither in virial equilibrium nor free-fall. They conclude that there must be a high pressure background to contain the gas at such high densities in equilibrium.

We compare this velocity dispersion to those in our clouds over time to test whether we reach such high velocities through the addition of stellar feedback to free-fall collapse alone or whether a high pressure background is indeed needed. The results of this comparison are shown in Figure 9. We plot the size–line width coefficient σ_v^2/R against surface density $\Sigma = M/\pi R^2$ for each of our clouds to compare with the observations from Finn et al. (2019). The observations are shown by the red points in Figure 9 corresponding to 4 aperture sizes they used for R: 6.4, 15, 26, and 37 pc. We use four smaller aperture sizes: 5, 10, 15, and 20 pc, as our cloud is half the radius of the Firecracker. We plot four times for each of our simula-

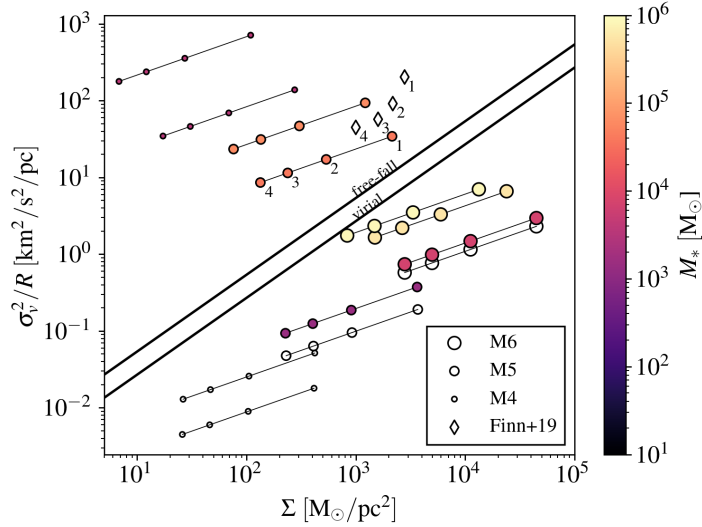


Figure 9: Size-line width coefficient versus surface density for the Firecracker cloud (Finn et al., 2019) and the M4, M5, and M6 clouds. The four red diamonds are observations, done using apertures (1–4) with radii $R = 6.4, 15, 26,$ and 37 pc. The other points are our simulations, with connected points corresponding to apertures (1–4) of radii $R = 5, 10, 15$ and 20 pc. The colors indicate how much stellar mass has been produced (with empty points indicating no star formation). The lines correspond to virial equilibrium and free-fall as labeled (see Fig. 2 of Ballesteros-Paredes et al., 2011).

tions corresponding to $t = 0.0, 0.5, 1.0, 1.25 t_{\text{ff}}$, with a line connecting the points showing the set of apertures. The apertures for each set increase from right to left with decreasing surface density. The colors of the points indicate the amount of stellar mass formed, colored white when no SF has occurred yet. The sizes indicate the initial gas mass of the cloud, with the smallest being the M4 simulations and the largest being M6. The two labelled lines on the plot indicate the analytical conditions for free-fall and virial equilibrium (see the discussion of Fig. 2 in Ballesteros-Paredes et al., 2011). We include these lines for easier comparison to the observations presented by (Finn et al., 2019) rather than for inferring the state of the system. Unintuitively, velocity dispersions in a state of free-fall exceed those of virial equilibrium.

Though the Firecracker cloud is as massive as M6, its surface density is lower: more comparable to M5. This is why we see an overlap between M5 and the Firecracker cloud when M5 has formed $4 \times 10^4 M_{\odot}$ of stars, which is on the order of the stellar mass estimated to have already formed in the Firecracker cloud of $\leq 10^4 M_{\odot}$. This aligns with the idea that surface density is more influential than mass in the formation of star clusters. This also supports the possibility that the Firecracker gas velocities could be caused by the contribution of stellar feedback to the velocity dispersion in addition to free-fall collapse. The fast dynamical evolution of our models sug-

gests that these are not equilibrium objects, making it unnecessary to invoke a high-pressure background to keep the cloud from expanding. This suggests objects like the Firecracker cloud can form from collapse with observed velocity dispersions without invoking a high pressure background medium.

3.5.3 Other simulations

For massive star clusters to form, they must survive the epoch of gas dispersal and remain bound. An analytical model predicts a positive correlation of SFE to SFR and initial cloud mass (Zamora-Avilés and Vázquez-Semadeni, 2014). At high enough surface densities, stellar feedback cannot compete with star formation. Numerical studies done by Geyer and Burkert (2001) found that if the stars are initially in virial equilibrium with the remaining gas, only clusters with SFE $\geq 50\%$ remain bound against the outflow of the gas. Li et al. (2018) finds in their cosmological galaxy formation models that though galactic properties are unaffected by varying ϵ_* , the properties of star clusters are affected. In particular, they found that the initial bound fraction of stars increases with ϵ_* and cloud mass. Farias et al. (2023) ran cluster formation models from $2 \times 10^4 M_\odot$ clouds and finds that SFE and gas expulsion time correlate with global bound fraction, with all SFEs $\leq 20\%$ and all bound fractions $\leq 40\%$. Although it is still possible to form bound clusters with low SFE, these studies imply massive bound star clusters were most likely formed with high SFEs.

Menon et al. (2023) also finds high SFEs of $\sim 80\%$ for $10^6 M_\odot$ clouds with feedback in the form of radiation pressure solved using a variable Eddington tensor approach as opposed to our ray-tracing method. In this density regime, radiation pressure is the dominant feedback mechanism⁴. They conclude that radiation pressure simply cannot regulate star formation for clouds with surface densities $\Sigma \gtrsim 10^3 M_\odot \text{pc}^{-2}$.

Our results are more constraining: We included more feedback physics, and we still achieved SFEs of $\epsilon_* > 80\%$. Our M6 cloud is above this surface density with $\Sigma = 2.3 \times 10^3 M_\odot \text{pc}^{-2}$. They also tested a larger $10^6 M_\odot$ cloud with roughly the same surface density as our M5 cloud, and find an SFE of $\epsilon_* \approx 60\%$ comparable to the SFE of our M5 cluster of $\epsilon_* = 65\%$.

Other simulations of massive star cluster formation with initial cloud mass of $10^6 M_\odot$ find high SFEs of $\sim 65\%$ (Grudić et al., 2018b) and 38% (Kim et al., 2018) for surface densities of $\Sigma = 1.27 \times 10^4 M_\odot \text{pc}^{-2}$ and $\Sigma = 500 M_\odot \text{pc}^{-2}$, respectively. Kim et al. (2018) finds an even higher SFE of 51% for a $10^5 M_\odot$ cloud but with a surface density

⁴ See extended data Figure 5 of Howard et al. (2018) and Figure 12 of Krumholz et al. (2019).

of $\Sigma = 1.27 \times 10^3 \text{ M}_\odot \text{ pc}^{-2}$. Cluster models in Kimm et al. (2022) reached $\epsilon_\star = 50\text{--}72\%$ from an initial cloud of $1.4 \times 10^6 \text{ M}_\odot$ and $\Sigma = 647 \text{ M}_\odot \text{ pc}^{-2}$ despite SN and radiation feedback. Another cluster, modeled with radiation feedback by Fukushima and Yajima (2021), reached $\epsilon_\star = 78\%$ from a 10^6 M_\odot cloud with $\Sigma = 3.2 \times 10^3 \text{ M}_\odot \text{ pc}^{-2}$. This study also finds that bound cluster formation only occurs with $\epsilon_\star \geq 30\%$. Recent models of 10^6 M_\odot clouds with $R = 10 \text{ pc}$, $\alpha_v = 0.1$, and $Z = 0.2 Z_\odot$ reached $\epsilon_\star = 50\%$ (Fujii et al., 2024). The SFE in all of these studies increases strongly with surface density and slightly with initial cloud mass. Our results combined with those from previous models provide evidence that the formation of bound YMCs requires not only a high cloud mass but also, and more importantly, a high surface density.

Simulations of star clusters forming from clouds similar to our M5 cloud resulted in lower SFEs of 10–30%. The main difference between these models and ours is the use of sink particles to represent sub-clusters with combined feedback compared to our tracking of feedback from individual massive stars. A cloud modelled by He et al. (2019) with an initial mass of 10^5 M_\odot , peak number density $n = 1.8 \times 10^3 \text{ cm}^{-3}$, metallicity $Z = Z_\odot$, a higher virial parameter $\alpha_v = 0.4$, and stellar feedback only through UV radiation reached a SFE of 13.7% by $6 t_{\text{ff}}$. The cloud in Ali (2021) is the same mass and metallicity as M5, almost the same radius, $R_{\text{cloud}} = 11.9 \text{ pc}$, but is initially super-virial, with $\alpha_v = 1$. By $0.75 t_{\text{ff}}$, the SFE reached only 10% while M5 reached $\epsilon_\star = 20\%$ by this time. This difference may come from the different initial virial parameters, which prolongs the formation of the cluster in Ali, 2021. Another possible cause is different feedback models. Injecting stellar feedback from entire sub-clusters rather than individual stars could artificially strengthen the effect of feedback resulting in a lower SFE.

Fujii et al. (2021) presents star-by-star cluster models with feedback in the form of radiation, radiation pressure and stellar outflows. For an initial cloud of 10^5 M_\odot , $R = 20 \text{ pc}$, and $\alpha_v = 0.25$ they find $\epsilon_\star = 40\%$. The same cloud with a larger virial parameter of $\alpha_v = 1.0$ only reached $\epsilon_\star = 40\%$. Their sub-virial model agrees with our findings for M5. The super-virial model with a lower SFE further indicates that the high SFEs we find are possibly due to the low initial virial parameter, particularly for lower density clouds.

A colliding flow model of star formation in GMC environments described in Colín et al., 2013 with individual star formation and ionizing radiation found SFEs of $\epsilon_\star = 10\text{--}30\%$ depending on the degree of concentration by the flows. The two cylindrical streams were very large, with $r = 64 \text{ pc}$ and $\ell = 112 \text{ pc}$ and rarefied, with $n = 1 \text{ cm}^{-3}$, with the total mass in the two streams equalling $9 \times 10^5 \text{ M}_\odot$. The different initial conditions hinder a direct comparison to our SFE values,

but reaching high SFEs from low density flows aligns with our results for M4.

Simulations have broadly found star formation to be suppressed with each additional form of stellar feedback included in the model (see Dale, 2015). The exclusion of protostellar jets in our feedback model may artificially raise the SFR, as they contribute to the dispersal of gas around even low-mass stars at small scales (Chevance et al., 2023). Due to the quantity of low-mass stars and the collimated shape of the outflow, jets are drivers of turbulence at large scales in GMCs (e.g., Appel et al., 2022; Federrath, 2015; Nakamura and Li, 2007). These models do show that jets are an important factor in slowing the growth rate of the integrated SFE, though the final SFE is not known due to the duration of the simulations (Federrath, 2015). Guszejnov et al. (2021) performed simulations of star-by-star cluster formation from $2 \times 10^4 M_{\odot}$ clouds with stellar feedback, including protostellar jets as well as radiation, winds, and SNe. Simulations were repeated that isolated each form of feedback. They found jets to be important in regulating the growth of low-mass stars and constraining the IMF. Radiation and jets were the primary form of feedback that slowed star formation and dispersed the cloud. However, again the simulations were not run until the end of star formation, so the degree to which each effect changes the final SFE remains uncertain.

Despite their ubiquity, jets cannot prevent gas in high-density GMCs from forming stars eventually nor contain the power needed to disperse GMCs (see Chevance et al., 2023). The effect that jets would have on more massive clouds remains unclear. Although they may indeed slow star formation to observed values, as proposed by Chevance et al. (2023), analytic work by Matzner (2002) suggests that more massive clouds would be resistant to dispersal by jets, consistent with simulations by Guszejnov et al. (2022a).

In order to verify the physical plausibility of the high SFE in M6 despite the large number of formed stars, we have directly compared our 3D results to a followup calculation using the one-dimensional (1D) code Winds And Radiation Pressure: Feedback Induced Expansion, collapse and Dissolution (WARPFIELD; Rahner et al., 2019). This code models the effect of stellar feedback from young clusters on their natal gas cloud in spherical symmetry. WARPFIELD is designed to solve for the self-consistent motion of a 1D spherical gas shell evolving under the influence of feedback mechanisms including stellar winds, SNe, and radiation pressure, with consideration of gravity. We ran WARPFIELD using the same initial conditions as chosen for the M6 run (i.e., mass, density, temperature), with the addition that we varied the SFE from $\epsilon_{*} = 0.1$ – 0.9 in bins of 0.1 , as shown in Figure 10. This varies the strength of the stellar feedback to test whether the M6 cloud would still be stable given amount of stars formed.

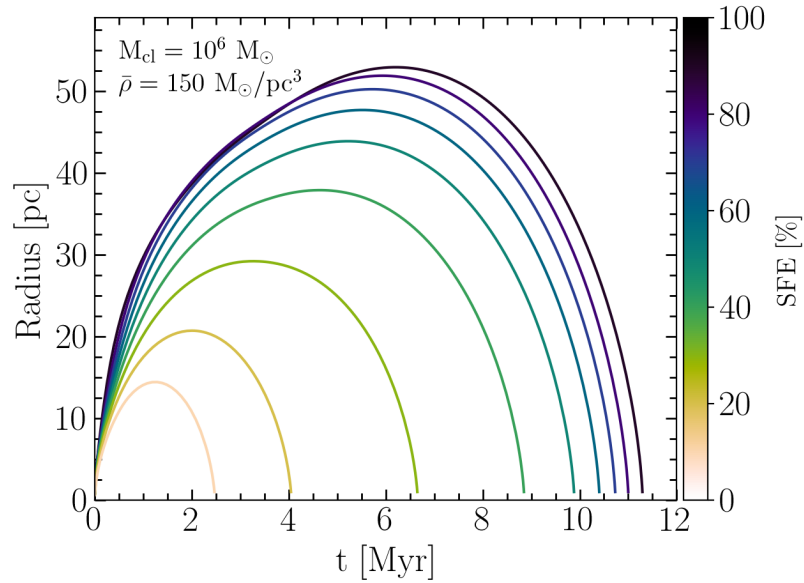


Figure 10: WARPFIELD evolution of shell radius versus time with different initial SFEs with the same parameters described in M6. In all cases, stellar feedback is inefficient in dispersing the surrounding dense cloud, and the shell eventually undergoes re-collapse.

For all SFE values, the shocked gas eventually re-collapses. At this high density, the included feedback is not strong enough to completely disperse the cloud. The SFE of our M6 cluster most closely resembles the WARPFIELD runs with $\epsilon_* = 80\%$ & 90% in Figure 10. The WARPFIELD model reaches a maximum radius of $R \sim 55$ pc at $t \sim 6.5$ Myr, and collapses back to $R = 0$ pc by $t \sim 11.25$ Myr. In the 1D model, all feedback occurs at a single point, so it is more effective than in our star-by-star 3D model, as in multiple dimensions channels that vent thermal energy can exist. Nevertheless, the gas still re-collapses, promoting further star formation. The expanding gas is not accelerated fast enough to escape the deep potential well of the massive cloud and the cluster that forms from it. This result supports the idea that the high SFE is due to the total feedback strength being weaker than gravity at these densities.

However, our results do suggest that more dispersed star formation leading to increased energy dissipation by radiative cooling may not even allow that much expansion. To resolve SFE well, feedback must be modelled for individual stars instead of for entire clusters. Approximating feedback as a sum for an entire cluster underestimates the SFE.

3.6 CONCLUSIONS

We performed numerical simulations of star cluster formation from gas clouds that run until star formation ceases or slows significantly due to stellar feedback dispersing any remaining gas. We tested initial cloud masses of 10^4 , 10^5 , and $10^6 M_\odot$ with radius $R = 11.7$ pc, holding all other characteristics of the initial cloud and simulation parameters the same. We analyzed the star formation histories and followed the evolution of the gas and forming star clusters. From this study, we conclude the following:

- Giant molecular clouds with surface density $\Sigma \geq 10^2 M_\odot \text{ pc}^{-2}$ and mass $M_{\text{cloud}} \geq 10^5 M_\odot$ can form fully bound star clusters with stellar mass $M_\star \geq 10^4 M_\odot$ with a high SFE $\epsilon_\star \geq 65\%$ over a short time $t_{\text{sf}} \approx 1 t_{\text{ff}}$, as seen by M5 and M6. The lower mass and density M4 cloud forms a cluster with a lower bound mass fraction of 60%.
- The Firecracker cloud in the Antennae galaxies, with a mass of $1\text{--}9 \times 10^6 M_\odot$ and a radius of 22 pc (Finn et al., 2019), is a close analog to our M6 cloud, though with a surface density more closely matching our M5 cloud. From our results we can estimate that the Firecracker cloud will convert 65–85% of its mass into stars within a free-fall time and that it will form a YMC.
- It has been suggested that the Firecracker cloud must be surrounded by a high pressure medium to contain it because of its high surface density and size-line width coefficient σ_v^2/R (Finn et al., 2019; Johnson et al., 2015). However, the M5 cluster reaches the same values by the time it forms $M_\star \approx 10^4 M_\odot$ worth of stars, the same amount of stellar mass estimated to have formed in the Firecracker cloud. This suggests another possibility: Rather than being an equilibrium object confined in a high pressure environment, the Firecracker cloud is actually dynamically collapsing and forming stars, and the high velocity dispersion of the gas is from the combination of free-fall collapse and stellar feedback.
- Star formation from GMCs is capable of achieving up to 85% efficiency at high densities. Our M6 cloud is the most efficient of our models, converting $\epsilon_\star = 85\%$ of its gas into stars. Even with hundreds of massive stars producing feedback, the short timescale of gravitational collapse for dense massive clouds renders the stellar feedback inefficient at slowing early star formation. However, even at much lower densities and masses, the M5 and M4 clouds achieved high SFEs of $\epsilon_\star = 65\%$ and 36%, respectively. In dense, massive clouds, the total dispersing force

of stellar feedback from winds and radiation cannot counteract the gravity from stars and gas until over half the cloud mass is converted into stars.

- The M4 cloud has a typical mass and size of Milky-Way GMCs. The SFE of M4 matches the maximum observed SFE values. This high SFE could be because of the low initial virial parameter of the cloud, or it could be due to the missing FUV radiation from stars $< 20 M_{\odot}$. Alternatively, the exclusion of the protostellar jet feedback mechanism may be important for clouds similar to M4 clouds, as suggested, for example, by Chevence et al. (2023). Further studies must be done to constrain the effect of varying the virial parameter and including protostellar jets on integrated SFE.
- Star formation is fast in our models of clouds with low α_v . Regardless of the initial mass or density, the majority of star formation occurs within the first global free-fall time of the collapsing GMC. Collapse occurs and stars are produced so rapidly that stellar feedback is only prevalent and strong enough to clear dense gas from the cluster’s deep potential well after most of the cloud has formed into stars. The speed of star formation may depend strongly on the initial virial parameter and the inclusion of jets.
- A 1D stellar feedback model `WARPFIELD` was run using the same mass and density as the M6 simulation. In it, the gas re-collapses even for SFEs up to 90%. Even centralized feedback cannot expel the gas from the potential well of the massive cluster that forms. The `WARPFIELD` results indicate that the expanding gas shell for $\epsilon_{*} = 85\%$ collapses back to $R = 0$ by 11 Myr.
- Including feedback for individual stars rather than adding the total energy for the cluster at a single point is important for correctly constraining star formation histories. Modelling individual stellar feedback spreads the feedback energy enough to greatly reduce its effectiveness at clearing the natal gas because of the resulting enhanced radiative cooling. Models that add stellar feedback for the entire star cluster at a single point appear to overestimate the effect of the feedback on the gas and the star formation timescale and to underestimate the final SFE.

In conclusion, bound massive star clusters such as YMCs and GCs readily form from high-mass, dense GMCs. The GMCs can become this dense and massive naturally, even in the present day, as shown by the Firecracker cloud in the Antennae galaxies. In the early Universe, where galaxies were much more gravitationally unstable, these conditions would be much more common. The subsequent star formation from these dense high-mass clouds is highly efficient, converting

$\geq 40\%$ of the gas mass into stars within the first free-fall time of the initial cloud. The short timescales of star formation and/or the deep gravitational potential wells of dense, massive clouds render stellar feedback unable to significantly slow star formation, leading to integrated efficiencies as high as 85% for more massive clouds. After their formation, the clusters born in these environments remain bound after 90% of the gas is expelled.

Until recently, directly observing proto-GCs has been elusive. Now with JWST, observers have discovered five bound stellar clumps just 460 Myr after the Big Bang at $z \sim 10.2_{-0.2}^{+0.2}$ (Adamo et al., 2024). These clusters in the strongly lensed galaxy SPT0615-JD1 (alias the Cosmic Gems arc) have intrinsic masses of $\sim 10^6 M_{\odot}$, half-light radii of $R_{\text{eff}} \sim 1$ pc, and ages between 9 and 35 Myr. Roughly $\sim 60\%$ of the total F150W flux of the galaxy comes from these five clusters, indicating that the predominant mode of star formation in these systems occurs in massive clusters. The resemblance between M6 and these objects is notable, indicating that the mode of star formation described in this study is a probable path for the formation of YMCs and proto-GCs in the present and early Universe, respectively.

3.7 ACKNOWLEDGEMENTS

B.P. would like to thank Gastón Escobar and Michela Mapelli for the helpful discussions that led to solving a persistent bug allowing continuation of the simulations. B.P. thanks Shyam Menon for many fruitful discussions of YMC formation, particularly regarding the battle between stellar feedback and gravity. We thank the referee for their useful comments and insights. B.P. was partly supported by a fellowship from the International Max Planck Research School for Astronomy and Cosmic Physics at the University of Heidelberg (IMPRS-HD). M.-M.M.L., B.P., E.P.A., and A.T. were partly supported by NSF grants AST18-15461 and AST23-07950. C.C.-C. is supported by a Canada Graduate Scholarship - Doctoral (CGS D) from the Natural Sciences and Engineering Research Council of Canada (NSERC). This work used Stampede 2 at TACC through allocation PHY220160 from the Advanced Cyberinfrastructure Coordination Ecosystem: Services & Support (ACCESS) program, which is supported by National Science Foundation grants 21-38259, 21-38286, 21-38307, 21-37603, and 21-38296. The code development that facilitated this study was done on Snellius through the Dutch National Supercomputing Center SURF grants 15220 and 2023/ENW/01498863. S.A. acknowledges the support of NSF grant AST-2009679. M.W. acknowledges the support of NOVA project 10.2.5.12.

R.S.K. and S.C.O.G. acknowledge financial support from the European Research Council via the ERC Synergy Grant “ECOGAL” (project ID 855130), from the Heidelberg Cluster of Excellence (EXC 2181 -

390900948) “STRUCTURES”, funded by the German Excellence Strategy, and from the German Ministry for Economic Affairs and Climate Action in project “MAINN” (funding ID 50002206). The team in Heidelberg also thanks *The Länd* and the German Science Foundation (DFG) for computing resources provided in bwHPC supported by grant INST 35/1134-1 FUGG and for data storage at SDS@hd supported by grant INST 35/1314-1 FUGG.

L.W. thanks the National Natural Science Foundation of China for support through grants 21BAA00619, 12073090 and 12233013, and the one-hundred-talent project of Sun Yat-sen University, the Fundamental Research Funds for the Central Universities, Sun Yat-sen University (22hytd09).

The authors acknowledge Interstellar Institute’s program “II6” and the Paris-Saclay University’s Institut Pascal for hosting discussions that nourished the development of the ideas behind this work.

3.8 DATA AVAILABILITY

Simulation data and the interactive plot file is available for download at <https://doi.org/10.5531/sd.astro.8>.

3.9 APPENDIX

3.9.1 *Stellar properties: Physical times*

Figure 11 reproduces Figure 8 using physical time rather than free-fall times to show global stellar properties over time. This demonstrates how much the duration of star formation shortens while its intensity increases as the cloud mass increases.

3.9.2 *Stellar modifications*

3.9.2.1 *Low-mass star agglomeration*

Upwards of 10^6 stars can be expected to form from a $10^6 M_{\odot}$ cloud with a peak number density of $n \approx 1000 \text{ cm}^{-3}$. Even with the best modern N-body codes, evolving this many single stars and higher order stellar systems in such a dense stellar environment with a gravity bridge from each star to the gas in a separate code is immensely computationally taxing. To reduce the strain on the N-body portion of the calculations, we chose to agglomerate all stars under a given mass into gravitational super-star particles of equivalent mass to their sum. We refer to this mass cutoff as the agglomerate mass.

When a sink progresses through the list of stellar masses it will form, stars with masses under M_{agg} are put aside until the sum of their masses is above M_{agg} . Then a star particle is formed with the

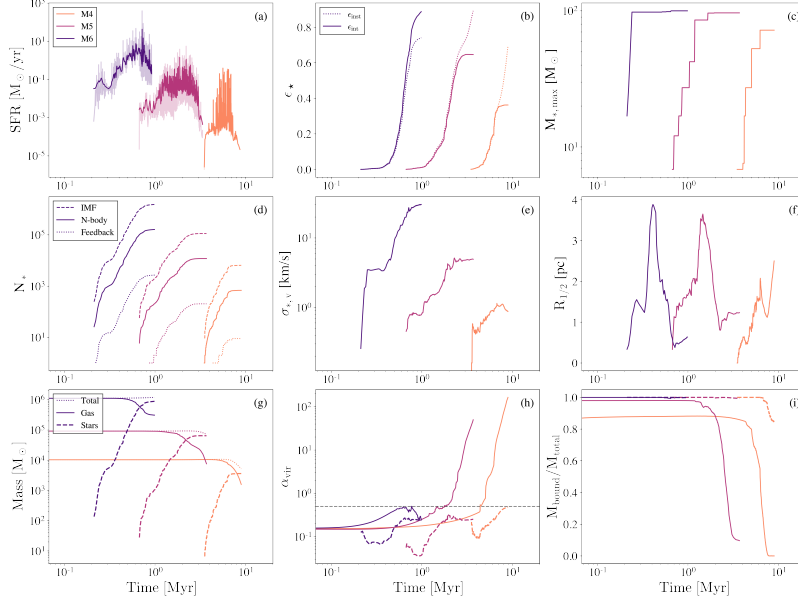


Figure 11: Global properties of the clusters and gas over time for models M4 (orange), M5 (maroon), and M6 (blue-violet) for comparison to Figure 8, where units of free-fall time (see Table 3) are used. From top left to bottom right: (a) SFR, where the transparent lines show the SFR at each star formation event, and the solid lines give the SFR smoothed using a Gaussian filter with $\sigma = 0.005t_{\text{ff}}$. (b) Instantaneous and integrated SFES of the clouds, where $\epsilon_{\text{inst}} = M_{\star}/(M_{\text{gas}} + M_{\text{sink}} + M_{\star})$ and $\epsilon_{\text{int}} = M_{\star}/M_{\text{cloud}} = \epsilon_{\star}$. (c) Most massive star formed. (d) Number of formed stars. *Dashed line:* actual number of stars that would form from sampling the IMF given the amount of gas mass collected for star formation by sink particles. *Solid line:* number of stars followed in TORCH after the sampled stellar population below $4 M_{\odot}$ has been agglomerated. *Dotted line:* number of stars above $20 M_{\odot}$ on the grid that are generating feedback. The number of stars can drop due to SNe, mass loss, or exiting the grid. (e) 3D stellar velocity dispersion. (f) Half-mass radius of the entire star cluster. (g) Total mass (*dotted line*), mass of stars (*dashed line*) and gas (*solid line*) on the grid. (h) Virial parameter of stars (*dashed line*) and gas (*solid line*), where $\alpha_{\text{v}} = 0.5$ is the equilibrium value. (i) Fraction of mass bound for stars (*dotted line*) and gas (*solid line*).

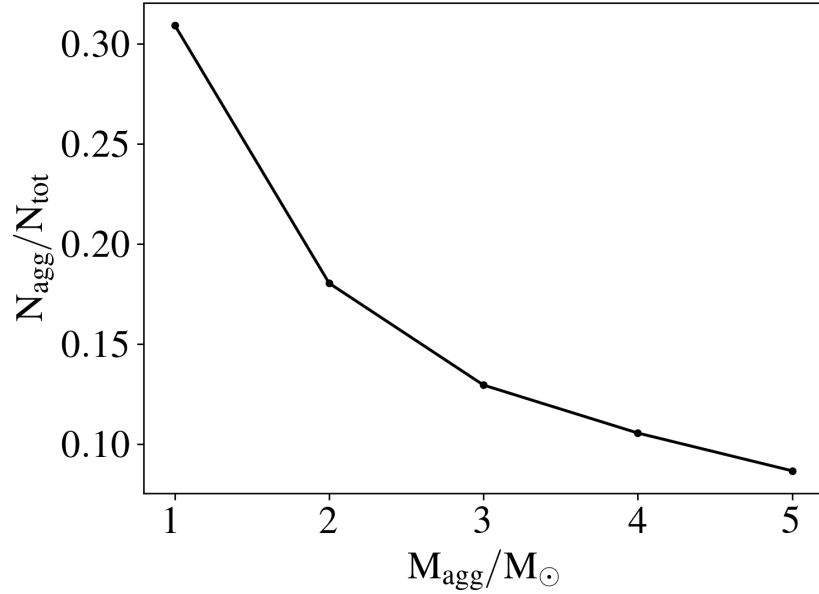


Figure 12: Fraction of the number of stars formed with agglomeration of stars below the mass on the x-axis over the total number of stars sampled by the IMF. We used $M_{\text{agg}} = 4 M_{\odot}$, which means the number of stars in the grid is 10% of the number that are formed by our IMF.

summed mass. Figure 12 shows the reduction in number of stars formed in a cloud for a given agglomerate mass. For our choice of $4 M_{\odot}$, we only had 10% of the stars undergoing gravitational interactions compared to the case with no agglomeration. This reduced our N-body execution time by a factor of somewhere between the $10 \log 10$ expected for the tree and 10^3 expected for the direct N portion of the PETAR algorithm. We note that the feedback from these low-mass stars is shown in Appendix 3.9.2.2 to be negligible compared to that of the higher-mass stars, and in any case the current TORCH version does not model feedback from stars $< 8 M_{\odot}$ as we neglect jets, while the ionizing radiation from such low-mass stars is negligible. In this study, we further limited feedback to only come from stars $\geq 20 M_{\odot}$ as we discuss in the next subsection. The primary missing contribution from low-mass stars physically is their mutual gravitational interactions, which could potentially lead to the ejection of some fraction of them. However, the dynamics driven by those low-mass stars is also expected to be negligible in comparison to the effect of gas and more massive stars in the cluster. TORCH simulations with no mass agglomeration were done by Cournoyer-Cloutier et al. (2023), and in analyzing the morphology of clusters they find that the gravitational effects of the gas dominate over any stellar dynamics effect for the overall evolution of the cluster while it remains embedded.

3.9.2.2 Feedback mass limit

We limited all forms of stellar feedback—winds, radiation, and SNe—to stars above $20 M_{\odot}$ instead of the value of $8 M_{\odot}$ (lower bound for SN explosions) usually adopted in TORCH. This is necessary to significantly reduce the number of rays on the grid, which greatly decreases the calculation time and memory overhead for the ray-tracing algorithm. We quantify the effects of excluding radiation and winds from stars with masses below $20 M_{\odot}$ by comparing the power output in the form of winds and radiation from all stars above $8 M_{\odot}$ and above $20 M_{\odot}$. We only allowed stars above $20 M_{\odot}$ to explode as SNe. Our simulations ran for ≤ 10 Myr, which is roughly the main-sequence lifetime of a $20 M_{\odot}$ star. Stars under $20 M_{\odot}$ do not explode as SNe in the timeframe of our simulations, so excluding their SNe feedback makes no practical difference for this comparison.

The power as a function of mass in the form of EUV radiation, non-ionizing FUV radiation, and stellar wind is shown in Figure 13. We calculate these powers by taking stars from 8 to $100 M_{\odot}$ in $1 M_{\odot}$ increments, evolving them in SEBA for 1 Myr, and summing the energy output of each feedback channel. From this figure we can see that the power output of stellar winds and UV radiation is several orders of magnitude higher for stars above $20 M_{\odot}$ than for stars closer to $8 M_{\odot}$. Although stars in the 8 – $20 M_{\odot}$ mass range still output a considerable amount of FUV radiation, stars above $20 M_{\odot}$ account for over 80% of the total radiation power.

Although the feedback power is much stronger for stars above $20 M_{\odot}$, stars with masses 8 – $20 M_{\odot}$ greatly outnumber them. To find the ratio of feedback power for stars below and above $20 M_{\odot}$, we convolve the number of stars of each mass with the power output for each stellar mass (Fig. 14). In the top left histogram, we show the ratio of stars with mass 8 – $20 M_{\odot}$ to stars with mass 20 – $100 M_{\odot}$ in all three simulations, sampled at their respective initial free-fall times. All three runs have more stars in the lower-mass bin. In the top right plot, we show the ratio of total stellar feedback power P_{FB} (excluding SNe) for the stars in the two mass bins considered. We can see that although the lower-mass stars outnumber the higher-mass stars, the higher-mass stars still account for $> 80\%$ of the total stellar feedback energy. This shows that only including feedback from stars above $20 M_{\odot}$ still retains almost all of the feedback energy produced after the formation of all three star clusters.

The bottom panel in Figure 14 shows the feedback power per mass bin for each separate feedback process. For the EUV radiation and wind feedback, the low-mass stars contribute practically nothing to the feedback energy in comparison to the high-mass stars. The FUV feedback of low-mass stars is not negligible, but is still well below 20% of the total FUV feedback energy from all stars.

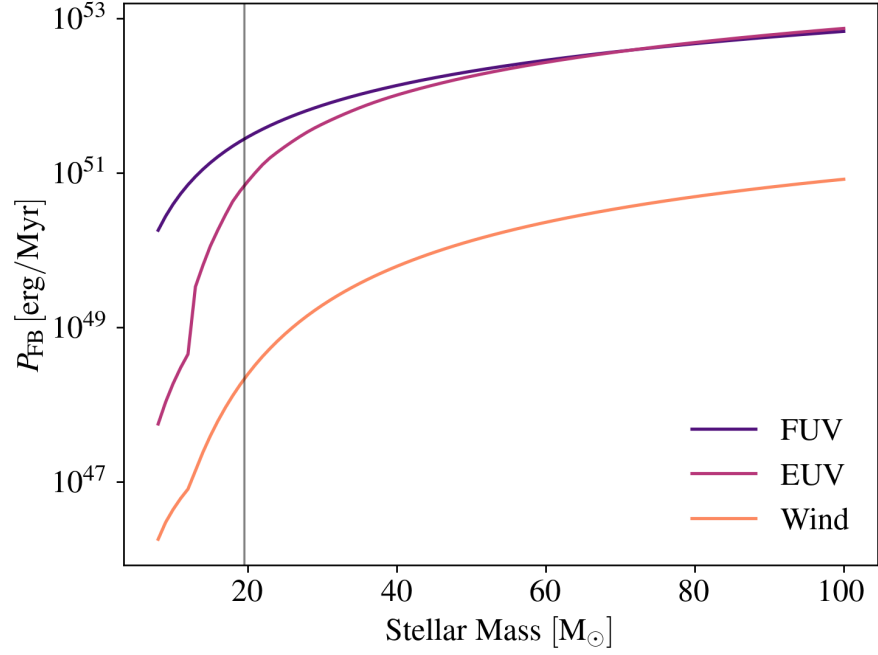


Figure 13: Power of stellar feedback in the form of winds and FUV and EUV radiation for different stellar masses. Left of the vertical line shows the amount of feedback power lost per star by excluding feedback from stars below $20 M_{\odot}$.

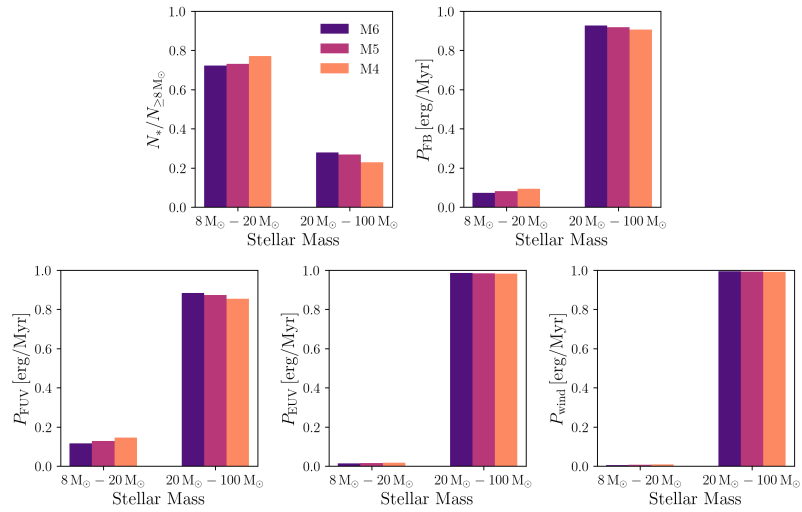


Figure 14: Power output of stellar feedback modes for each stellar mass regime. (*Top left*): Histogram showing the fractional stellar population of the three runs at one free-fall time, split into the mass regimes of $8\text{--}20$ and $20\text{--}100 M_{\odot}$. (*Top right*): Fraction of feedback power in each mass regime. (*Bottom*): Histograms showing the fraction of feedback power for FUV, EUV, and winds in each mass regime. Although there are more lower-mass stars, the feedback produced by them is less than 20% of the total feedback energy for all stars.

3.9.2.3 Mass-loading stellar winds

In TORCH, the stellar wind feedback implementation is inspired by Simpson et al. (2015), using a method of momentum injection, the details of which can be found in Wall et al. (2020). The energy of the cells within the wind injection radius of the star is increased based on the mechanical luminosity of the wind $L_w = (1/2)\dot{M}v_w^2$, where \dot{M} is the stellar mass loss rate (Vink et al., 2000) and v_w is the terminal wind velocity (Kudritzki and Puls, 2000). The wind injection radius is set by comparing the cell width Δx to the wind termination shock radius (Weaver et al., 1977)

$$R_w = 0.74 \left(\frac{\dot{M}}{\rho_0} \right)^{3/10} v_w^{1/10} t_w^{2/5}, \quad (51)$$

where ρ_0 is the background density and t_w is the age of the wind-blowing star at the given time step. If $R_w < \Delta x$ the injection radius is set to Δx , otherwise it is set to a maximum value of $6\sqrt{3}\Delta x$, at which we have found that spherical winds are well resolved. Momentum and energy are conserved when injecting stellar winds.

Within a stellar wind bubble, in dense clumpy regions of star formation such as the ones in our simulations, material will be swept up into the flow of the hot bubble by mass loading processes such as photoevaporation and hydrodynamic ablation (Dyson and Hartquist, 1992; Hartquist and Dyson, 1996; Lancaster et al., 2021; Pittard et al., 2001). With enough mass loading, the density increase will result in much more efficient cooling and create momentum-driven rather than energy-driven bubbles. The amount of mass-loading in the case of hydrodynamic ablation depends on the prevalence of dense clumps within the wind region as well as the Mach number M of the flow around the clump. With a supersonic flow, the mass-loading rate saturates. With a subsonic flow, the mass-loading rate is proportional to $M^{4/3}$ (Hartquist et al., 1986; Smith et al., 1984). Accounting for mass loading in stellar wind models has been shown to successfully reproduce the kinematic properties of the observed stellar wind bubble of the Wolf-Rayet star RCW 58 (Arthur, 2007; Arthur et al., 1993, 1996).

Simply injecting winds at v_w does not account for these mass-loading processes and results in unphysically hot bubbles. Therefore, we chose a lower temperature target for our bubbles and lowered the wind velocity v_w such that the final temperature of the wind bubble is the correct one. We conserved momentum and energy when injecting stellar winds, so while lowering the wind velocity, we also infused correspondingly more mass into the bubble than the stellar mass loss calculated. This mass is not taken off the grid elsewhere, meaning mass was not entirely conserved. At $1.25 t_{ff}$, the total amount of mass that has been injected due to mass-loading as a fraction of initial cloud mass is 0.04, 0.02, and 0.01 for M4, M5, and M6.

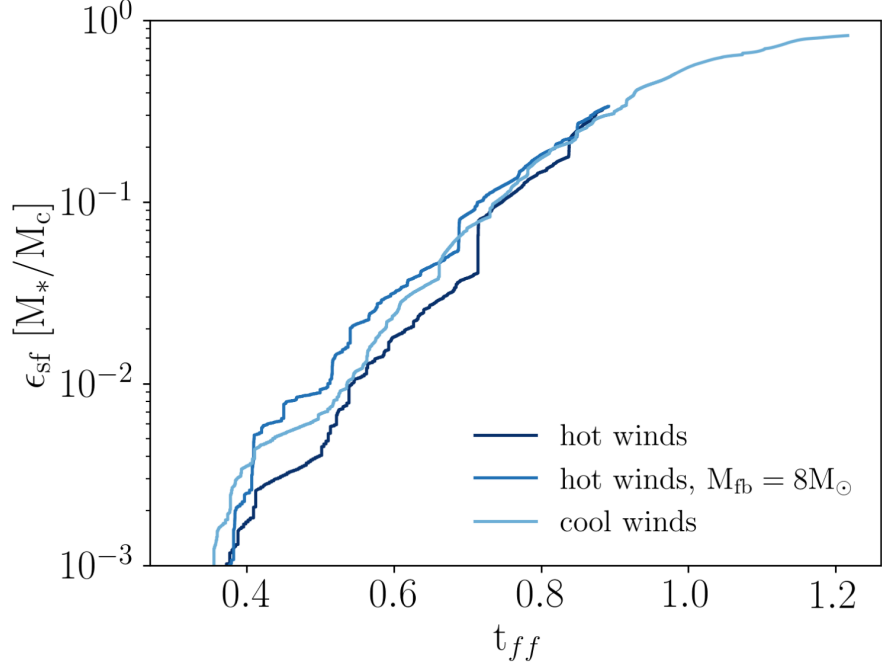


Figure 15: Star formation efficiency over time for the fiducial M6 cloud with $T_w = 300,000$ K and $M_{\text{feedback}} \geq 20 M_\odot$ (*cool winds*), the M6 cloud with $T_w = 5,000,000$ K and $M_{\text{feedback}} \geq 20 M_\odot$ (*hot winds*), and the M6 cloud with $T_w = 5,000,000$ K and $M_{\text{feedback}} \geq 8 M_\odot$ (*hot winds, $M_{\text{fb}} = 8 M_\odot$*).

Observed circumstellar bubbles cooled by suspected mass loading have been seen with temperatures as low as $T_b \approx 1.1 \times 10^6$ K in the S308 bubble (Chu et al., 2003). The spectra of the NGC 6888 bubble indicates a dominant component almost as cool, with $T_b = 1.5 \times 10^6$ K (Bochkarev, 1988; Wrigge, 1999; Wrigge et al., 1994).

In the simulations presented here, we heavily mass loaded the stellar winds to achieve a lower than observed bubble temperature of $T_b = 3 \times 10^5$ K. This temperature is at the peak of the cooling curve, so the shocked wind rapidly cools, resulting in smaller, cooler, momentum-driven bubbles instead of hot bubbles filled with 10^6 K gas. We chose to do so because the high sound speeds in hot wind bubbles lower the Courant time step significantly, making the computation impractical. Since we do not follow X-rays through ray-tracing, having cooler bubbles is adequate. Bubbles at this temperature also do not affect the ionization of the surrounding gas. The primary action of wind feedback during cluster formation is to clear out dense regions of gas so that radiatively ionized H II regions can expand. The only hot gas ($\geq 10^6$ K) on the grid comes from SNe. Capping the temperature of gas on the grid at 3×10^5 K until SNe occur significantly speeds up the simulations.

3.9.2.4 *Effect on star formation efficiency*

Limiting the temperature of stellar winds and only modelling feedback for stars above $20 M_{\odot}$ could potentially lead to un-physical runaway star formation. To test this, we re-ran the M6 model at early times to see if these two approximations are the cause for the extremely high SFE of 85%. For the first new M6 run we raised the wind temperature from 3×10^5 K to 5×10^6 K. For the second test, we both raised the wind temperature and modelled feedback for all stars above $8 M_{\odot}$. The SFE over time for the fiducial M6 run with our standard approximations and the new M6 models are shown in Figure 15.

The two runs without the approximations that reduce the strength of the stellar feedback have similar SFEs as the M6 model with the aforementioned approximations. This validates our approximations and supports our argument that the high SFE in model M6 is not an artifact of under-estimating the strength of stellar feedback.

RUNAWAY STARS AS FOSSILS OF SUB-CLUSTER MERGERS

4.1 ABSTRACT

Two main mechanisms have classically been proposed for the formation of runaway stars. The binary supernova scenario (BSS) suggests that a massive star in a binary explodes as a supernova, ejecting its companion. The dynamical ejection scenario suggests that a star is ejected through a strong dynamical encounter between multiple stars. We propose a third mechanism for the formation of runaway stars: the sub-cluster ejection scenario (SCES), where a subset of stars from an infalling sub-cluster is ejected out of the cluster by a tidal interaction with the contracting gravitational potential of the assembling cluster. We demonstrate the SCES in a star-by-star simulation of the formation of a young massive cluster from a $10^6 M_{\odot}$ gas cloud using the TORCH framework. This star cluster forms hierarchically through a sequence of sub-cluster mergers, determined by the initial turbulent, spherical initial conditions of the gas. We find that these mergers drive the formation of runaway stars in our model. Late-forming sub-clusters fall into the central potential, where they are tidally disrupted, forming tidal tails of runaway stars that are distributed highly anisotropically. Runaways formed by the same SCES share similar ages, velocities, and ejection directions. Surveying observations, we identify several SCES candidate groups with anisotropic ejection directions. The SCES is capable of producing runaway binaries: two wide dynamical binaries in infalling sub-clusters were tightened through ejection. This allows for another velocity kick via subsequent BSS. An SCES-BSS ejection is a possible avenue for producing hypervelocity stars unbound to the Galaxy. The SCES occurs when sub-cluster formation is resolved. We expect non-spherical initial gas distributions to increase runaway star numbers to observed values. The observation of groups of runaway stars formed via SCES thus reveals the assembly history of their natal clusters.

4.2 INTRODUCTION

Young stars displaced from their birthplace in the star-forming spiral arms of the Galaxy and moving away from the Galactic disk were first observed by Blaauw and Morgan (1954). Since then many more stars moving rapidly away from their formation sites have been observed throughout the Galaxy. These stars are typically classified as

runaways when their velocity relative to their associated nebula or cluster is $\geq 30 \text{ km s}^{-1}$ (Gies and Bolton, 1986).

Despite their ubiquity, the ejection mechanism remains unknown for most runaway stars. Currently, there are two popular proposed mechanisms for producing runaway stars: the binary supernova scenario (BSS, sometimes referred to as Blaauw kicks; Blaauw, 1961) and the dynamical ejection scenario (DES; Fujii and Portegies Zwart, 2011; Hoogerwerf et al., 2000; Poveda et al., 1967). The BSS suggests that when two massive stars are in a binary system and one explodes as a supernova, loss of the ejecta from the system reduces the gravity on the companion, which begins moving through space at a velocity comparable to its orbital velocity. The DES suggests that runaway stars are ejected by a strong dynamical encounter involving at least one binary, where orbital binding energy is converted to kinetic energy. In some cases, a runaway system is formed moving in the opposite direction of the system that ejected it (in the center of mass frame of the encounter) (Fujii and Portegies Zwart, 2011; Poveda et al., 1967). BSS and DES runaways can be distinguished by their rotational and linear velocities: the BSS produces slow-moving, rapidly rotating stars while the DES produces fast-moving, slowly rotating stars (Sana et al., 2022).

In this work, we propose a third mechanism for producing runaway stars: the sub-cluster ejection scenario (SCES) in which part of a sub-cluster is ejected from the cluster after it is tidally disrupted by the contracting potential of the assembling cluster. Star clusters form hierarchically, with giant molecular clouds (GMCs) fragmenting into dense clumps that form sub-clusters of stars. These sub-clusters merge, forming a single central cluster. The combined feedback eventually blows away the unused gas, leaving a gas-free star cluster (see e.g. Cournoyer-Cloutier et al., 2021, 2023; Grudić et al., 2018a; Lewis et al., 2023; Rahner et al., 2017, 2019; Wall et al., 2020, 2019; Wilhelm et al., 2023). To thoroughly investigate the origin of SCES runaway stars, the entire complex dynamical history of young star clusters must be modeled consistently. This necessitates modeling the entire star cluster formation process, following the birth of stars within sub-clusters.

We present a star-by-star simulation of cluster formation performed with the TORCH framework (Wall et al., 2020, 2019). TORCH follows gas dynamics, the N-body dynamics of stars, sub-grid star formation via sink particles, stellar evolution, and stellar feedback in the form of winds, radiation, and supernovae. With this simulation, we can determine the origin of runaway stars formed self-consistently in the cluster environment.

In this paper, we analyze the runaway stars formed in the M6 star cluster presented in Section 3.3, which forms from a molecular cloud with initial mass of $M_{\text{cloud}} = 10^6 M_{\odot}$ and initial radius of $R_{\text{cloud}} = 11.7 \text{ pc}$. In Sect. 4.3 we present the properties of the run-

away stars formed in M6, as well as, our evidence for the new SCES mechanism for producing runaway stars. We discuss the implications of our results in Sect. 4.4, and present some observational candidates for runaways formed via the SCES. We conclude in Sect. 4.5.

4.3 RESULTS

In our analysis, we make an initial selection for runaway stars by filtering for unbound stars,¹ with $E_{\text{total},i} = E_{k,i} + U_{*,ij} + U_{\text{gas}} > 0$ where $E_{k,i}$ is the kinetic energy, $U_{*,ij}$ is the gravitational potential of other star particles, and U_{gas} is the gravitational potential of the gas. Our analysis only covers the early runaways ejected during the hierarchical assembly of the cluster. The free-fall time of the M6 cloud is $t_{\text{ff}} = 0.67$ Myr, and the final simulation time is $1.36t_{\text{ff}} = 0.91$ Myr. The cluster is fully assembled by the end of the simulation, and SCES only occurs during active sub-cluster formation. This run time is therefore sufficient for analysis of the SCES. At the final time, the fraction of runaway stars is 0.51%. We cannot yet determine the final runaway star fraction due to the short run time of the simulation. Simulating the total runaway fraction requires integration times of $\gtrsim 2$ Myr, which is outside the scope of this paper introducing a production mechanism for early-forming runaway stars in young clusters.

Figure 16 shows a histogram of the runaway star count binned by the angular direction of the runaway velocities in the center-of-mass frame. There are two distinct groupings of runaway stars ejected in the same directions, and the overall directional distribution of runaways is highly anisotropic. This is caused by the tidal disruption of two infalling sub-clusters by the cluster center of mass, which then form two groups of runaway stars as tidal tails. White boxes in Figure 16 indicate the selection regions used to investigate the origin of these two groups of runaways. These regions were chosen by eye with the intent of performing a broad initial analysis.

We inspect the properties of the runaway stars in Figure 17 which shows a Mollweide spherical projection of the runaway stars colored according to radial velocity from the center-of-mass, mass, and age. The group 2 population is moving faster than group 1. The average velocity and standard deviation for group 1 and 2 are $\bar{v}_1 = 38.6 \text{ km s}^{-1}$, $\sigma_1 = 8.2 \text{ km s}^{-1}$, $\bar{v}_2 = 87.1 \text{ km s}^{-1}$, $\sigma_2 = 20.7 \text{ km s}^{-1}$. Both groups are composed mostly of low-mass stars with a few high-mass stars scattered within. The stars in a given group were formed at similar ages.

¹ Canonically, runaway stars are defined as stars leaving their birthplace at velocities $\geq 30 \text{ km s}^{-1}$. Unbound stars with lower velocities are typically referred to as walkaways. All unbound stars we consider in this work have velocities $\geq 30 \text{ km s}^{-1}$ criterion.

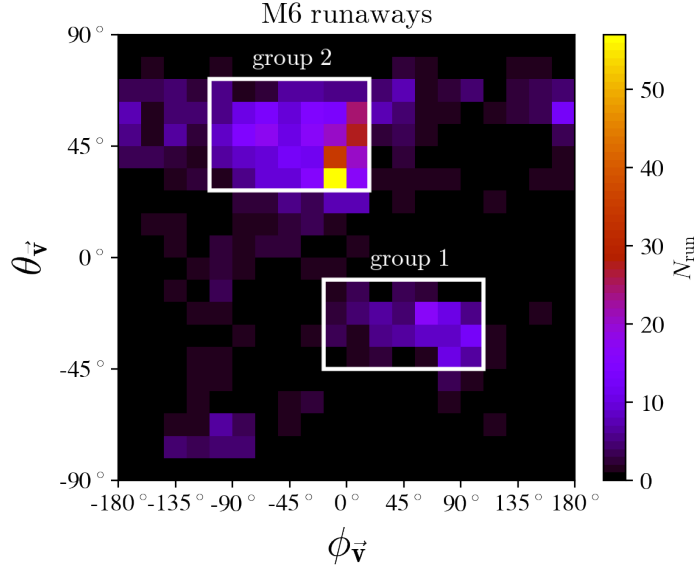


Figure 16: Ejection velocity angular directions of M6 runaways stars with $\theta_{\vec{v}}$ and $\phi_{\vec{v}}$ binned in 9° and 18° angle bins, respectively. There are two distinctly peaked angular regions which are labeled as group 1 and group 2. The rectangles indicate the angular bins of runaways we selected for trajectory analysis.

Figure 18 shows the age and velocity of the runaways in a scatter plot colored according to stellar mass, with the selected angle bins in Figure 16 marked by symbol type. The runaways are distinctly clustered in both radial velocity and stellar age. Group 1 is distinguished from the rest of the runaways in the upper left; stars in group 1 are older and have lower velocities ($v_r \approx 30 \text{ km s}^{-1}$). Group 2, however, consists of two populations of runaways seen as an age gap in the diamond points in Figure 18. This indicates stars from two sub-clusters or two generations of stars within one sub-cluster were ejected in the same direction. The mass distributions of both groups are the same, though, with both mostly containing low mass stars and a few stars above $10 M_\odot$. Figure 19 shows the Kroupa IMF power-law with $\alpha = -2.3$ and the histograms of the stellar masses in each runaway group as well as the entire cluster. The overpopulation of low mass bins ($< 8 M_\odot$) is a result of the mass agglomeration of stars below $< 4 M_\odot$. This suggests that each group consists of a random sampling of the IMF, which makes sense for a sub-cluster. Both runaway groups roughly resemble the IMF, indicating a lack of bias in which star masses in a merging sub-cluster are ejected from the cluster. We expect this is because the stars in the sub-cluster closest to the potential are tidally captured while the outer stars are ejected, and the spatial distribution of stellar masses within a sub-cluster is random by construction. Most of the runaway stars are agglomerated, which is expected from a sampling of the broader stellar population. This

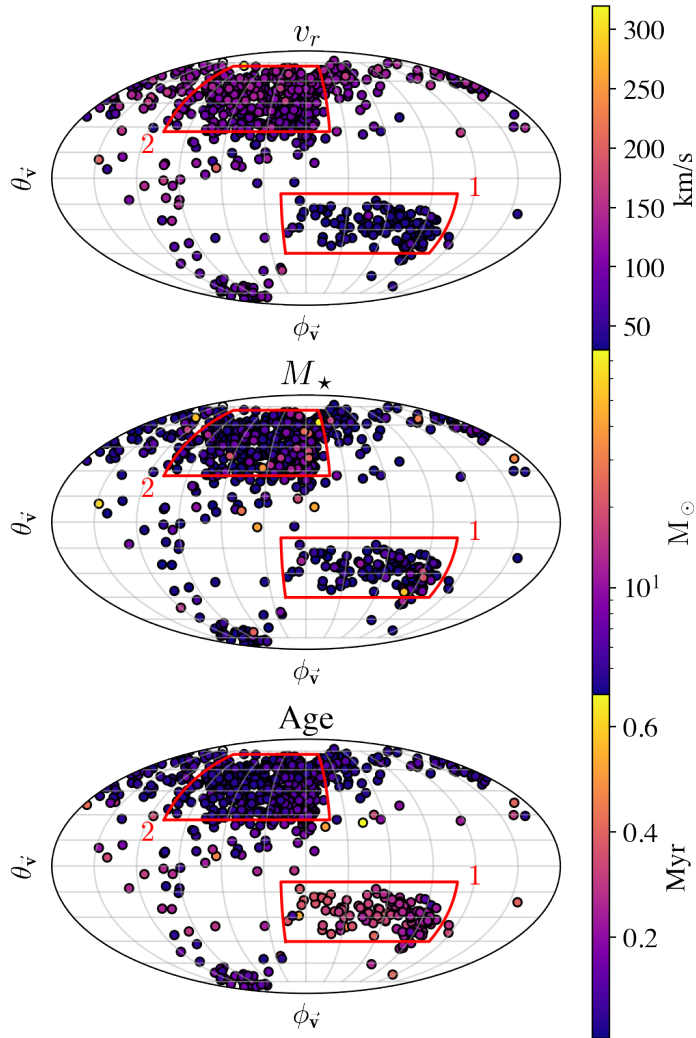


Figure 17: Mollweide map projection of the ejection directions of the runaway stars in M6. The colors correspond to (*top*) radial velocity from the cluster center of mass, (*middle*) star mass, and (*bottom*) star age. The highest values are plotted over lower values for visibility.

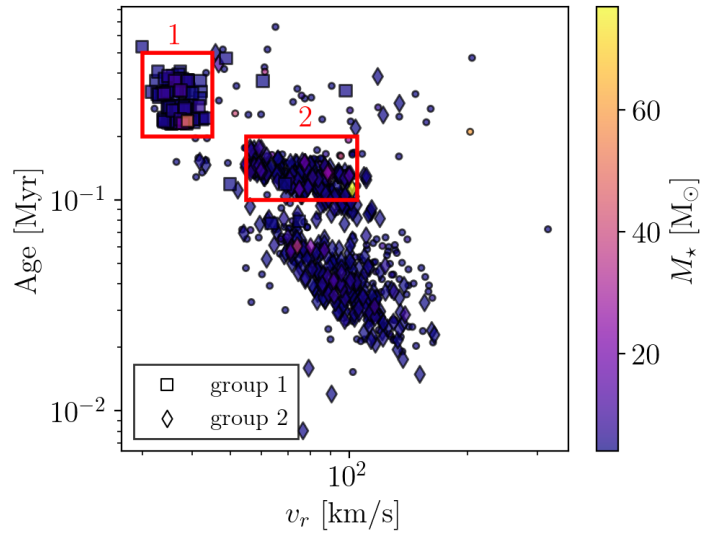


Figure 18: Scatter plot of the runaway stars, showing the radial velocity and age colored by mass. Squares are group 1, diamonds are group 2, and dots are the rest of the runaways. These groups are the runaways selected by ejection direction only. The two groups are distinctly separate in both age and velocity. Group 2 contains two sub-groups ejected in the same direction but at slightly different times. For the purpose of demonstrating the SCES mechanism, we focus on the later forming sub-group in group 2. The red rectangles indicate the additional filtering of the runaway groups by age and velocity.

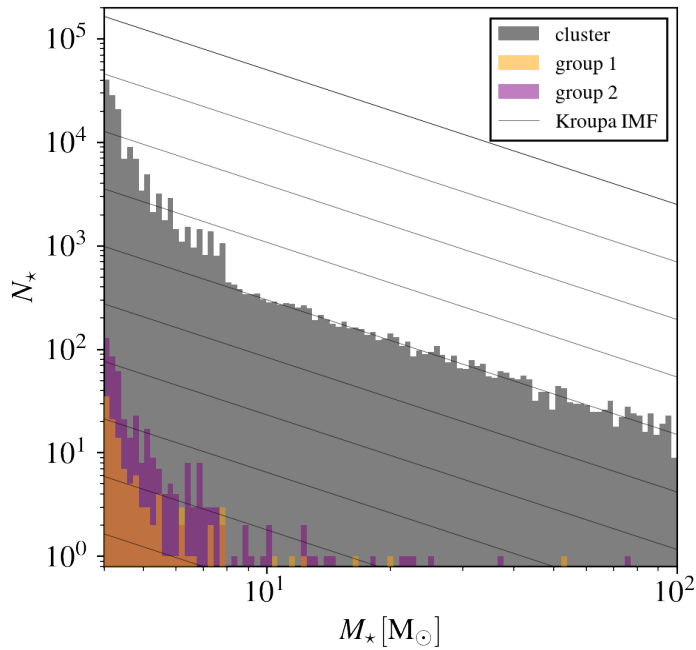


Figure 19: Particle mass distributions of the entire star cluster (*grey*) and the runaway groups along with the Kroupa IMF power-law. Note that at the low-mass ($\leq 8M_{\odot}$) end, the particle masses are skewed higher than the sampled IMF due to the agglomeration of stars below $< 4M_{\odot}$.

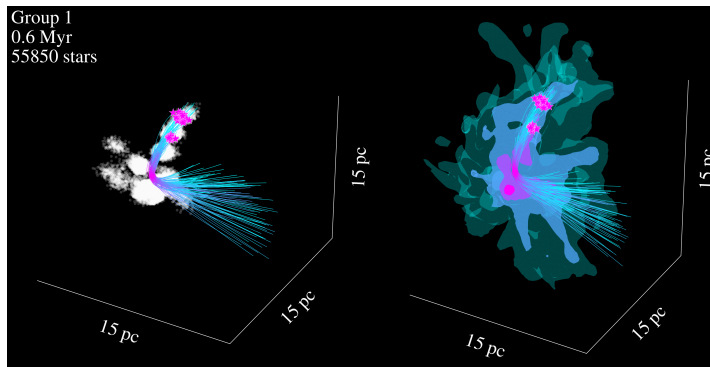


Figure 20: (Movie online) Movie of the formation and ejection of runaway star group 1. The left plot shows the stars as they are forming in the cluster, and the right plot shows the gravitational potential of both the stars and gas. The trajectories of the runaway stars are shown as lines. Once each runaway star forms, it appears with a star marker. This plot shows the same variables as shown in Figures 21 and 22.

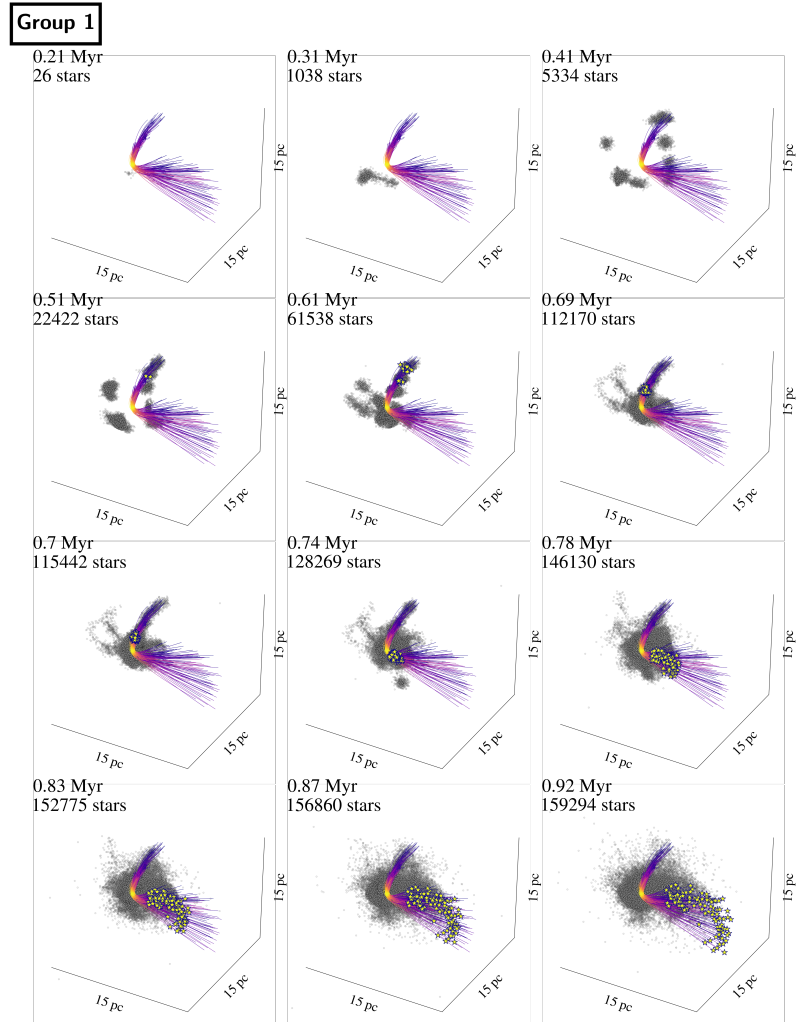


Figure 21: Trajectories of runaway star group 1 originating from a sub-cluster merging into the central cluster, with color indicating stellar velocity (light = v_{\max} , dark = v_{\min}). The dots are star particles at the given time, and the star markers indicate the runaway stars in the group as they form. The total number of stars in the cluster is listed in each panel.

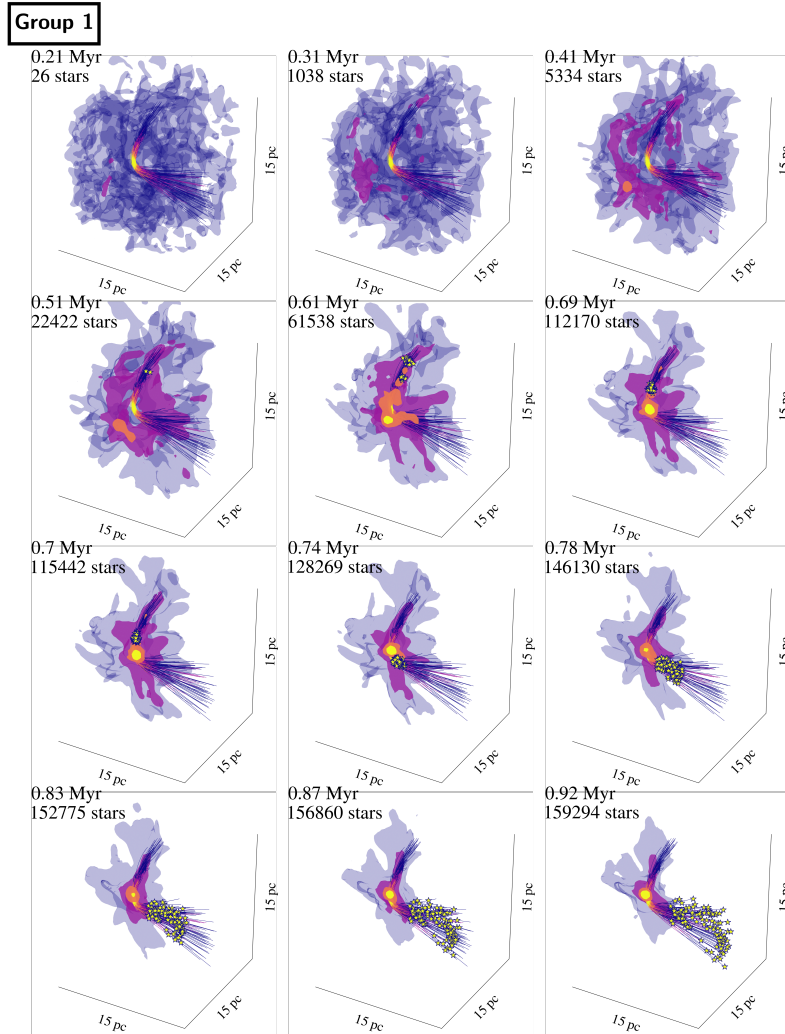


Figure 22: Trajectories of runaway star group 1 originating from a sub-cluster merging into the central cluster, with color indicating stellar velocity (light = v_{\max} , dark = v_{\min}). The isosurfaces show four values of the gravitational potential of both the stars and gas: $|U_g| = 10^{47,48,49,50}$ erg with dark to light as lowest to highest. As the runaway stars form, they are plotted with star markers. The total number of stars in the cluster is listed in each panel.

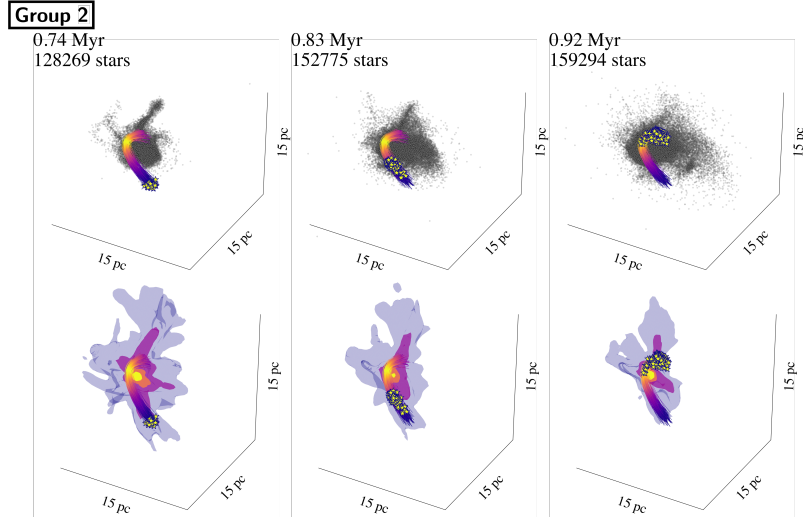


Figure 23: Trajectories of runaway star group 2 originating from a sub-cluster merging into the central cluster, with color indicating stellar velocity (light = v_{\max} , dark = v_{\min}). The top row (analogous to Figure 21) shows dots as all star particles, and the star markers indicate the runaway stars in the group as they form. The bottom row (analogous to Figure 22) shows the same runaway star trajectories with the potential of gas and stars plotted as isosurfaces. The isosurfaces show four values of the gravitational potential of both the stars and gas: $|U_g| = 10^{47,48,49,50}$ erg with dark to light as lowest to highest.

is acceptable as there is no apparent mass preference or cutoff for ejection via SCES.

We apply a second filter to select the runaways belonging to the two groups using stellar age and radial velocity indicated in Figure 18. We select the younger of the two populations in group 2 to focus on a specific sub-cluster. The three most important characteristics for identifying groups of runaways are ejection direction, velocity, and stellar age. The complete list of filters for group 1 and 2 is listed in Table 7. We find that selecting groups based on direction, age, and radial velocity provides a sufficient selection of runaways from a particular sub-cluster merger.

Using these age, velocity, and direction filters, we traced the stars in the two groups back through the evolution and formation of the star cluster to determine their ejection mechanism. Figure 20 is a still from a movie (available in the online version of the paper) showing the formation and ejection of runaway group 1 as well as the formation of the star cluster. In addition to the angular selection outlined in Table 7, we also impose an age restriction to select stars that formed at the same time. In this way, we select only one of the two age groups in group 2.

Figures 20-23 reveal tidal interactions of the sub-cluster with the main cluster as the physical mechanism for ejecting these two groups,

Table 7: Runaway Group Filters.

| Parameter | Group 1 | Group 2 |
|--------------------|--------------------------|--------------------------|
| $\phi_{\vec{v}}$ | $[-18^\circ, 108^\circ]$ | $[-108^\circ, 18^\circ]$ |
| $\theta_{\vec{v}}$ | $[-45^\circ, -9^\circ]$ | $[27^\circ, 72^\circ]$ |
| v_r | $[30, 45]$ km/s | $[55, 105]$ km/s |
| τ | $[0.2, 0.5]$ Myr | $[0.1, 0.2]$ Myr |

Selection ranges for runaways stars in groups 1 and 2. Rows: ϕ and θ directions of velocity, radial velocity from center of mass, and stellar age.

explaining their shared ejection direction, age, and velocity as well as their uniformly sampled IMF mass composition. Group 1 and 2 stars form from distinct sub-clusters. The sub-cluster merges with the assembled central massive cluster becoming tidally disrupted. Some stars are tidally captured while others are slingshotted around the central potential and escape as tidal tails.

The timing of the contraction and expansion of the central cluster potential is crucial for the SCES. In a static potential, the stars falling in could not escape the cluster due to conservation of energy. In SCES, a sub-cluster approaches the central potential as the potential contracts due to the assembly of other sub-clusters and gas infall. After the tidal interaction, as the SCES stars are leaving the central cluster, the potential well expands as star formation from the gas proceeds and the cluster virializes. The timing of the sub-cluster formation and cluster potential evolution determines whether the SCES stars become unbound.

Group 2 is more populous than group 1. This is not because sub-cluster 2 formed more stars, but because the potential driving the tidal force on group 2 is stronger than when group 1 fell in, resulting in more stars being ejected. From Figure 21 we see many stars that do not become runaways forming in the vicinity of group 1 stars, whereas the majority of stars forming near group 2 stars in Figure 23 become runaways.

We find that SCES runaways from later interactions with a deeper potential well result in a higher fraction of stars ejected within a sub-cluster. The tidal interaction is highlighted further by the figures showing trajectories with the evolving potential. At the onset of infall for group 1, the potential is significantly shallower than when group 2 forms. The peak of the potential has just formed and is still migrating when group 1 forms, but it is at its final destination when group 2 forms. However, the potential reaches its peak by the time of slingshot (point of maximum stellar velocity) for both groups. The greater integrated acceleration results in more stars in sub-cluster 2 being ejected than in sub-cluster 1. This correlation allows us to probe the

assembly history of a star cluster from the ejection directions, ages, and velocities of runaway stars.

4.4 DISCUSSION

4.4.1 *Persistence of runaway groups through projection effects*

In our simulated cluster, the anisotropy of runaway stars is directly linked to the sub-cluster merger history. To apply this to observations, we must determine whether the anisotropy can be clearly seen from any given observation angle, and the degree to which the groups of runaways appear to be distinct. We test this by rotating the cluster about a randomly generated unit vector by a randomly generated angle and then re-calculating the escape directions. Figure 24 shows (*top*) a histogram of 1000 random projections and (*bottom*) histograms of the average, maximum, and minimum values of the projections as well as the cumulative sum of runaway fractions per bin. The bins are centered such that the central bin is the most prevalent escape angle for each projection. The histograms are strongly peaked, and in almost every projection (each row in the top panel) a fainter secondary peak in the escape direction is still visible. The secondary peak indicates a second SCES runaway group. The strongly peaked histograms, paired with the steep cumulative sum distribution, tells us that if there is a significant sub-cluster merger history in a cluster resulting in a population of SCES runaways, observers will see an anisotropic distribution of runaway stars regardless of viewing angle.

4.4.2 *Fossils of cluster assembly history*

Groups of runaways ejected by the SCES are distinctly grouped kinematically, temporally, and directionally. We can identify clusters ejected by this mechanism by finding corresponding grouping in age-velocity space and $\phi_{\vec{v}}-\theta_{\vec{v}}$ space. With well-resolved velocities and ages of runaway stars from Gaia, this technique can be applied to find runaways originating from the same sub-cluster. If paired with other groups of SCES runaways, one can unwind the dynamical assembly history of the natal cluster. Furthermore, in the case of multiple runaway groups, the relative size and velocity of each group can indicate which sub-cluster merger happened first. The groups with more stars at higher velocities likely were ejected later. Since SCES groups can only be ejected while the central potential is contracting, the kinetic ages of multiple SCES groups can constrain the timescale of their natal cluster's assembly.

Observations typically only look for runaway O and B-type stars because of their short lifetime. If an O or B star is far from a star forming region, it must be a runaway whereas low-mass stars could

just be field stars. Furthermore, there is a bias towards massive stars for ejection via BSS and DES : Massive stars have a multiplicity fraction of $> 90\%$ (Sana et al., 2014), and because of mass segregation massive stars are clustered in the stellar core and are more likely to have close dynamical encounters (Oh and Kroupa, 2016). Therefore the presence of many low-mass runaway stars is a unique feature of the SCES. There are 3 O stars ($\geq 15 M_{\odot}$) in group 1 and 7 O stars in group 2, so these SCES runaway groups would be detectable using just the O stars. In the case of anisotropic runaways, we predict these high-mass runaways to be accompanied by many more low-mass stars with similar velocities and ages. Depending on how many massive stars are in a runaway grouping, one can estimate how many low-mass stars accompany them using the IMF.

4.4.3 *Observational examples*

The most promising example of the SCES is a group of runaways ejected to the north of R136 in the 30 Doradus star-forming region (Stoop et al., 2024b). Of the 18 runaways ejected < 1 Myr ago, 16 are ejected in the same direction. Additionally, there is an older group of runaways ejected more isotropically suggesting these were ejected by DES or BSS. There is a distinct separation in age-velocity space between the SCES and BSS/DES groups, just as we see in our model. This also confirms detectability of SCES runaways using age and velocity. Stoop et al. (2024b) suggest that the anisotropic runaways were ejected by an interaction with another cluster. Our results further suggest that these ejected stars are the tidal tails produced in the tidal disruption of a late-forming, infalling sub-cluster. Observations show that there is an ongoing merger between two sub-clusters within R136 (Sana et al., 2012). This confirms that R136 formed via hierarchical assembly and supports the case for SCES as the ejection mechanism of its northern runaway star group.

Another example of possible SCES ejection is seen in the runaway OB stars ejected from the YMC NGC 6618, which seem to have a preferential direction. In Figure 6 of Stoop et al. (2024a), the directions of runaways are plotted showing 7 of 13 stars ejected in a $< 90^{\circ}$ region of the sky. Furthermore, in Figure 8 of Stoop et al. (2024a), there is a distinct grouping of stars in velocity and stellar age. These stars are ejected from a cluster ≤ 1 Myr old (Hanson et al., 1997; Hoffmeister et al., 2008; Povich et al., 2009; Ramírez-Tannus et al., 2017), which indicates a dynamical ejection, as no stars have exploded as SNe yet. We argue that this group of runaway stars was ejected via sub-cluster merger rather than individual dynamical interactions.

Figure 12 of Drew et al. (2021) shows the ejection directions of runaway OB stars in NGC 360 and Westerlund 2, colored according to the time of their ejection. The runaway populations from both clus-

ters display some anisotropy, with clusters of runaways moving in roughly the same direction. While it is possible these have all been ejected by the DES, we argue the anisotropy indicates a sub-cluster merger as their origin.

4.4.4 *Runaway binary stars*

Two dynamical binaries² were ejected by SCES in our model, both in group 1. Note that our model did not include any primordial binaries, a topic we will explore in future work. The time evolution of their velocities and orbital separations from the system center of mass is shown in Figure 25 along with the velocity of all SCES runaways. Both systems formed as extremely wide dynamical binaries. After passing through the central potential, they became significantly harder as orbital energy is lost during the dynamical encounter(s) in the dense core. This suggests that tight primordial binaries ejected by SCES are unlikely to be ionized. On the contrary, we show that ejection through SCES can further harden binaries. This needs to be confirmed by analyzing a similar model with primordial binaries.

The hardening effect occurred in both a circular and a slightly eccentric binary. One binary transitioned into a circular ($e = 0.089$) orbit after passing through the central potential, gaining orbital angular momentum through dynamical encounters in the dense core. The other was irregular, settling into a steady eccentric ($e = 0.276$) orbit roughly ≈ 0.1 Myr after peak acceleration.

With the expectation that binaries are preserved and hardened through this mechanism, SCES has the potential to produce runaway binaries with a broad range of properties. This is because runaways produced by SCES are a mostly uniform sampling of the stars formed in a sub-cluster.

Observations of runaway binaries are fairly rare. The binary fraction of observed OB runaway stars is $\approx 8\%$ (Gies and Bolton, 1986; Mason et al., 1998). Simulations of equal mass binary-binary collisions also found that $\approx 10\%$ of O type runaways were binaries (Leonard and Duncan, 1990). The ejection mechanism producing the observed runaway binaries is not always certain.

The ejection mechanism is unknown for two confirmed runaway O-star binaries HD 14633 and HD 15137³ (Gies and Bolton, 1986). They both are in a tight ($P \approx 15, 30$), eccentric ($e \approx 0.7, 0.48$) orbits with low mass companions ($1-3 M_{\odot}$) (McSwain et al., 2007). The low-mass companions could be neutron stars, but neither pulsars nor X-ray

² We refer to binaries as dynamical if they formed dynamically rather than primordially—in the protostellar disk. All binaries in our model are dynamical.

³ HD 14633 and HD 15137 originated in the open cluster NGC 654, approximately 2,400 pc away.

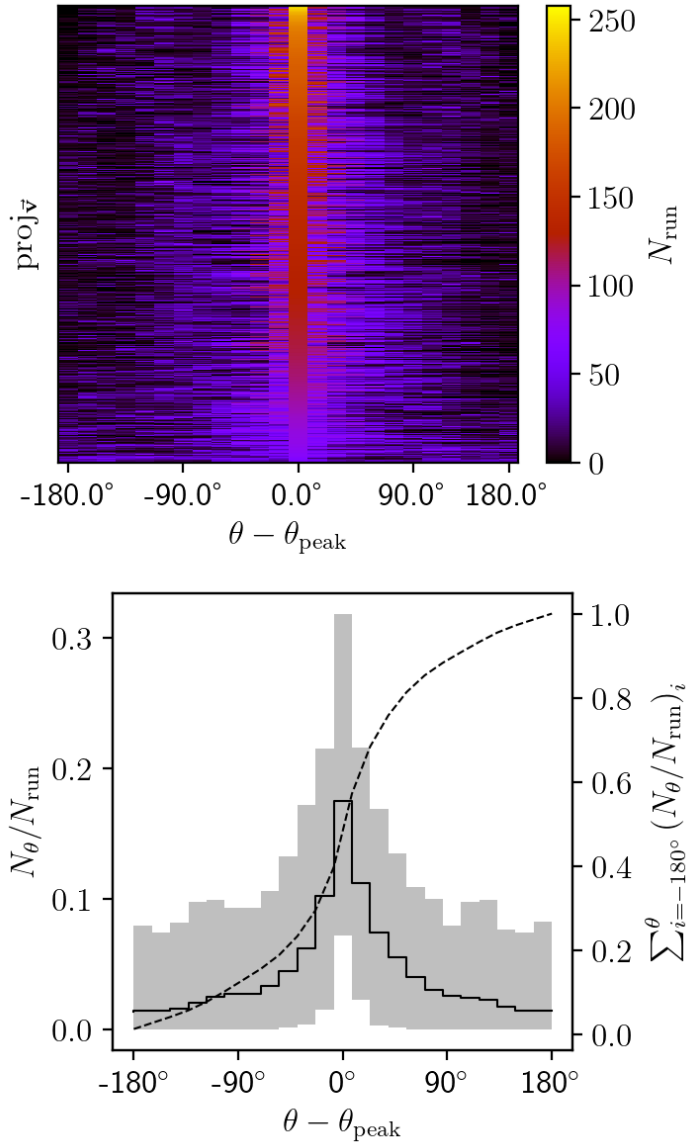


Figure 24: Histograms of runaway star directions from 1,000 different projections. (*top*) 2D histogram showing the 1,000 projections, sorted vertically and centered horizontally by peak number of runaway stars N_{run} , and wrapped around the x-axis. For every projection there is a strong peak. Looking at each row individually, a fainter peak can be seen to the right or left of the peak value. (*bottom*) The *black* histogram is the average value of the projections, while the *grey* area shows the range from maximum to minimum, with values given by the left axis. The *dashed line* shows the cumulative sum of the runaway stars per bin, with values given by the right axis.

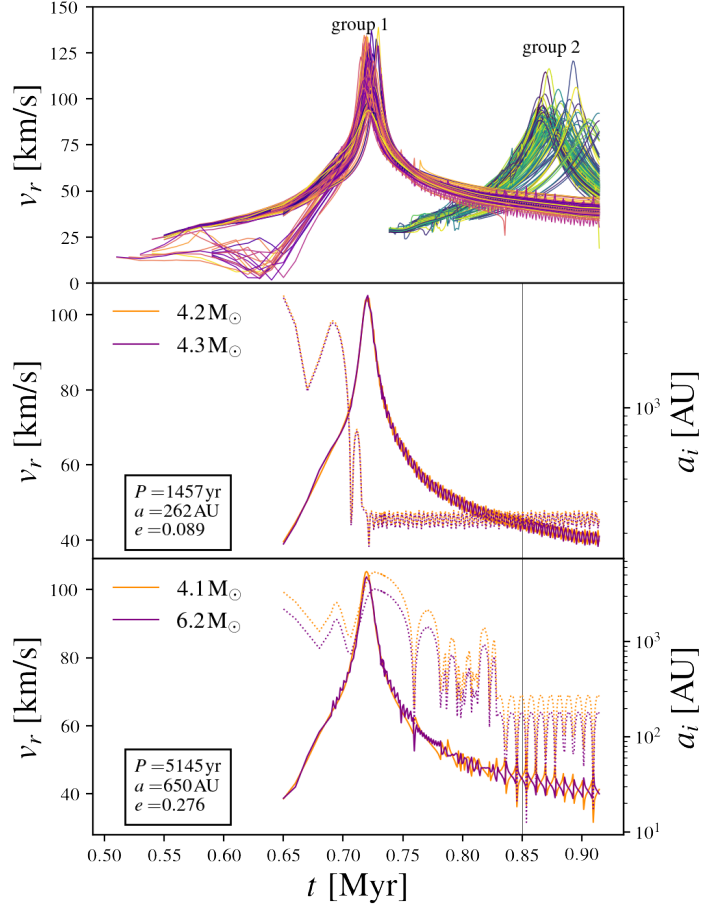


Figure 25: Radial velocity v_r relative to the center of mass over time and orbital properties of the SCES runaway singles and binaries. (*top*) Time evolution of all the runaways in group 1 and 2. (*middle-bottom*) The velocity (*solid*) and semi-major axes a_i (*dotted*) of each member in the two runaway binary stars formed in our simulation. Both are from group 1. The dark lines are the primary stars and the light lines are the companion stars. Orbital properties for each system are listed on the corresponding panel, calculated for the stable orbits after $t = 0.85$ Myr indicated by the vertical black line.

emissions are detected, so ejection via BSS cannot be demonstrated⁴. This leaves the case of a low-mass star companion. Most primordial O star binaries with low-mass companions⁵ have wide orbits ($a > 100$ AU) (Moe and Di Stefano, 2017; Sana et al., 2014). Given our results, it is possible that HD 14633 and HD 15137 originated as wide O-B pairs that were hardened and ejected via SCES.

The SCES ejects binary systems while they are young, and they most likely survive. This means binaries ejected via the SCES can potentially undergo two velocity kicks, with a second kick from the BSS following the SCES⁶. Furthermore, because the binaries are hardened during the SCES, the velocity kick from the BSS will be even higher. This could be a channel for producing hypervelocity stars (HVS). HVS are stars unbound from the Galaxy, which requires $v \gtrsim 400 \text{ km s}^{-1}$ in the Galactic rest frame depending on location and direction. Tauris (2015) found the BSS capable of producing HVS. For HVS with masses $M_* = 0.9, 3.5,$ and $10 M_\odot$ they found kick velocities in the Galactic rest frame up to $v_{\text{grf}}^{\text{max}} = 1, 280, 770,$ and 550 km s^{-1} , respectively. These maximum velocities are only possible via the BSS for particularly favorable binary parameters, such as closer orbits.

Binaries ejected via the SCES become more favorable HVS progenitors via subsequent BSS: they are closer in orbit, further from the galactic disk, and already locally unbound. Therefore, SCES binaries are more likely to produce HVS via a subsequent BSS than if a binary undergoes the BSS while still bound to its parent cluster. This two-step mechanism is a likely channel for producing a HVS that is not pointing at the super-massive black hole (SMBH) at the Galactic center⁷(Hills, 1988).

The runaway binaries produced in our model could not become HVS, as their orbital velocities are too low. Rather, we argue that a close primordial binary could become further hardened by ejection through SCES and thus acquire a fast enough orbital velocity to become a HVS after the SN of its companion.

4.4.5 Importance of initial conditions

Our initial conditions are simplified: a spherical cloud of almost uniform density with isotropic turbulence. In reality, giant molecular

⁴ McSwain et al. (2007) explored the possibility of quiescent neutron stars as the companions. Quiescent neutron stars emit X-rays at a comparable magnitude to O stars but are spectrally distinguishable. X-ray observations with spectral resolution must be done to determine the presence of a quiescent neutron star companion.

⁵ The low-mass companions could also have been massive stars stripped of their envelopes via mass-transfer (Sana et al., 2012).

⁶ A two step ejection method via DES-BSS was introduced first by Pflamm-Altenburg and Kroupa (2010).

⁷ HVS can be produced when a tight binary has a close encounter with the SMBH at the center of the Galaxy and its companion is captured. A large number of late B-type HVS originate in this way (Brown et al., 2014).

clouds (GMCs) forming star clusters are filamentary (see Hacar et al., 2023; Heyer and Dame, 2015; Klessen and Glover, 2016). Sub-clusters forming from spherical clouds are closer to the center of mass and more evenly distributed than those forming from filamentary clouds. Accounting for filamentary initial conditions could dramatically increase the effectiveness of the SCES.

The two sub-clusters that formed furthest from the center of the cluster in M6 were ejected. Sub-clusters that form late or far enough away that they approach the assembling cluster after most of the other sub-clusters have already merged will be most effectively accelerated in the SCES. The sub-cluster must approach during the period when the central potential is still contracting. With more realistic filamentary initial conditions, there will be more sub-clusters formed as the dense gas will be more distributed. We therefore predict a much higher fraction of SCES runaways from star cluster models with more realistic initial conditions due to the increase in the number and infall distance of sub-cluster merger events.

In future work, we plan to import GMCs formed in large-scale galaxy simulations into TORCH to assess the extent to which realistic initial GMCs affect the fraction of runaway stars formed by SCES. This will give us a better idea of how many observed runaways can be attributed to the SCES versus the BSS or the DES. This issue highlights the necessity of using realistic initial conditions, particularly for realistic sub-cluster dynamics in star cluster formation models.

4.4.6 High peak stellar density

The stellar encounter rate per unit volume γ in a star cluster is given by $\gamma \propto \rho^2/\sigma$ where ρ is the stellar density and σ is the velocity dispersion (Verbunt and Hut, 1987). Due to the high initial density and low virial parameter of the initial cloud for our M6 model, the star cluster collapses to a high stellar density, resulting in a high stellar encounter rate. We compare the half-mass density of our model to young (< 10 Myr) Milky Way and Local Group star clusters in Figure 26. We also indicate the time periods of ejection (peak velocity) for the two runaway groups.

The stellar density of our model when the runaway groups are ejected is higher than the observed values. However, we note that this is the density just after core collapse. The cluster will relax to a lower stellar density as it continues to evolve, and, indeed, the stellar density has already begun to decrease at a steady rate following the ejection of group 1. Considering their ages (the youngest is 3 Myr old), the observed clusters used to make Figure 11 are most likely already further post-collapse than our model. Also, aside from R136, none are as massive as our M6 model, which is more characteristic of clusters in starburst galaxies.

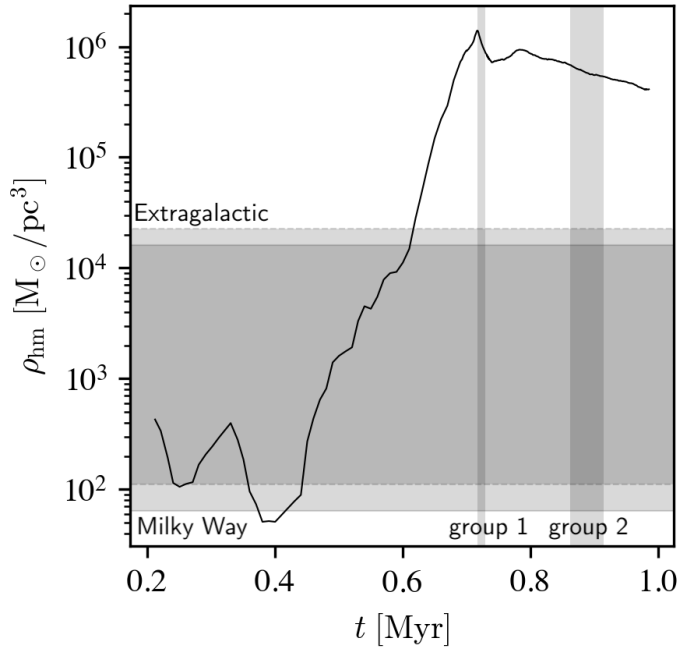


Figure 26: Half-mass stellar density of our model over time. Regions of observed ρ_{hm} values in young clusters (< 10 Myr) are indicated by horizontal grey shaded regions. The dashed border lines show extragalactic clusters and the solid border lines show Milky Way clusters. The vertical shaded regions show the time windows when runaways are dynamically ejected at peak velocity in our M6 model. The observational data was taken from Portegies Zwart et al. (2010).

Regardless, the high stellar density in our model compared to observations implies that the interaction rate could be inflated. The fraction of stars ejected via SCES in clusters that do not reach as high stellar densities during core collapse would likely be lower than in our model. Additional models with more self-consistent initial conditions are needed to constrain the efficiency and frequency of SCES runaways in clusters of varying mass and density.

4.5 CONCLUSIONS

Using a star-by-star simulation of star cluster formation from a gas cloud, we have identified the SCES as a new channel for the origin of runaway stars. This scenario occurs when a sub-cluster forms late, after the rest of the cluster is mostly assembled, and the sub-cluster then falls into the contracting central potential becoming tidally disrupted, ejecting the majority of the stars in the sub-cluster as runaways in tidal tails.

We believe this phenomenon has not been identified earlier due to the over-simplification of initial conditions in many star cluster formation simulations. Using a smooth spherical cloud instead of a cloud more realistically structured by supersonic turbulence results in less energetic sub-cluster mergers since star formation is more centrally concentrated in a spherical cloud. This emphasizes the need for linking scales and using realistic clouds formed in galaxy formation simulations as initial conditions for models of cluster formation.

In order to determine the fraction of runaways formed by SCES, BSS, and DES, we must import a self-consistently formed GMC to model the hierarchical assembly correctly. We also need to include primordial binaries, as they are essential for ejection via the DES or BSS. Furthermore, the simulations must be run for long enough to account for long-term dynamics and the timing of SNe. The M6 simulation in this study was only run for $1.35 t_{\text{ff}}$, equivalent to less than 1 Myr, therefore no SNe have occurred by the time we report on the simulation.

The runaways formed by the SCES are highly correlated with respect to their velocities, ages, and ejection directions. Finding groupings of runaway stars with similar values of these three properties is a clear method to detect runaways formed from the same sub-cluster merger. If anisotropy is observed in a group of runaway stars, this indicates a distinct sub-cluster merger history. Conversely, if the runaways are isotropic, this indicates a mild cluster assembly history and ejection primarily by the DES or BSS channels. A multimodal spatial or velocity distribution of runaway stars could indicate multiple distinct sub-cluster mergers, as seen in our model. Depending on the resolution of observations, these groups of runaways can be used as fossils to trace the assembly history of a star cluster.

An important caveat for confirming an anisotropic distribution of runaway stars is the number of detectable runaways. If a cluster ejects a small number of runaway stars isotropically, even fewer will be massive and detectable. This could falsely imply anisotropy in runaway star ejection directions. A sufficiently large sample of massive runaway stars is needed to exclude this possibility and confirm the anisotropy of the ejection direction. On the other hand, if the small sampling of grouped runaways have the same velocity and kinetic age, it is likely that they were ejected by the SCES.

We have surveyed observational work and found several anisotropic populations of runaway stars. (Stoop et al., 2024b) show that the group of runaways moving north of R136 has properties consistent with ejection via SCES. We also find runaway groups in other clusters that could be produced by SCES, though more analysis needs to be done to confirm this. Regardless, observations of runaway stars must be looked at through an additional lens of possible SCES origins.

The SCES is capable of producing runaway binaries. Two wide binaries in our model were ejected, and through ejection, their orbits hardened significantly. This suggests that primordial binaries can survive ejection and end up with harder orbits. The SCES can thus explain observations of runaway binaries. This scenario also allows for a subsequent BSS ejection, which will be more energetic than a birthplace BSS as the binary progenitor is already unbound and in a hardened orbit. A two-step SCES-BSS ejection is therefore a potential production mechanism for HVS unbound from the Galaxy.

4.6 ACKNOWLEDGEMENTS

We thank the referee Mark Gieles for his insightful comments, one of which led to Sect. 4.4.6. We thank Yuri Levin for pointing out runaway binary stars as a potential signature of SCES. B.P. was partly supported by a fellowship from the International Max Planck Research School for Astronomy and Cosmic Physics at the University of Heidelberg (IMPRS-HD). M.-M.M.L., B.P., and E.P.A. were partly supported by NSF grants AST18-15461 and AST23-07950. E.P.A. also received support from NASA Astrophysical Theory grant 80NSSC24K0935. C.C.-C. is supported by a Canada Graduate Scholarship - Doctoral (CGS D) from the Natural Sciences and Engineering Research Council of Canada (NSERC). This work used Stampede 2 at TACC through allocation PHY220160 from the Advanced Cyberinfrastructure Coordination Ecosystem: Services & Support (ACCESS) program, which is supported by National Science Foundation grants 21-38259, 21-38286, 21-38307, 21-37603, and 21-38296. The code development that facilitated this study was done on Snellius through the Dutch National Supercomputing Center SURF grants 15220 and 2023/ENW/01498863. S.M.A. acknowledges the support of NSF grant AST-2009679. R.S.K.

and S.C.O.G. acknowledge financial support from the European Research Council via the ERC Synergy Grant “ECOGAL” (project ID 855130), from the Heidelberg Cluster of Excellence (EXC 2181 - 390900948) “STRUCTURES”, funded by the German Excellence Strategy, and from the German Ministry for Economic Affairs and Climate Action in project “MAINN” (funding ID 50002206). The team in Heidelberg also thanks *The Länd* and the German Science Foundation (DFG) for computing resources provided in bwHPC supported by grant INST 35/1134-1 FUGG and for data storage at SDS@hd supported by grant INST 35/1314-1 FUGG. The authors acknowledge Interstellar Institute’s program “II6” and the Paris-Saclay University’s Institut Pascal for hosting discussions that nourished the development of the ideas behind this work.

EARLY DYNAMICAL MASS SEGREGATION DURING CLUSTER ASSEMBLY

5.1 ABSTRACT

Mass segregation is seen in many star clusters, but whether massive stars form in the center of a cluster or migrate there dynamically is still debated. N-body simulations have shown that early dynamical mass segregation is possible when sub-clusters merge to form a dense core with a small crossing time. However, the effect of gas dynamics on both the formation and dynamics of the stars could inhibit the formation of the dense core. We aim to study the dynamical mass segregation of star cluster models that include gas dynamics and self-consistently form stars from the dense substructure in the gas. Our models use the TORCH framework, which is based on AMUSE and includes stellar and magnetized gas dynamics, as well as stellar evolution and feedback from radiation, stellar winds, and supernovae. Our models consist of three star clusters forming from initial turbulent spherical clouds of mass 10^4 , 10^5 , $10^6 M_{\odot}$ and radius 11.7 pc that have final stellar masses of $3.6 \times 10^3 M_{\odot}$, $6.5 \times 10^4 M_{\odot}$, and $8.9 \times 10^5 M_{\odot}$, respectively. There is no primordial mass segregation in the model by construction. All three clusters become dynamically mass segregated at early times via collapse confirming that this mechanism occurs within sub-clusters forming directly out of the dense substructure in the gas. The dynamics of the embedded gas and stellar feedback do not inhibit the collapse of the cluster. We find that each model cluster becomes mass segregated within 2 Myr of the onset of star formation, reaching the levels observed in young clusters in the Milky Way. However, we note that the exact values are highly time-variable during these early phases of evolution. Massive stars that segregate to the center during core collapse are likely to be dynamically ejected, a process that can decrease the overall level of mass segregation again.

5.2 INTRODUCTION

Most stars form from giant molecular clouds (GMCs) in groups of tens to millions of stars called star clusters (see, e.g., Krause et al., 2020; Lada and Lada, 2003; Portegies Zwart et al., 2010). Models suggest that star clusters form from the global hierarchical collapse of GMCs (Grudić et al., 2018a; Vázquez-Semadeni et al., 2017). As the GMC undergoes gravoturbulent collapse (Larson, 1981), fragmenta-

tion leads to the formation of dense star-forming clumps (Klessen and Glover, 2016; Mac Low and Klessen, 2004; McKee and Ostriker, 2007) called sub-clusters. These sub-clusters eventually merge if they are gravitationally bound, collapsing into a single star cluster.

Many star clusters exhibit signs of mass segregation where the massive stars are concentrated in the center of the cluster (Hillenbrand and Hartmann, 1998). This can happen dynamically when massive stars migrate to the center via two-body interactions (Spitzer, 1969), or it can occur primordially when massive stars are preferentially formed in the center where the gas density is highest e.g., Klessen and Burkert, 2000; McKee and Tan, 2003. Determining whether and when one of these modes of mass segregation dominates is essential for understanding the formation of stars and assembly of star clusters; whether star formation is spatially distributed randomly or according to mass presents two entirely different pictures of star formation.

If a young star cluster is observed to be mass segregated earlier than expected given the cluster’s crossing time, this would necessitate primordial mass segregation. However, N-body models presented in Allison et al. (2009) suggest a mechanism that allows for clusters to become dynamically segregated at much earlier times. They suggested that the collapse¹ of the star cluster – when sub-clusters merge and create a short-lived dense core – facilitates efficient and early dynamical mass segregation. However, it is unclear whether sub-clusters forming self-consistently from a collapsing GMC would still merge in a way that creates this dense core. Furthermore, including gas dynamics could also inhibit the collapse of the cluster’s central region.

We examine the mass segregation in the M4, M5, and M6 star cluster models first described in Section 3.3. These simulations follow individual stars forming from an initially turbulent spherical cloud of gas. By construction, the stars in our model are not primordially mass segregated. Thus we specifically study the timescale on which *dynamical mass segregation* occurs. We find that this process becomes important much earlier than proposed by Allison et al. (2009). We confirm that sub-clusters forming self-consistently from the cloud’s substructure do form the dense cores needed for early dynamical segregation, and the embedding gas does not inhibit the collapse necessary for this mechanism.

In Section 5.3 we present the progression of mass segregation over each cluster’s lifetime. In Section 5.4 we examine the expected time scales for dynamical mass segregation and compare the degree of mass segregation in our clusters to observations in order to address whether primordial mass segregation is necessary to explain the mass segregation observed in young Galactic clusters. We conclude in Section 5.5.

¹ Not to be confused with the core collapse that occurs at late dynamical times after the star cluster has already assembled.

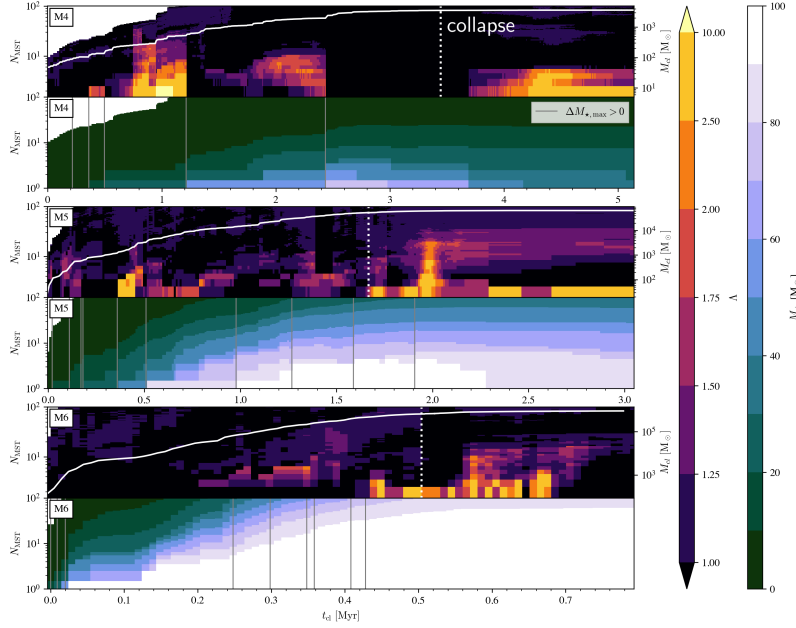


Figure 27: The three rows with two grouped plots correspond to the M4, M5, and M6 models. The following descriptions apply to the two plots in each row. *Top:* Mass segregation ratio Λ over time for the N_{MST} most massive stars in each cluster. The vertical dotted white lines indicate the time of collapse, where R_{rms} reaches a minimum. The solid white lines correspond to the right vertical axis showing the stellar mass of the cluster. *Bottom:* Mass of the $N_{\text{MST}}^{\text{th}}$ most massive star in each cluster. The grey vertical lines indicate the formation of a new most-massive star ($N_{\text{MST}} = 1$). As these are often not in the core, the time of formation, particularly in M4, corresponds to a drop in the apparent mass segregation. Note that each cluster was run to $\approx 1.5t_{\text{ff}}$, leading to different absolute time scales.

5.3 RESULTS

We quantify the degree of mass segregation in a star cluster using a minimum spanning tree (MST) method as described by Allison et al., 2009. The basic is to use the total edge length of the MST formed by a group of stars to quantify their proximity to each other. This method compares the total edge length (ℓ_{massive}) of the MST made by the N_{MST} most massive stars in a cluster to the average total edge length (ℓ_{rand}) of n_{sample} MSTs formed by the same number of randomly selected stars. This gives a simple and comprehensive way of comparing the proximity of massive stars to that of all the stars in the cluster. This quantifies the mass segregation as a mass segregation ratio Λ , calculated by

$$\Lambda = \frac{\langle \ell_{\text{rand}} \rangle}{\ell_{\text{massive}}} \pm \frac{\text{ff}_{\text{rand}}}{\ell_{\text{massive}}} \quad (52)$$

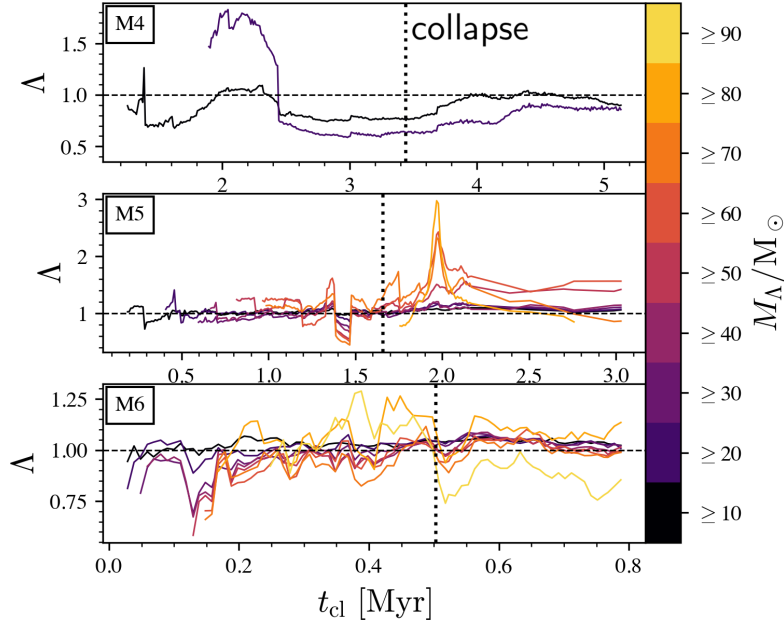


Figure 28: Mass segregation ratio Λ over time for all stars above a given mass threshold M_Λ shown on the color bar. Λ is only calculated if there are ≥ 5 stars with mass $\geq M_\Lambda$. The threshold for mass segregation is $\Lambda > 1$, above the *horizontal dashed line*. The *vertical dotted lines* indicate the time of collapse, where R_{rms} reaches a minimum. Note the variable time scales in each panel.

where σ_{rand} is the standard deviation of the ℓ_{rand} values. Mass segregation is present when $\Lambda > 1$. We use $n_{\text{sample}} = 500$ sets of randomly selected stars for calculating $\langle \ell_{\text{rand}} \rangle \pm \sigma_{\text{rand}}$.

Parker and Goodwin (2015) review the currently used measures of mass segregation and found the MST method to be the most accurate for measuring classical mass segregation, i.e., when massive stars are concentrated in particular regions of space. This review also finds that a random distribution of stars can result in values of $\Lambda = 1-2$ for $N_{\text{MST}} \leq 20$, and advise caution when interpreting values of Λ below 2 for low N_{MST} . However, they only used $N_\star = 300$ stars in this test. The M5 and M6 clusters form $N_\star > 15,000$ and $N_\star > 150,000$ stars, respectively. The likelihood that the 20 most massive stars were all formed in the center of these clusters randomly is negligible. Therefore, for these clusters we consider all values of $\Lambda > 1$ to signify mass segregation. The M4 cluster only forms $N_\star > 500$ stars, so as a precaution we only consider mass segregation in M4 to be significant if $\Lambda > 2$. We only consider bound stars for all the calculations in this study.

In the top half of each row in Figure 27, we plot the time evolution of the mass segregation ratio Λ for the $N_{\text{MST}} \leq 100$ most massive stars in each cluster. The bottom half of each row shows the mass of the N_{MST} most massive stars. All three clusters go through peri-

ods of significant mass segregation. The state of mass segregation is also highly variable throughout the cluster lifetime; mass segregation is not monotonic. M4 becomes mass segregated from $t_{\text{cl}} \approx 0.75\text{--}1.25$ Myr for $N_{\text{MST}} \leq 7$ and mildly so from $t_{\text{cl}} \approx 1.75\text{--}2.4$ for $N_{\text{MST}} \leq 10$. At the end of these time periods, the cluster transitions sharply to an inverse mass segregated state with $\Lambda < 1$. From the bottom half of the M4 plot we can see that this is due to a new most-massive star being formed on the outskirts of the cluster, reducing Λ for all values of N_{MST} . M4 achieves a stable state of mass segregation for $N_{\text{MST}} \leq 5$ by $t_{\text{cl}} \approx 3.7$ Myr. This is after the collapse of the cluster, the point of maximum compression where the sub-clusters have merged to form a short-lived dense core. The dense core begins to expand as the collapsed cluster relaxes. The onset of gas expulsion also contributes to cluster expansion. In lower star formation efficiency (SFE) clouds ($\text{SFE} \leq 30\%$) gas expulsion is the dominant cause of expansion, while higher SFE clusters expand due to stellar dynamics (Pfalzner and Kaczmarek, 2013). The M4 cluster expansion is driven by gas expulsion, whereas the M5 and M6 cluster expansion is due to dynamical relaxation.

M5 has similar episodes, with mass segregation from $t_{\text{cl}} \approx 0.35\text{--}0.5$ for $N_{\text{MST}} \leq 4$ and $t_{\text{cl}} > 1.9$ Myr for $N_{\text{MST}} \leq 20$ after collapse. Just before the onset of mass segregation at times $t_{\text{cl}} = 0.35$ Myr and $t_{\text{cl}} = 1.9$ Myr a new most massive star formed. Unlike in the M4 case, these massive stars formed near the center of mass of the cluster, thereby increasing Λ . This is dynamically induced primordial mass segregation. As the cluster assembles, dense gas is also pulled to the center of mass allowing for the formation of a massive star in the center of the cluster. This is more likely during collapse when segregation is most rapid, as is seen with the massive star that formed at $t_{\text{cl}} = 1.9$ Myr just after collapse. After $t_{\text{cl}} = 2$ Myr, all stars $N_{\text{MST}} \leq 100$ show signs of mass segregation with the exception of $N_{\text{MST}} = 3\text{--}7$ where $\Lambda < 1$. This region of inverse mass segregation is caused by an interaction at time $t_{\text{cl}} = 2.1$ Myr in which the fourth most massive star ($N_{\text{MST}} = 4$) is dynamically ejected from the cluster's core. Then, at $t_{\text{cl}} = 2.27$ Myr the third and fourth most massive stars swap places due to the third star losing mass from stellar winds. The ejected massive star stays in the outskirts of the cluster for the remainder of the simulation, affecting Λ values for $N_{\text{MST}} = 3\text{--}7$.

The M6 cluster begins to show signs of mass segregation for $N_{\text{MST}} \geq 3$ as early as $t_{\text{cl}} = 0.2$ Myr after formation. An episode of mass segregation for $N_{\text{MST}} \leq 20$ occurs from $t_{\text{cl}} = 0.56\text{--}0.68$ Myr, which is just after collapse. This ends when the second most massive star is dynamically ejected from the core, decreasing all values of Λ . The higher stellar mass of the M5 and M6 cluster results in a denser core and therefore more dynamical ejections of the most massive stars. The most massive stars are more susceptible to these ejections as dy-

namical friction drags them more quickly to the center of the core. This is one of the reasons why runaway stars—stars unbound to their birth cluster (see, e.g., Blaauw, 1961; Fujii and Portegies Zwart, 2011; Hoogerwerf et al., 2000; Poveda et al., 1967)—are preferably massive OB-type stars (Oh and Kroupa, 2016).

While star formation continues and massive stars remain young, Λ can be highly variable because new massive stars are forming throughout the cluster and are losing mass through stellar winds. To remove some of the dependence of Λ on individual stars, we also calculated the average Λ for all stars above a given stellar mass M_Λ , which is shown in Figure 28. We only calculate Λ if there are $N_{\text{mass}} \geq 5$ stars with mass $\geq M_\Lambda$. If there are $N_{\text{mass}} \geq 500$ stars above a mass, we set $N_{\text{mass}} = 500$ and average the MST length of 100 sets of randomly selected $N_{\text{mass}} = 500$ massive stars to increase computational efficiency.

The M4 cluster shows immediate mass segregation for stars above $20 M_\odot$ which sharply transitions towards uniformity/inverse mass segregation just after $t_{\text{cl}} = 2.4$ Myr. This is the same feature seen in Figure 27 when a new most massive star formed in the outskirts of the cluster. Λ values in M4 begin to increase towards uniformity after collapse. M5 has some fluctuations in the segregation of the high mass stars, with a prominent peak at $t_{\text{cl}} = 1$ Myr for stars above $60 M_\odot$. This peak occurs after collapse, when the dense core drove efficient migration of the massive stars to the center. For the next megayear, Λ for stars more massive than $50 M_\odot$ shows consistent mass segregation. Higher mass stars above $70 M_\odot$ evolve to be more uniform/slightly inverse mass segregated, though. This is a result of dynamical ejection, which acts on the most massive stars in a cluster as they reach the highest levels of mass segregation. The higher mass cutoffs also include many fewer stars in the calculation, meaning they are more sensitive to one star being ejected from the cluster core.

Stars below $80 M_\odot$ in the M6 cluster show signs of little to no mass segregation towards the end of the simulation $t_{\text{cl}} \geq 0.55$ Myr when the cluster starts to relax. Before this, Λ for stars below $80 M_\odot$ is highly variable due to the high star formation rate. This is also before the sub-clusters have merged, so global mass segregation can not take place.

As in the M5 cluster, Λ in the M6 cluster has peaks and subsequent dips. However, there are more peaks and dips because M6 has more sub-cluster mergers before they all coalesce during collapse. The peaks before collapse are caused by similar mass sub-cluster mergers. The final peak after collapse occurs at $t_{\text{cl}} = 0.56$ Myr for stars above $80 M_\odot$, and afterwards Λ levels off at $\Lambda = 1.2$ indicating clear mass segregation. The most massive stars in M6, however, show less mass segregation after collapse due to their ejection from the core. The high concentration of the most massive stars in the dense

core raises the probability of their ejection through a strong dynamical encounter. The low number of stars with $M \geq 90 M_{\odot}$ results in Λ dipping below one if even a single star in this mass bin is ejected from the core.

5.4 DISCUSSION

5.4.1 Time Scales

An observed star cluster is determined to have primordial mass segregation if there is mass segregation before the expected segregation timescale of the cluster. A recent study that consistently models individual star formation from gas found that sub-clusters form primordially segregated (Guszejnov et al., 2022b). They do not indicate Λ values for individual stars using N_{MST} , but rather the global Λ for all stars $\geq 5 M_{\odot}$. Despite the primordial mass segregation in the sub-clusters, the global Λ still varies as their cluster model evolves. This is in contrast to the results in Allison et al. (2009) who found that Λ mostly increases after collapse, never decreasing back down to $\Lambda = 1$. McMillan et al. (2007) also found in their pure N-body simulations that $\Lambda > 1$ values in sub-clusters are retained through mergers. These conflicting results suggest that gas dynamics play a significant role in the long term relaxation and dynamical mass segregation of the cluster.

We calculate the dynamical segregation timescale for our clusters to see when mass segregation occurs with respect to it. The expected time for a star of mass M to dynamically segregate in a uniform spherical cluster is given by (Allison et al., 2009; Spitzer, 1969)

$$t_{\text{seg}} \approx \frac{\langle m_{\star} \rangle}{M} \frac{N_{\star}}{8 \log N_{\star}} \frac{R_{\text{rms}}}{\sigma_{\text{v}}}, \quad (53)$$

where $\langle m_{\star} \rangle$ and N_{\star} are the average mass and number of stars in the cluster, $R_{\text{rms}} = \sqrt{\langle \|\Delta \mathbf{x}\|^2 \rangle}$ is the root mean square radius from the center of mass, and σ_{v} is the stellar velocity dispersion in the center of mass frame. We note that this is an idealized approximation of the segregation time, as our clusters are far from spherical at early times.

We must address the effect of our mass agglomeration routine on the segregation timescale in our clusters. We agglomerate stars below $4 M_{\odot}$. With an IMF sampling mass of $10^5 M_{\odot}$, our agglomeration routine increases $\langle m_{\star} \rangle$ from 0.575 to 5.390 M_{\odot} and decreases N_{\star} from 174,432 to 18,243. Using Eq. 53, we find that the segregation time of a cluster with agglomeration is 20.6% larger than the segregation time for a cluster without agglomeration. This is an approximation that assumes that agglomeration does not change the radius of the cluster or stellar velocity dispersion. This result means that clusters with the true Kroupa IMF will dynamically mass segregate even more efficiently than our model with the agglomerated IMF.

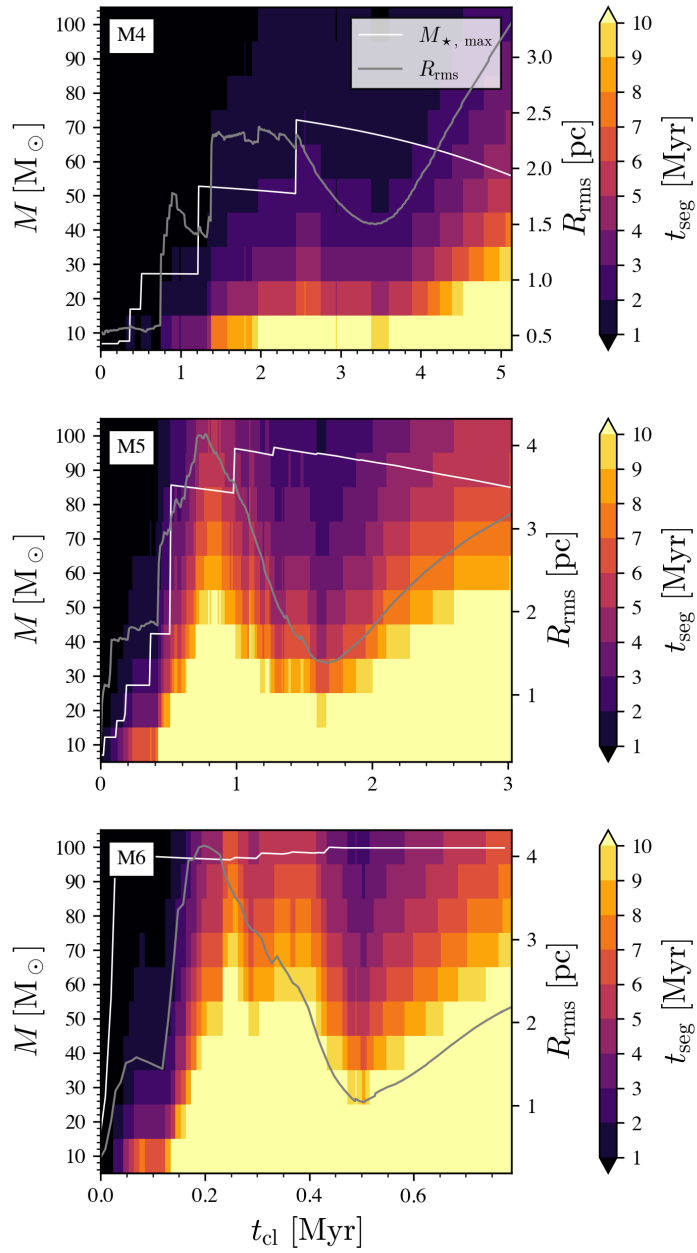


Figure 29: Dynamical segregation time for a star with mass M over time based on the cluster's properties. The white line indicates the mass of the most massive star, which can decrease due to mass loss from stellar winds. The grey line shows the evolution of the cluster radius R_{rms} . Note that the dip in the evolution of R_{rms} indicates the time of collapse.

Figure 29 shows the time evolution of t_{seg} as a function of M for each of the modeled clusters. The mass of the most massive star is indicated by the white line and the grey line shows the evolution of R_{rms} . In all three clusters, there is a distinct wave pattern of high and low t_{seg} values which correspond to the variations in R_{rms} during cluster assembly. Over time, N_{\star} and σ_v only increase and $\langle m_{\star} \rangle$ is roughly constant by construction. The segregation time increases as more pockets of dense gas begin to form spatially separate sub-clusters of stars, and decreases when the sub-clusters are pulled together by gravity. The lowest t_{seg} value corresponds to the maximum contraction of the assembling cluster during collapse, after which the cluster expands and t_{seg} increases again.

Comparing Figure 29 to Figure 27, one can see a direct correlation between the episodes of high mass segregation to low segregation times, particularly the time period just after the dense core forms from collapse. This is the mass segregation mechanism described in Allison et al. (2009) in which the collapse of a star cluster forming from many sub-clusters creates a short-lived dense core that allows for early and efficient dynamical mass segregation in young clusters. They discovered this mechanism with models of $N = 1,000$ star particles initially distributed in sub-clusters. Our model confirms that these results hold for sub-clusters forming self-consistently from the dense substructures in a collapsing cloud. One key difference in our results is that they found Λ to steadily increase after collapse, whereas our clusters show more variability. We suspect this is due to the gas dynamics in our model slowing the relaxation of the star particles.

Starting with the M4 cluster, the first episode of mass segregation is from $t_{\text{cl}} \approx 0.8\text{--}1.2$ Myr, which occurs before t_{seg} begins to increase as more stars form. The final period of steady mass segregation begins at $t_{\text{cl}} \approx 3.7$ Myr, which is right after the period of low t_{seg} due to the collapse of the cluster. This allows the most massive stars to efficiently reach a state of mass segregation.

The M5 cluster also has an episode of mass segregation when the cluster is young $t_{\text{cl}} \approx 0.4$ Myr and just after the collapse when t_{seg} is lowest. The collapse induced mass segregation occurs at $t = 1.8\text{--}2$ Myr, just 0.2 Myr after the maximum contraction of the cluster. By the time mass segregation sets in, t_{seg} has risen considerably. At $t_{\text{cl}} = 1.95$ Myr, there is pronounced mass segregation of $\Lambda \geq 2$ for $N_{\text{MST}} \leq 20$ which corresponds to stellar masses between $M = 50\text{--}100 M_{\odot}$. The segregation timescale for stars in this mass range is between $t_{\text{seg}} = 2\text{--}6$ Myr. For stars between $M = 50\text{--}70 M_{\odot}$, $t_{\text{seg}} = 3\text{--}6$ Myr which is greater than the age of the cluster. If observing this cluster at that time, one would mistakenly conclude that the massive stars have segregated before the expected dynamical time and therefore must have been primordially segregated. This can occur if observing the cluster just after the initial collapse.

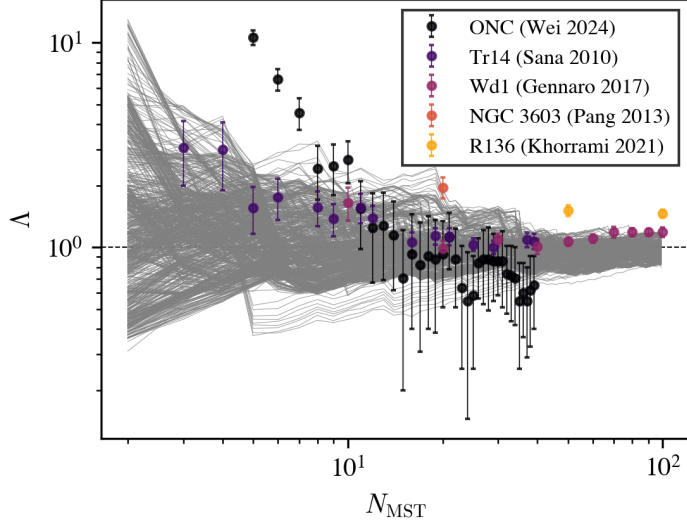


Figure 30: Mass segregation ratio Λ versus number of most massive stars N_{MST} for young Galactic clusters. Each grey line represents one snapshot in time for each of the M4, M5, and M6 clusters.

The star formation in M6 is too rapid for mass segregation to set in before multiple sub-clusters form. However, the initial collapse does produce an episode of mass segregation from $t_{\text{cl}} = 0.56\text{--}0.68$ Myr. The minimum t_{seg} values due to collapse occurs at $t_{\text{cl}} = 0.5$ Myr. The two most massive stars are segregated before the collapse, and just 0.06 Myr after the maximum contraction the 20 most massive stars become mass segregated as well. The 20 most massive stars ($N_{\text{MST}} \leq 20$) have $M \geq 90 M_{\odot}$. The segregation timescale for these stars during the time period of segregation ranges from $t_{\text{seg}} = 3\text{--}6$ Myr. This is again much older than the age of the cluster.

5.4.2 Observational comparisons

The mass segregation ratio Λ for five young clusters in the Milky Way is shown in Figure 30, with the values for our three models indicated in grey. This allows us to assess whether the state of mass segregation observed in these clusters can reasonably be attained with only dynamics. Due to the chaotic nature of star formation and dynamics, we are not expecting an exact match in Λ for a given N_{MST} value. Rather, we are looking to see whether the Λ values in our models reach those seen in observations for a given N_{MST} . For reference, the cluster mass and age of our models and the Milky Way clusters are listed in Table 8.

The degree of mass segregation in the Trumpler 14 (Tr14; Sana et al., 2010), Westerlund 1 (Wd1; Gennaro et al., 2017), and NGC 3603 (Pang et al., 2013) clusters are well within the Λ values of our simulated clusters for the same N_{MST} . Each of these studies concluded that the

mass segregation of these clusters can be explained by dynamics and does not have to be primordial because of their segregation timescale. Our results confirm this.

The young massive cluster Radcliffe 136 (R136, see, e.g., Massey and Hunter 1998 or Crowther et al. 2010) embedded in the 30 Doradus star-forming region is mass segregated with $\Lambda \approx 1.5$ at $N_{\text{MST}} = 50, 100$ (Khorrami et al., 2021). At times, our models are slightly segregated at these N_{MST} , with the maximum values reaching $\Lambda \approx 1.1 - 1.2$. Khorrami et al. (2021) notes that the detection completeness is very low for low-mass stars in the center of the cluster. A young massive cluster such as R136 is likely to have a dense stellar core with many low-mass stars. More low-mass stars in the center of the cluster would lower Λ , so it is probable that these values of Λ are upper limits for R136. With this we conclude that the mass segregation in R136 can be reasonably attained through early dynamics.

All values of Λ in the Orion Nebula Cluster (ONC; Wei et al., 2024) are reached by our model except for the massive Trapezium stars at $N_{\text{MST}} \leq 7$. Due to the high multiplicity fraction of massive stars (Moe and Di Stefano, 2017), it is highly likely that the Trapezium stars are binaries rather than single stars. The binaries would undergo mass segregation as a system, increasing Λ for two stars instead of one. We do not include primordial binary formation in our model, which can explain why our models reach the high Λ values seen in the ONC at half the value of N_{MST} .

The Allison et al. (2009) model, however, did reproduce the mass segregation seen throughout the ONC dynamically. Because of the stochastic nature of star formation and sub-cluster dynamics, our results will vary with different realizations of the initial turbulent seed of the clouds. It is likely that by performing more simulations we would produce a group of $N_{\text{MST}} = 7$ highly centralized stars resembling the Trapezium group.

Wei et al. (2024) find the ONC to be in a super-virial state and expanding. If the ONC formed through hierarchical assembly, the expanding state of the ONC implies that it is post-collapse. This is consistent with the scenario that the ONC became dynamically mass segregated during initial collapse, and is now expanding². It is also possible that some of the Trapezium stars formed in the center of the ONC if their progenitor gas clumps became mass segregated during collapse.

Up to now, we've compared observations to our model with no primordial mass segregation by construction. We find that observations

² It has also been suggested that the super-virial state of the ONC might be due to a slingshot effect, where oscillations in the gas filament that formed the ONC led to the ejection of the cluster (see Matus Carrillo et al., 2023; Stutz, 2018; Stutz and Gould, 2016). In this scenario, it is still possible that the initial collapse of the ONC occurred before expulsion by the filament, allowing for the Trapezium stars to efficiently migrate to the center.

Table 8: Star cluster properties.

| | M_{cl} [M_{\odot}] | Age [Myr] |
|---------|---------------------------------|-----------|
| M4 | 3.6×10^3 | 5.5(3.1) |
| M5 | 6.5×10^4 | 3.1(1.9) |
| M6 | 8.9×10^5 | 0.8(0.4) |
| ONC | 1.8×10^3 | 2.2 |
| Tr14 | $4.3^{+3.3}_{-1.5} \times 10^3$ | 0.3 – 0.5 |
| Wd1 | 5×10^4 | 4 – 5 |
| NGC3603 | 10^4 | 1 |
| R136 | 1.5×10^4 | 1 – 2 |

The final age and stellar mass of our modeled clusters and the Galactic clusters shown in Figure 30. We also list the average stellar age of our modeled clusters in parentheses. ONC mass Hillenbrand and Hartmann (1998), ONC age Reggiani et al. (2011), NGC3603 mass Harayama et al. (2008). All other observed values are taken from the papers reporting their mass segregation.

of early mass segregation can be reproduced with no primordial mass segregation. Therefore, to confirm the existence of primordial mass segregation, massive stars must be observed in the center of a cluster as they are forming. Recent ALMA observations of 11 dense proto-clusters ($M_{\text{clump}} \geq 10^3 M_{\odot}$) find significant mass segregation of their prestellar and protostellar cores (Xu et al., 2024). This indicates that stars forming within sub-clusters could be primordially mass segregated. If this is the case, as they merge during the collapse of the cluster we expect the mass segregation will only increase. However, it is unclear whether primordially mass segregated sub-clusters remain that way until they merge. The concentration of massive stars in the center of a sub-cluster subjects them to a higher chance of being dynamically ejected. With these new results, sub-grid models of star formation should perhaps place massive stars preferentially towards the center of sub-clusters. Then one could determine whether primordial mass segregation persists through the dynamical evolution of the cluster.

5.5 CONCLUSIONS

We performed simulations of star-by-star cluster formation from turbulent self-gravitating gas clouds, taking into account stellar feedback in the form of radiation, stellar winds, and supernovae. We found that dynamical mass segregation can occur early on during the hierarchical formation process, when sub-clusters collapse and form a dense

core with a much smaller crossing time (as proposed by Allison et al. 2009 for purely stellar dynamical systems).

Due to the hierarchical formation of star clusters, the timescale over which massive stars dynamically segregate t_{seg} varies greatly as the size of the cluster changes. There are two points in a cluster's lifetime when t_{seg} is significantly lower. First, when the cluster is just forming and only contains a single site of star formation, and second during the initial collapse when the sub-clusters merge into a central cluster forming a short-lived dense core. These two time periods allow massive stars to segregate efficiently, with $t_{\text{seg}} \leq 2$ Myr for the most massive stars. During initial collapse, the most massive stars in each of our models ($\geq 20 M_{\odot}$, $\geq 50 M_{\odot}$, $\geq 90 M_{\odot}$ for M4, M5, M6) underwent efficient mass segregation reaching $\Lambda > 1$ within $t_{\text{seg}} < 0.5$ Myr. The variation of t_{seg} over the lifetime of a cluster means that the integrated t_{seg} may be shorter than the value given by the cluster's current state. Therefore, a young cluster being mass segregated earlier than expected does not necessarily indicate primordial mass segregation.

Mass segregation can occur while star formation is ongoing. This means massive stars and massive star-forming clumps alike will migrate to the center, thereby increasing the likelihood of a massive star being born in the center of the cluster. This can lead to primordial mass segregation if a massive star is formed during the initial collapse of a young cluster.

The mass segregation ratio Λ in young clusters is highly variable due to the ongoing star formation, stellar mass loss, and energetic kinematics of sub-cluster assembly. There are time periods of significant mass segregation in all three clusters that last for 0.1–0.3 Myr. There are also time periods without apparent mass segregation, which usually occur after the dynamical ejection of a massive star from the core. As more massive stars fall into the dense core, they are more likely to be ejected by a strong dynamical encounter. Mass segregation and dynamical ejection are two competing physical processes, and massive stars are most susceptible to both. The interplay and balance of these two processes needs further investigation. Given these variations in Λ before the cluster is fully relaxed, it is unclear how long primordial mass segregation would last.

In summary, our results conclusively show that young clusters can become mass segregated through early dynamics. Efficient dynamical mass segregation is achieved when the initial collapse of the star cluster forms a dense core with a much smaller crossing time. We have demonstrated that the degree of mass segregation seen in young Galactic clusters is also seen in our models and can therefore be achieved through dynamics alone. During collapse, massive stars are more likely to form primordially segregated as massive star-forming clumps will also promptly approach the center of mass. Our findings

also indicate that Λ is highly variable at early times. New observations point to primordial mass segregation, at least on the sub-cluster scale, so further work is needed to confirm whether primordial mass segregation would survive cluster assembly or dissipate in a model that includes gas dynamics.

5.6 ACKNOWLEDGEMENTS

B.P. was partly supported by a fellowship from the International Max Planck Research School for Astronomy and Cosmic Physics at the University of Heidelberg (IMPRS-HD). M.-M.M.L., B.P., and E.A. were partly supported by NSF grants AST18-15461 and AST23-07950. E.A. and M.-M.M.L. also acknowledge partial support from NASA grant 80NSSC24K0935. C.C.-C. is supported by a Canada Graduate Scholarship - Doctoral (CGS D) from the Natural Sciences and Engineering Research Council of Canada (NSERC). This work used Stampede 2 at TACC through allocation PHY220160 from the Advanced Cyberinfrastructure Coordination Ecosystem: Services & Support (ACCESS) program, which is supported by National Science Foundation grants 21-38259, 21-38286, 21-38307, 21-37603, and 21-38296. The code development that facilitated this study was done on Snellius through the Dutch National Supercomputing Center SURF grants 15220 and 2023/ENW/01498863. S.A. acknowledges the support of NSF grant AST-2009679. R.S.K. and S.C.O.G. acknowledge financial support from the European Research Council via the ERC Synergy Grant “ECOGAL” (project ID 855130), from the Heidelberg Cluster of Excellence (EXC 2181 - 390900948) “STRUCTURES”, funded by the German Excellence Strategy, and from the German Ministry for Economic Affairs and Climate Action in project “MAINN” (funding ID 50002206). The team in Heidelberg also thanks *The Länd* and the German Science Foundation (DFG) for computing resources provided in bwHPC supported by grant INST 35/1134-1 FUGG and for data storage at SDS@hd supported by grant INST 35/1314-1 FUGG. M.-M.M.L. acknowledges Interstellar Institute’s program “II6” and the Paris-Saclay University’s Institut Pascal for hosting discussions that nourished the development of the ideas behind this work.

Part III

SUMMARY & FUTURE WORK

SUMMARY & FUTURE WORK

*One never notices what has been done;
one can only see what remains to be done.*

— Marie Curie

6.1 SUMMARY

This thesis presents modifications I have made to the TORCH star cluster formation framework in order to model the formation of young massive clusters from initial gas clouds as massive as $10^6 M_{\odot}$. The most massive cluster, M6, reached a final mass of $850,000 M_{\odot}$ with $\gtrsim 125,000$ individual star particles being evolved. This is one of the largest star-by-star cluster formation models to date.

The full simulation suite consists of the M4, M5, and M6 cluster models. These were initialized as almost identical clouds with varying masses corresponding to 10^4 , 10^5 , and $10^6 M_{\odot}$. With these novel simulations of YMC formation from natal clouds, we have learned a great deal about how star clusters form and evolve. We were able to compare how cluster formation proceeds differently in low-density, low-mass clouds versus high-density, high-mass clouds. We've found that star cluster formation in GMCs can be a highly efficient process in high density clouds. We've also discovered that sub-cluster dynamics greatly influence the early evolution of young clusters. Resolving sub-clusters in our model revealed a new mechanism for producing runaway stars and early dynamical mass segregation.

In Chapter 3, we found that star formation in giant molecular clouds is rapid and efficient. Within the first free-fall time of the initial cloud, all three models converted at least 30% of the cloud mass into stars. The final SFEs for the M4, M5, and M6 models are $\epsilon_{\star} = 36\%$, 65% , and 85% , respectively. Bound clusters form readily from the dense M5 and M6 clouds, while the M4 cluster is becoming an association. This indicates that the critical density for gravity to overpower stellar feedback is $\Sigma \gtrsim 10^2 M_{\odot} \text{ pc}^{-2}$. This also points to a critical SFE for a cluster to survive gas dispersal of $\epsilon \gtrsim 50\%$, which intuitively requires that most of the gravity is contained in the stellar population rather than the gas. In summary, bound YMCs and GCs easily form from high-mass, dense GMCs. GMCs can naturally reach such density and mass even today, as demonstrated by the Firecracker cloud in the Antennae galaxies. In the early Universe, when galaxies were far more gravitationally unstable, such conditions were even more prevalent.

In Chapter 4, we have identified a new channel for producing runaway stars unbound to their birth cluster. The SCES mechanism occurs when a late-forming sub-cluster falls into the center of mass after most of the cluster has already assembled. The infalling sub-cluster is tidally disrupted, and a fraction of the stars are ejected as tidal tails. The velocity, age, and ejection direction of SCES runaways are strongly correlated, providing a simple identification method for observations. We have identified several promising candidates of SCES runaways, with the group ejected to the north of R136 being the most promising. The sub-cluster assembly history can be probed by the degree of anisotropy in the ejection direction of runaways: more/less anisotropy indicates greater/fewer sub-cluster mergers. The SCES can tighten binaries through ejection, so the ejected binary could undergo a second ejection when its companion explodes as a SN. With the right orbital properties, a two-step SCES-BSS ejection can potentially produce hyper-velocity stars unbound to the Galaxy.

In Chapter 5, we found that young clusters can become mass segregated soon after formation, when the sub-clusters collapse into a single cluster. The collapse creates a dense core with a low dynamical crossing time, allowing the massive stars to rapidly migrate to the center of the cluster. This mechanism can explain the state of mass segregation in clusters younger than the expected dynamical segregation time. The initial collapse of the sub-cluster occurs while star formation is ongoing, which allows massive stars to be formed near the cluster center, i.e., primordially mass segregated. This is because dense star-forming gas will also be pulled in with the collapsing sub-clusters. We also find that though young clusters become mass segregated, this state is highly variable. This can be due to a new massive star forming on the outskirts of the cluster. Most importantly, however, is that massive stars concentrated in the center are more likely to be dynamically ejected as runaways. Mass segregation and dynamical ejections are two competing mechanisms, and early mass segregation has the potential for producing more early OB-type runaways.

The first ever proto-globular clusters have been observed with JWST at $z \sim 10.2_{-0.2}^{+0.2}$, just 460Myr after the Big Bang (Adamo et al., 2024). With masses of $\sim 10^6 M_{\odot}$, half-light radii of $R_{\text{eff}} \sim 1\text{pc}$, and ages between 9 and 35 Myr, these objects have a striking resemblance to our M6 model. This indicates that the mode of star cluster formation presented in this thesis could not only describe the formation of YMCs in the current age, but the formation of young GCs in the early Universe as well. With the combination of cutting-edge telescopes and numerical methods, it seems we are on the precipice of a unifying theory of star cluster formation across cosmic time and space.

6.2 FUTURE WORK

6.2.1 *Towards realistic initial conditions*

The biggest issue that needs addressing in the current models of star cluster formation are the unrealistic initial conditions. Modelling astrophysical processes is exceedingly complicated. To get around this, problems are usually converted into *spherical cows*, i.e., we aim to model a cow, but assume it is spherical and in a vacuum. We have seen the complicated, continuous structure of giant molecular clouds in the Figures of Chapter 1. Yet, we approximate it as an isolated turbulent sphere. The assembly history, turbulent structure, and accretion channels of the cloud gets lost in translation, all of which can drastically alter how the model star cluster forms and evolves. For example, we have seen the significant impact that sub-clustering has in Chapters 4 and 5. Realistic clouds leading to realistic sub-clustering could lead to more undiscovered physics. With new techniques, we can now take GMCs formed self-consistently in galaxy formation models and load it into the TORCH framework as initial conditions. Modelling star clusters forming from these realistic clouds is the most important next step for the field of star cluster formation theory.

6.2.2 *Efficient radiation transfer*

The biggest computational bottleneck in TORCH is the ray-tracing routine. Rays propagating through an AMR grid are split when they cross into a region with higher refinement. The rays are not combined when they cross into a lower refinement region. This leads to a flooding of rays on the grid and greatly raises the computational cost of the ray-tracing step. I plan to replace the ray-tracing module in TORCH with TREERAY (Wünsch et al., 2021) and/or VETTAM (Menon et al., 2022). These radiation transfer schemes are much more efficient, and will allow us to run more models of massive cluster formation with a broad range of parameters.

6.2.3 *Long-term dynamical evolution*

Several questions remain concerning the fate of our modelled clusters. We are interested in constraining the final runaway fraction, the timescale for relaxed mass segregation, and whether the clusters remain bound or eventually disperse dynamically. The short timeframe of our simulations prevents us from determining these properties with certainty. We will investigate this by continuing the cluster's dynamical evolution in a pure N-body code once the gravity from the leftover gas becomes negligible.

With this method, we can resolve the total fraction of dynamical runaway stars. As we don't include primordial binaries in our model, we will approximate the runaway fraction through BSS by counting the number of SNe likely to have a tight binary companion. Furthermore, TORCH can include primordial binaries in initial conditions (Cournoyer-Cloutier et al., 2021), which is necessary to accurately predict the fraction of runaway stars originating via SN. We will use future runs with primordial binaries to confirm the runaway fraction through the BSS as well as determine whether primordial binaries are the progenitors or producers of DES runaways. Then we can predict which of the three runaway mechanisms (DES, BSS, SCES) is the most productive. We can also constrain the timescale for dynamical mass segregation and dispersion in our clusters.

BIBLIOGRAPHY

- ¹A. Adamo, G. Östlin, E. Zackrisson, M. Hayes, R. J. Cumming, and G. Micheva, “Super star clusters in Haro 11: properties of a very young starburst and evidence for a near-infrared flux excess,” *MNRAS* **407**, 870–890 (2010).
- ²A. Adamo, C. Usher, J. Pfeffer, and A. Claeysens, “The ages and metallicities of the globular clusters in the Sparkler,” *MNRAS* **525**, L6–L10 (2023).
- ³A. Adamo, P. Zeidler, J. M. D. Kruijssen, M. Chevance, M. Gieles, D. Calzetti, C. Charbonnel, H. Zinnecker, and M. G. H. Krause, “Star Clusters Near and Far; Tracing Star Formation Across Cosmic Time,” *Space Sci. Rev.* **216**, 69, 69 (2020).
- ⁴A. Adamo et al., “Bound star clusters observed in a lensed galaxy 460 myr after the big bang,” *Nature*, [10.1038/s41586-024-07703-7](https://doi.org/10.1038/s41586-024-07703-7) (2024).
- ⁵A. A. Ali, “The growth of H II regions around massive stars: the role of metallicity and dust,” *MNRAS* **501**, 4136–4147 (2021).
- ⁶R. J. Allison, S. P. Goodwin, R. J. Parker, S. F. Portegies Zwart, R. De Grijs, and M. B. N. Kouwenhoven, “Using the minimum spanning tree to trace mass segregation,” *MNRAS* **395**, 1449–1454 (2009).
- ⁷R. J. Allison, S. P. Goodwin, R. J. Parker, R. de Grijs, S. F. Portegies Zwart, and M. B. N. Kouwenhoven, “Dynamical Mass Segregation on a Very Short Timescale,” *ApJ* **700**, L99–L103 (2009).
- ⁸E. P. Andersson, M.-M. Mac Low, O. Agertz, F. Renaud, and H. Li, “Pre-supernova feedback sets the star cluster mass function to a power law and reduces the cluster formation efficiency,” *A&A* **681**, A28, A28 (2024).
- ⁹S. M. Appel, B. Burkhart, V. A. Semenov, C. Federrath, and A. L. Rosen, “The Effects of Magnetic Fields and Outflow Feedback on the Shape and Evolution of the Density Probability Distribution Function in Turbulent Star-forming Clouds,” *ApJ* **927**, 75, 75 (2022).
- ¹⁰S. J. Arthur, “Wind-Blown Bubbles around Evolved Stars,” in *Diffuse matter from star forming regions to active galaxies - a volume honouring john dyson*, Vol. 1, Astrophysics and Space Science Proceedings (Jan. 2007), p. 183.
- ¹¹S. J. Arthur, J. E. Dyson, and T. W. Hartquist, “Mass-loaded astronomical flows. IV. A time-dependent hydrodynamic model of an observed clumpy wind-blown bubble, RCW 58.,” *MNRAS* **261**, 425–429 (1993).

- ¹²S. J. Arthur, W. J. Henney, and J. E. Dyson, "A coupled hydrodynamic-ionisation model for the clumpy Wolf-Rayet ring nebula RCW 58," *A&A* **313**, 897–908 (1996).
- ¹³K. M. Ashman and S. E. Zepf, "The Formation of Globular Clusters in Merging and Interacting Galaxies," *ApJ* **384**, 50 (1992).
- ¹⁴C. Baczynski, S. C. O. Glover, and R. S. Klessen, "Fervent: chemistry-coupled, ionizing and non-ionizing radiative feedback in hydrodynamical simulations," *MNRAS* **454**, 380–411 (2015).
- ¹⁵J. Ballesteros-Paredes, L. W. Hartmann, E. Vázquez-Semadeni, F. Heitsch, and M. A. Zamora-Avilés, "Gravity or turbulence? Velocity dispersion-size relation," *MNRAS* **411**, 65–70 (2011).
- ¹⁶F. J. Ballesteros, "New insights into black bodies," *EPL (Europhysics Letters)* **97**, 34008 (2012).
- ¹⁷J. Barnes and P. Hut, "A hierarchical $O(N \log N)$ force-calculation algorithm," *Nature* **324**, 446–449 (1986).
- ¹⁸E. J. Barton, M. J. Geller, and S. J. Kenyon, "Tidally Triggered Star Formation in Close Pairs of Galaxies," *ApJ* **530**, 660–679 (2000).
- ¹⁹M. R. Bate, I. A. Bonnell, and N. M. Price, "Modelling accretion in protobinary systems," *MNRAS* **277**, 362–376 (1995).
- ²⁰A. Blaauw, "On the origin of the O- and B-type stars with high velocities (the "run-away" stars), and some related problems," *Bull. Astron. Inst. Netherlands* **15**, 265 (1961).
- ²¹A. Blaauw and W. W. Morgan, "The Space Motions of AE Aurigae and μ Columbae with Respect to the Orion Nebula," *ApJ* **119**, 625 (1954).
- ²²A. Blaauw, "The O Associations in the Solar Neighborhood," *ARA&A* **2**, 213 (1964).
- ²³N. G. Bochkarev, "X-ray emission from the ring nebula NGC6888," *Nature* **332**, 518–520 (1988).
- ²⁴J. P. Brodie and J. Strader, "Extragalactic Globular Clusters and Galaxy Formation," *ARA&A* **44**, 193–267 (2006).
- ²⁵W. R. Brown, M. J. Geller, and S. J. Kenyon, "MMT Hypervelocity Star Survey. III. The Complete Survey," *ApJ* **787**, 89, 89 (2014).
- ²⁶M. Chevance, M. R. Krumholz, A. F. McLeod, E. C. Ostriker, E. W. Rosolowsky, and A. Sternberg, "The Life and Times of Giant Molecular Clouds," in *Protostars and planets vii*, Vol. 534, edited by S. Inutsuka, Y. Aikawa, T. Muto, K. Tomida, and M. Tamura, *Astronomical Society of the Pacific Conference Series* (July 2023), p. 1.
- ²⁷Y.-H. Chu, M. A. Guerrero, R. A. Gruendl, G. García-Segura, and H. J. Wendker, "Hot Gas in the Circumstellar Bubble S308," *ApJ* **599**, 1189–1195 (2003).

- ²⁸A. Claeysens, A. Adamo, J. Richard, G. Mahler, M. Messa, and M. Dessauges-Zavadsky, “Star formation at the smallest scales: a JWST study of the clump populations in SMACSo723,” *MNRAS* **520**, 2180–2203 (2023).
- ²⁹P. Colella and P. R. Woodward, “The Piecewise Parabolic Method (PPM) for Gas-Dynamical Simulations,” *Journal of Computational Physics* **54**, 174–201 (1984).
- ³⁰P. Colín, E. Vázquez-Semadeni, and G. C. Gómez, “Molecular cloud evolution - V. Cloud destruction by stellar feedback,” *MNRAS* **435**, 1701–1714 (2013).
- ³¹D. Colombo, E. Rosolowsky, A. Duarte-Cabral, A. Ginsburg, J. Glenn, E. Zetterlund, A. K. Hernandez, J. Dempsey, and M. J. Currie, “The integrated properties of the molecular clouds from the JCMT CO(3-2) High-Resolution Survey,” *MNRAS* **483**, 4291–4340 (2019).
- ³²P. Colín, E. Vázquez-Semadeni, and G. C. Gómez, “Molecular cloud evolution – V. Cloud destruction by stellar feedback,” *MNRAS* **435**, 1701–1714 (2013).
- ³³*Correspondance d’hermite et de stieltjes*, Vol. 2 (Gauthier-Villars, 1905), pp. 317–319.
- ³⁴R. Courant, K. Friedrichs, and H. Lewy, “On the Partial Difference Equations of Mathematical Physics,” *IBM Journal of Research and Development* **11**, 215–234 (1967).
- ³⁵C. Cournoyer-Cloutier, A. Tran, S. Lewis, J. E. Wall, W. E. Harris, M.-M. Mac Low, S. L. W. McMillan, S. Portegies Zwart, and A. Sills, “Implementing primordial binaries in simulations of star cluster formation with a hybrid MHD and direct N-body method,” *MNRAS* **501**, 4464–4478 (2021).
- ³⁶C. Cournoyer-Cloutier et al., “Early evolution and three-dimensional structure of embedded star clusters,” *MNRAS* **521**, 1338–1352 (2023).
- ³⁷T. J. Cox, P. Jonsson, R. S. Somerville, J. R. Primack, and A. Dekel, “The effect of galaxy mass ratio on merger-driven starbursts,” *MNRAS* **384**, 386–409 (2008).
- ³⁸P. A. Crowther, O. Schnurr, R. Hirschi, N. Yusof, R. J. Parker, S. P. Goodwin, and H. A. Kassim, “The R136 star cluster hosts several stars whose individual masses greatly exceed the accepted $150M_{\text{Solar}}$ stellar mass limit,” *MNRAS* **408**, 731–751 (2010).
- ³⁹R. Crutcher, C. Heiles, and T. Troland, “Observations of Interstellar Magnetic Fields,” in *Turbulence and magnetic fields in astrophysics*, Vol. 614, edited by E. Falgarone and T. Passot, Lecture Notes in Physics (Springer, Berlin, Heidelberg, 2003), pp. 155–181.

- ⁴⁰R. M. Crutcher, B. Wandelt, C. Heiles, E. Falgarone, and T. H. Troland, "Magnetic Fields in Interstellar Clouds from Zeeman Observations: Inference of Total Field Strengths by Bayesian Analysis," *ApJ* **725**, 466–479 (2010).
- ⁴¹J. E. Dale, I. A. Bonnell, C. J. Clarke, and M. R. Bate, "Photoionizing feedback in star cluster formation," *MNRAS* **358**, 291–304 (2005).
- ⁴²J. E. Dale, "The modelling of feedback in star formation simulations," *New A Rev.* **68**, 1–33 (2015).
- ⁴³A. Dekel, K. C. Sarkar, Y. Birnboim, N. Mandelker, and Z. Li, "Efficient formation of massive galaxies at cosmic dawn by feedback-free starbursts," *MNRAS* **523**, 3201–3218 (2023).
- ⁴⁴R. L. Dickman, "The ratio of carbon monoxide to molecular hydrogen in interstellar dark clouds.," *ApJS* **37**, 407–427 (1978).
- ⁴⁵B. T. Draine, "Photoelectric heating of interstellar gas.," *ApJS* **36**, 595–619 (1978).
- ⁴⁶B. T. Draine, *Physics of the Interstellar and Intergalactic Medium* (2011).
- ⁴⁷J. E. Drew, M. Monguió, and N. J. Wright, "Proper motions of OB stars in the far Carina Arm," *MNRAS* **508**, 4952–4968 (2021).
- ⁴⁸A. Dubey et al., "Evolution of flash, a multi-physics scientific simulation code for high-performance computing," *The International Journal of High Performance Computing Applications* **28**, 225–237 (2014).
- ⁴⁹J. E. Dyson and T. W. Hartquist, "Astronomical Bubbles with Clumpy Cores and Accelerating Haloes," *Astrophysical Letters and Communications* **28**, 301 (1992).
- ⁵⁰S. L. Ellison, D. R. Patton, L. Simard, and A. W. McConnachie, "Galaxy Pairs in the Sloan Digital Sky Survey. I. Star Formation, Active Galactic Nucleus Fraction, and the Mass-Metallicity Relation," *AJ* **135**, 1877–1899 (2008).
- ⁵¹B. G. Elmegreen and E. Falgarone, "A Fractal Origin for the Mass Spectrum of Interstellar Clouds," *ApJ* **471**, 816 (1996).
- ⁵²K. L. Emig et al., "Super Star Clusters in the Central Starburst of NGC 4945," *ApJ* **903**, 50, 50 (2020).
- ⁵³I. Evans Neal J. et al., "The Spitzer c2d Legacy Results: Star-Formation Rates and Efficiencies; Evolution and Lifetimes," *ApJS* **181**, 321–350 (2009).
- ⁵⁴S. M. Fall, "Relations between the Luminosity, Mass, and Age Distributions of Young Star Clusters," *ApJ* **652**, 1129–1132 (2006).
- ⁵⁵S. M. Fall, R. Chandar, and B. C. Whitmore, "The Age Distribution of Massive Star Clusters in the Antennae Galaxies," *ApJ* **631**, L133–L136 (2005).

- ⁵⁶S. M. Fall and Q. Zhang, “Dynamical Evolution of the Mass Function of Globular Star Clusters,” *ApJ* **561**, 751–765 (2001).
- ⁵⁷J. P. Farias, S. S. R. Offner, M. Y. Grudić, D. Guszejnov, A. L. Rosen, and The Starforge Team, “Stellar populations in STARFORGE: The origin and evolution of star clusters and associations,” *MNRAS*, [10.1093/mnras/stad3609](https://doi.org/10.1093/mnras/stad3609) (2023).
- ⁵⁸C. Federrath, “Inefficient star formation through turbulence, magnetic fields and feedback,” *MNRAS* **450**, 4035–4042 (2015).
- ⁵⁹C. Federrath, R. Banerjee, P. C. Clark, and R. S. Klessen, “Modeling collapse and accretion in turbulent gas clouds: implementation and comparison of sink particles in amr and sph,” *ApJ* **713**, 269 (2010).
- ⁶⁰C. Federrath, R. Banerjee, P. C. Clark, and R. S. Klessen, “Modeling Collapse and Accretion in Turbulent Gas Clouds: Implementation and Comparison of Sink Particles in AMR and SPH,” *ApJ* **713**, 269–290 (2010).
- ⁶¹G. B. Field, D. W. Goldsmith, and H. J. Habing, “Cosmic-Ray Heating of the Interstellar Gas,” *ApJ* **155**, L149 (1969).
- ⁶²M. K. Finn, K. E. Johnson, C. L. Brogan, C. D. Wilson, R. Indebetouw, W. E. Harris, J. Kamenetzky, and A. Bemis, “New Insights into the Physical Conditions and Internal Structure of a Candidate Proto-globular Cluster,” *ApJ* **874**, 120, 120 (2019).
- ⁶³B. Fryxell, K. Olson, P. Ricker, F. X. Timmes, M. Zingale, D. Q. Lamb, P. MacNeice, R. Rosner, J. W. Truran, and H. Tufo, “FLASH: An Adaptive Mesh Hydrodynamics Code for Modeling Astrophysical Thermonuclear Flashes,” *ApJs* **131**, 273–334 (2000).
- ⁶⁴M. S. Fujii, K. Hattori, L. Wang, Y. Hirai, J. Kumamoto, Y. Shimajiri, and T. R. Saitoh, “SIRIUS Project - V. Formation of off-centre ionized bubbles associated with Orion Nebula Cluster,” *MNRAS* **514**, 43–54 (2022).
- ⁶⁵M. S. Fujii and S. Portegies Zwart, “The Origin of OB Runaway Stars,” *Science* **334**, 1380 (2011).
- ⁶⁶M. S. Fujii, T. R. Saitoh, Y. Hirai, and L. Wang, “SIRIUS project. III. Star-by-star simulations of star cluster formation using a direct N-body integrator with stellar feedback,” *PASJ* **73**, 1074–1099 (2021).
- ⁶⁷M. S. Fujii, L. Wang, Y. Hirai, Y. Shimajiri, J. Kumamoto, and T. Saitoh, “SIRIUS Project - IV. The formation history of the Orion Nebula Cluster driven by clump mergers,” *MNRAS* **514**, 2513–2526 (2022).
- ⁶⁸M. S. Fujii, L. Wang, A. Tanikawa, Y. Hirai, and T. R. Saitoh, “Simulations predict intermediate-mass black hole formation in globular clusters,” *arXiv e-prints*, [arXiv:2406.06772](https://arxiv.org/abs/2406.06772), [arXiv:2406.06772](https://arxiv.org/abs/2406.06772) (2024).

- ⁶⁹M. Fujii, M. Iwasawa, Y. Funato, and J. Makino, "BRIDGE: A Direct-Tree Hybrid N-Body Algorithm for Fully Self-Consistent Simulations of Star Clusters and Their Parent Galaxies," *PASJ* **59**, 1095 (2007).
- ⁷⁰H. Fukushima and H. Yajima, "Radiation hydrodynamics simulations of massive star cluster formation in giant molecular clouds," *MNRAS* **506**, 5512–5539 (2021).
- ⁷¹D. Galli and M. Padovani, "Cosmic-ray heating of molecular cloud cores," *PoS CRISM2014*, 030 (2015).
- ⁷²R. Galván-Madrid et al., "MUSCLE W49: A Multi-Scale Continuum and Line Exploration of the Most Luminous Star Formation Region in the Milky Way. I. Data and the Mass Structure of the Giant Molecular Cloud," *ApJ* **779**, 121, 121 (2013).
- ⁷³S. Geen, J. D. Soler, and P. Hennebelle, "Interpreting the star formation efficiency of nearby molecular clouds with ionizing radiation," *MNRAS* **471**, 4844–4855 (2017).
- ⁷⁴M. Gennaro, S. P. Goodwin, R. J. Parker, R. J. Allison, and W. Brandner, "Hierarchical formation of Westerlund 1: a collapsing cluster with no primordial mass segregation?" *MNRAS* **472**, 1760–1769 (2017).
- ⁷⁵M. P. Geyer and A. Burkert, "The effect of gas loss on the formation of bound stellar clusters," *MNRAS* **323**, 988–994 (2001).
- ⁷⁶D. R. Gies and C. T. Bolton, "The Binary Frequency and Origin of the OB Runaway Stars," *ApJS* **61**, 419 (1986).
- ⁷⁷P. Girichidis, S. S. R. Offner, A. G. Kritsuk, R. S. Klessen, P. Hennebelle, J. M. D. Kruijssen, M. G. H. Krause, S. C. O. Glover, and M. Padovani, "Physical Processes in Star Formation," *Space Sci. Rev.* **216**, 68, 68 (2020).
- ⁷⁸O. Gnat and G. J. Ferland, "Ion-by-ion Cooling Efficiencies," *ApJS* **199**, 20, 20 (2012).
- ⁷⁹S. K. Godunov and I. Bohachevsky, "Finite difference method for numerical computation of discontinuous solutions of the equations of fluid dynamics," *Matematičeskij sbornik* **47(89)**, 271–306 (1959).
- ⁸⁰P. F. Goldsmith, "Molecular Depletion and Thermal Balance in Dark Cloud Cores," *ApJ* **557**, 736–746 (2001).
- ⁸¹G. C. Gómez and E. Vázquez-Semadeni, "Filaments in Simulations of Molecular Cloud Formation," *ApJ* **791**, 124, 124 (2014).
- ⁸²S. P. Goodwin, A. P. Whitworth, and D. Ward-Thompson, "Simulating star formation in molecular cloud cores. I. The influence of low levels of turbulence on fragmentation and multiplicity," *A&A* **414**, 633–650 (2004).

- ⁸³K. Grisdale, O. Agertz, F. Renaud, and A. B. Romeo, “Physical properties and scaling relations of molecular clouds: the effect of stellar feedback,” *MNRAS* **479**, 3167–3180 (2018).
- ⁸⁴M. Y. Grudić, D. Guszejnov, P. F. Hopkins, A. Lamberts, M. Boylan-Kolchin, N. Murray, and D. Schmitz, “From the top down and back up again: star cluster structure from hierarchical star formation,” *MNRAS* **481**, 688–702 (2018).
- ⁸⁵M. Y. Grudić, D. Guszejnov, P. F. Hopkins, S. S. R. Offner, and C.-A. Faucher-Giguère, “STARFORGE: Towards a comprehensive numerical model of star cluster formation and feedback,” *MNRAS* **506**, 2199–2231 (2021).
- ⁸⁶M. Y. Grudić, P. F. Hopkins, C.-A. Faucher-Giguère, E. Quataert, N. Murray, and D. Kereš, “When feedback fails: the scaling and saturation of star formation efficiency,” *MNRAS* **475**, 3511–3528 (2018).
- ⁸⁷M. Y. Grudić, P. F. Hopkins, E. J. Lee, N. Murray, C.-A. Faucher-Giguère, and L. C. Johnson, “On the nature of variations in the measured star formation efficiency of molecular clouds,” *MNRAS* **488**, 1501–1518 (2019).
- ⁸⁸M. Y. Grudić, P. F. Hopkins, C.-A. Faucher-Giguère, E. Quataert, N. Murray, and D. Kereš, “When feedback fails: the scaling and saturation of star formation efficiency,” *MNRAS* **475**, 3511–3528 (2018).
- ⁸⁹D. Guszejnov, M. Y. Grudić, P. F. Hopkins, S. S. R. Offner, and C.-A. Faucher-Giguère, “STARFORGE: the effects of protostellar outflows on the IMF,” *MNRAS* **502**, 3646–3663 (2021).
- ⁹⁰D. Guszejnov, M. Y. Grudić, S. S. R. Offner, C.-A. Faucher-Giguère, P. F. Hopkins, and A. L. Rosen, “Effects of the environment and feedback physics on the initial mass function of stars in the STARFORGE simulations,” *MNRAS* **515**, 4929–4952 (2022).
- ⁹¹D. Guszejnov, C. Markey, S. S. R. Offner, M. Y. Grudić, C.-A. Faucher-Giguère, A. L. Rosen, and P. F. Hopkins, “Cluster assembly and the origin of mass segregation in the STARFORGE simulations,” *MNRAS* **515**, 167–184 (2022).
- ⁹²H. J. Habing, “The interstellar radiation density between 912 Å and 2400 Å,” *19*, 421 (1968).
- ⁹³A. Hacar, S. E. Clark, F. Heitsch, J. Kainulainen, G. V. Panopoulou, D. Seifried, and R. Smith, “Initial Conditions for Star Formation: a Physical Description of the Filamentary ISM,” in *Protostars and planets vii*, Vol. 534, edited by S. Inutsuka, Y. Aikawa, T. Muto, K. Tomida, and M. Tamura, Astronomical Society of the Pacific Conference Series (July 2023), p. 153.
- ⁹⁴M. M. Hanson, I. D. Howarth, and P. S. Conti, “The Young Massive Stellar Objects of M17,” *ApJ* **489**, 698–718 (1997).

- ⁹⁵Y. Harayama, F. Eisenhauer, and F. Martins, “The Initial Mass Function of the Massive Star-forming Region NGC 3603 from Near-Infrared Adaptive Optics Observations,” *ApJ* **675**, 1319–1342 (2008).
- ⁹⁶W. E. Harris and M. Reina-Campos, “JWST photometry of globular cluster populations in Abell 2744 at $z = 0.3$,” *MNRAS* **526**, 2696–2708 (2023).
- ⁹⁷T. W. Hartquist and J. E. Dyson, “Flows in Clumpy Planetary Nebulae,” *Ap&SS* **245**, 263–273 (1996).
- ⁹⁸T. W. Hartquist, J. E. Dyson, M. Pettini, and L. J. Smith, “Mass-loaded astronomical flows - I. General principles and their application to RCW 58.,” *MNRAS* **221**, 715–726 (1986).
- ⁹⁹C.-C. He, M. Ricotti, and S. Geen, “Simulating star clusters across cosmic time - I. Initial mass function, star formation rates, and efficiencies,” *MNRAS* **489**, 1880–1898 (2019).
- ¹⁰⁰C. Heiles, “The interstellar magnetic field,” *ARA&A* **14**, 1–22 (1976).
- ¹⁰¹F. Heitsch, M.-M. Mac Low, and R. S. Klessen, “Gravitational Collapse in Turbulent Molecular Clouds. II. Magnetohydrodynamical Turbulence,” *ApJ* **547**, 280–291 (2001).
- ¹⁰²P. Hennebelle and M. Pérault, “Dynamical condensation in a thermally bistable flow. Application to interstellar cirrus,” *A&A* **351**, 309–322 (1999).
- ¹⁰³M. Heyer and T. M. Dame, “Molecular Clouds in the Milky Way,” *ARA&A* **53**, 583–629 (2015).
- ¹⁰⁴J. Heyl, I. Caiazzo, H. Richer, J. Anderson, J. Kalirai, and J. Parada, “Deep HST Imaging in 47 Tucanae: A Global Dynamical Model,” *ApJ* **850**, 186, 186 (2017).
- ¹⁰⁵L. A. Hillenbrand and L. W. Hartmann, “A Preliminary Study of the Orion Nebula Cluster Structure and Dynamics,” *ApJ* **492**, 540–553 (1998).
- ¹⁰⁶L. A. Hillenbrand, P. Massey, S. E. Strom, and K. M. Merrill, “NGC 6611: A Cluster Caught in the Act,” *AJ* **106**, 1906 (1993).
- ¹⁰⁷J. G. Hills, “Hyper-velocity and tidal stars from binaries disrupted by a massive Galactic black hole,” *Nature* **331**, 687–689 (1988).
- ¹⁰⁸V. H. Hoffmeister, R. Chini, C. M. Scheyda, D. Schulze, R. Watermann, D. Nürnberger, and N. Vogt, “The Stellar Population of M17,” *ApJ* **686**, 310–324 (2008).
- ¹⁰⁹D. Hollenbach and C. F. McKee, “Molecule Formation and Infrared Emission in Fast Interstellar Shocks. III. Results for J Shocks in Molecular Clouds,” *ApJ* **342**, 306 (1989).
- ¹¹⁰R. Hoogerwerf, J. H. J. de Bruijne, and P. T. de Zeeuw, “The Origin of Runaway Stars,” *ApJ* **544**, L133–L136 (2000).

- ¹¹¹C. S. Howard, R. E. Pudritz, and W. E. Harris, “Simulating radiative feedback and star cluster formation in GMCs – II. Mass dependence of cloud destruction and cluster properties,” *MNRAS* **470**, 3346–3358 (2017).
- ¹¹²C. S. Howard, R. E. Pudritz, and W. E. Harris, “A universal route for the formation of massive star clusters in giant molecular clouds,” *Nature Astronomy* **2**, 725–730 (2018).
- ¹¹³F. Hoyle and G. R. A. Ellis, “On the Existence of an Ionized Layer about the Galactic Plane,” *Australian Journal of Physics* **16**, 1 (1963).
- ¹¹⁴M. Iwasawa, D. Namekata, K. Nitadori, K. Nomura, L. Wang, M. Tsubouchi, and J. Makino, “Accelerated FDPS: Algorithms to use accelerators with FDPS,” *PASJ* **72**, 13, 13 (2020).
- ¹¹⁵M. Iwasawa, A. Tanikawa, N. Hosono, K. Nitadori, T. Muranushi, and J. Makino, “Implementation and performance of FDPS: a framework for developing parallel particle simulation codes,” *PASJ* **68**, 54, 54 (2016).
- ¹¹⁶J. H. Jeans, “The Stability of a Spherical Nebula,” *Philosophical Transactions of the Royal Society of London Series A* **199**, 1–53 (1902).
- ¹¹⁷K. E. Johnson, A. K. Leroy, R. Indebetouw, C. L. Brogan, B. C. Whitmore, J. Hibbard, K. Sheth, and A. S. Evans, “The Physical Conditions in a Pre-super Star Cluster Molecular Cloud in the Antennae Galaxies,” *ApJ* **806**, 35, 35 (2015).
- ¹¹⁸M. K. R. Joung and M.-M. Mac Low, “Turbulent Structure of a Stratified Supernova-driven Interstellar Medium,” *ApJ* **653**, 1266–1279 (2006).
- ¹¹⁹J. Kauffmann, T. Pillai, and P. F. Goldsmith, “Low Virial Parameters in Molecular Clouds: Implications for High-mass Star Formation and Magnetic Fields,” *ApJ* **779**, 185, 185 (2013).
- ¹²⁰Z. Khorrami et al., “High-contrast and resolution near-infrared photometry of the core of R136,” *MNRAS* **503**, 292–311 (2021).
- ¹²¹J.-G. Kim, W.-T. Kim, and E. C. Ostriker, “Modeling UV Radiation Feedback from Massive Stars. II. Dispersal of Star-forming Giant Molecular Clouds by Photoionization and Radiation Pressure,” *ApJ* **859**, 68, 68 (2018).
- ¹²²J.-G. Kim, W.-T. Kim, E. C. Ostriker, and M. A. Skinner, “Modeling uv radiation feedback from massive stars. i. implementation of adaptive ray-tracing method and tests,” *ApJ* **851**, 93 (2017).
- ¹²³T. Kimm, R. Bieri, S. Geen, J. Rosdahl, J. Blaizot, L. Michel-Dansac, and T. Garel, “A Systematic Study of the Escape of LyC and Ly α Photons from Star-forming, Magnetized Turbulent Clouds,” *ApJS* **259**, 21, 21 (2022).

- ¹²⁴R. S. Klessen and A. Burkert, "The Formation of Stellar Clusters: Gaussian Cloud Conditions. I.," *ApJS* **128**, 287–319 (2000).
- ¹²⁵R. S. Klessen and S. C. O. Glover, "Physical Processes in the Interstellar Medium," *Saas-Fee Advanced Course* **43**, 85 (2016).
- ¹²⁶A. Kolmogorov, "The Local Structure of Turbulence in Incompressible Viscous Fluid for Very Large Reynolds' Numbers," *Akademiia Nauk SSSR Doklady* **30**, 301–305 (1941).
- ¹²⁷M. G. H. Krause et al., "The Physics of Star Cluster Formation and Evolution," *Space Sci. Rev.* **216**, 64, 64 (2020).
- ¹²⁸P. Kroupa, "The Initial Mass Function of Stars: Evidence for Uniformity in Variable Systems," *Science* **295**, 82–91 (2002).
- ¹²⁹M. R. Krumholz, C. F. McKee, and J. Bland-Hawthorn, "Star Clusters Across Cosmic Time," *ARA&A* **57**, 227–303 (2019).
- ¹³⁰R.-P. Kudritzki and J. Puls, "Winds from Hot Stars," *ARA&A* **38**, 613–666 (2000).
- ¹³¹M. A. Kuhn, K. V. Getman, and E. D. Feigelson, "The Spatial Structure of Young Stellar Clusters. II. Total Young Stellar Populations," *ApJ* **802**, 60, 60 (2015).
- ¹³²M. A. Kuhn et al., "The Spatial Structure of Young Stellar Clusters. I. Subclusters," *ApJ* **787**, 107, 107 (2014).
- ¹³³C. J. Lada and E. A. Lada, "Embedded Clusters in Molecular Clouds," *ARA&A* **41**, 57–115 (2003).
- ¹³⁴N. Lahén, T. Naab, P. H. Johansson, B. Elmegreen, C.-Y. Hu, and S. Walch, "The Formation of Low-metallicity Globular Clusters in Dwarf Galaxy Mergers," *ApJ* **879**, L18, L18 (2019).
- ¹³⁵N. Lahén, T. Naab, and D. Szécsi, "Star clusters forming in a low-metallicity starburst - rapid self-enrichment by (very) massive stars," *MNRAS* **530**, 645–667 (2024).
- ¹³⁶L. Lancaster, E. C. Ostriker, J.-G. Kim, and C.-G. Kim, "Efficiently Cooled Stellar Wind Bubbles in Turbulent Clouds. I. Fractal Theory and Application to Star-forming Clouds," *ApJ* **914**, 89, 89 (2021).
- ¹³⁷R. B. Larson, "Turbulence and star formation in molecular clouds.," *MNRAS* **194**, 809–826 (1981).
- ¹³⁸R. B. Larson and B. M. Tinsley, "Star formation rates in normal and peculiar galaxies.," *ApJ* **219**, 46–59 (1978).
- ¹³⁹E. J. Lee, M.-A. Miville-Deschênes, and N. W. Murray, "Observational Evidence of Dynamic Star Formation Rate in Milky Way Giant Molecular Clouds," *ApJ* **833**, 229, 229 (2016).
- ¹⁴⁰P. J. T. Leonard and M. J. Duncan, "Runaway Stars from Young Star Clusters Containing Initial Binaries. II. A Mass Spectrum and a Binary Energy Spectrum," *AJ* **99**, 608 (1990).

- ¹⁴¹A. K. Leroy et al., “ALMA Reveals the Molecular Medium Fueling the Nearest Nuclear Starburst,” *ApJ* **801**, 25, 25 (2015).
- ¹⁴²A. K. Leroy et al., “Forming Super Star Clusters in the Central Starburst of NGC 253,” *ApJ* **869**, 126, 126 (2018).
- ¹⁴³S. C. Lewis et al., “Early-forming Massive Stars Suppress Star Formation and Hierarchical Cluster Assembly,” *ApJ* **944**, 211, 211 (2023).
- ¹⁴⁴H. Li, O. Y. Gnedin, and N. Y. Gnedin, “Star Cluster Formation in Cosmological Simulations. II. Effects of Star Formation Efficiency and Stellar Feedback,” *ApJ* **861**, 107, 107 (2018).
- ¹⁴⁵H. Li, M. Vogelsberger, F. Marinacci, and O. Y. Gnedin, “Disruption of giant molecular clouds and formation of bound star clusters under the influence of momentum stellar feedback,” *MNRAS* **487**, 364–380 (2019).
- ¹⁴⁶P. S. Li, A. Myers, and C. F. McKee, “Ambipolar Diffusion Heating in Turbulent Systems,” *ApJ* **760**, 33, 33 (2012).
- ¹⁴⁷Z. Li, A. Dekel, K. C. Sarkar, H. Aung, M. Giavalisco, N. Mandelker, and S. Tacchella, “Feedback-Free Starbursts at Cosmic Dawn: Observable Predictions for JWST,” *A&A*, accepted, 10.1051/0004-6361/202348727 (2024).
- ¹⁴⁸Y. Lin et al., “Cloud Structure of Galactic OB Cluster-forming Regions from Combining Ground- and Space-based Bolometric Observations,” *ApJ* **828**, 32, 32 (2016).
- ¹⁴⁹R. Löhner, “An adaptive finite element scheme for transient problems in CFD,” *Computer Methods in Applied Mechanics and Engineering* **61**, 323–338 (1987).
- ¹⁵⁰C. J. Lonsdale, S. E. Persson, and K. Matthews, “Infrared observations of interacting/merging galaxies.,” *ApJ* **287**, 95–107 (1984).
- ¹⁵¹M.-M. Mac Low and R. S. Klessen, “Control of star formation by supersonic turbulence,” *Rev. Mod. Phys.* **76**, 125–194 (2004).
- ¹⁵²J. Makino and S. J. Aarseth, “On a Hermite Integrator with Ahmad-Cohen Scheme for Gravitational Many-Body Problems,” *PASJ* **44**, 141–151 (1992).
- ¹⁵³B. D. Mason, D. R. Gies, W. I. Hartkopf, J. Bagnuolo William G., T. ten Brummelaar, and H. A. McAlister, “ICCD Speckle Observations of Binary Stars. XIX. an Astrometric/Spectroscopic Survey of O Stars,” *AJ* **115**, 821–847 (1998).
- ¹⁵⁴P. Massey and D. A. Hunter, “Star Formation in R136: A Cluster of O3 Stars Revealed by Hubble Space Telescope Spectroscopy,” *ApJ* **493**, 180–194 (1998).
- ¹⁵⁵J. S. Mathis, W. Ruml, and K. H. Nordsieck, “The size distribution of interstellar grains.,” *ApJ* **217**, 425–433 (1977).

- ¹⁵⁶D. R. Matus Carrillo, M. Fellhauer, T. C. N. Boekholt, A. Stutz, and M. C. B. Morales Inostroza, “Stirred, not shaken: star cluster survival in the slingshot scenario,” *MNRAS* **522**, 4238–4250 (2023).
- ¹⁵⁷C. D. Matzner, “On the Role of Massive Stars in the Support and Destruction of Giant Molecular Clouds,” *ApJ* **566**, 302–314 (2002).
- ¹⁵⁸C. F. McKee and J. P. Ostriker, “A theory of the interstellar medium: three components regulated by supernova explosions in an inhomogeneous substrate.,” *ApJ* **218**, 148–169 (1977).
- ¹⁵⁹C. F. McKee and E. C. Ostriker, “Theory of star formation,” *ARA&A* **45**, 565–687 (2007).
- ¹⁶⁰C. F. McKee and J. C. Tan, “The Formation of Massive Stars from Turbulent Cores,” *ApJ* **585**, 850–871 (2003).
- ¹⁶¹C. F. McKee and J. P. Williams, “The luminosity function of ob associations in the galaxy,” *ApJ* **476**, 144 (1997).
- ¹⁶²S. McMillan, S. Portegies Zwart, A. van Elteren, and A. Whitehead, “Simulations of Dense Stellar Systems with the AMUSE Software Toolkit,” in *Advances in computational astrophysics: methods, tools, and outcome*, Vol. 453, edited by R. Capuzzo-Dolcetta, M. Limongi, and A. Tornambè, Astronomical Society of the Pacific Conference Series (July 2012), p. 129.
- ¹⁶³S. L. W. McMillan, E. Vesperini, and S. F. Portegies Zwart, “A Dynamical Origin for Early Mass Segregation in Young Star Clusters,” *ApJ* **655**, L45–L49 (2007).
- ¹⁶⁴M. V. McSwain, S. M. Ransom, T. S. Boyajian, E. D. Grundstrom, and M. S. E. Roberts, “Runaway Massive Binaries and Cluster Ejection Scenarios,” *ApJ* **660**, 740–746 (2007).
- ¹⁶⁵S. H. Menon, C. Federrath, and M. R. Krumholz, “Outflows driven by direct and reprocessed radiation pressure in massive star clusters,” *MNRAS* **521**, 5160–5176 (2023).
- ¹⁶⁶S. H. Menon, C. Federrath, M. R. Krumholz, R. Kuiper, B. D. Wibking, and M. Jung, “VETTAM: a scheme for radiation hydrodynamics with adaptive mesh refinement using the variable Eddington tensor method,” *MNRAS* **512**, 401–423 (2022).
- ¹⁶⁷S. Mikkola and S. J. Aarseth, “A Slow-down Treatment for Close Binaries,” *Celestial Mechanics and Dynamical Astronomy* **64**, 197–208 (1996).
- ¹⁶⁸S. Mikkola and K. Tanikawa, “Algorithmic regularization of the few-body problem,” *MNRAS* **310**, 745–749 (1999).
- ¹⁶⁹M.-A. Miville-Deschênes, N. Murray, and E. J. Lee, “Physical Properties of Molecular Clouds for the Entire Milky Way Disk,” *ApJ* **834**, 57, 57 (2017).

- ¹⁷⁰T. Miyoshi and K. Kusano, “A multi-state HLL approximate Riemann solver for ideal magnetohydrodynamics,” *Journal of Computational Physics* **208**, 315–344 (2005).
- ¹⁷¹M. Moe and R. Di Stefano, “Mind Your Ps and Qs: The Interrelation between Period (P) and Mass-ratio (Q) Distributions of Binary Stars,” *ApJS* **230**, 15, 15 (2017).
- ¹⁷²T. C. Mouschovias and J. Spitzer L., “Note on the collapse of magnetic interstellar clouds.,” *ApJ* **210**, 326 (1976).
- ¹⁷³T. C. Mouschovias, “Cosmic magnetism and the basic physics of the early stages of star formation,” in *The physics of star formation and early stellar evolution* (Springer Netherlands, Dordrecht, 1991), pp. 61–122.
- ¹⁷⁴N. Murray and M. Rahman, “Star formation in massive clusters via the wilkinson microwave anisotropy probe and the spitzer glimpse survey,” *ApJ* **709**, 424 (2009).
- ¹⁷⁵F. Nakamura and Z.-Y. Li, “Protostellar Turbulence Driven by Collimated Outflows,” *ApJ* **662**, 395–412 (2007).
- ¹⁷⁶S. Oh and P. Kroupa, “Dynamical ejections of massive stars from young star clusters under diverse initial conditions,” *A&A* **590**, A107, A107 (2016).
- ¹⁷⁷S. Oshino, Y. Funato, and J. Makino, “Particle-Particle Particle-Tree: A Direct-Tree Hybrid Scheme for Collisional N-Body Simulations,” *PASJ* **63**, 881 (2011).
- ¹⁷⁸D. E. Osterbrock and G. J. Ferland, *Astrophysics of gaseous nebulae and active galactic nuclei* (2006).
- ¹⁷⁹X. Pang, E. K. Grebel, R. J. Allison, S. P. Goodwin, M. Altmann, D. Harbeck, A. F. J. Moffat, and L. Drissen, “On the Origin of Mass Segregation in NGC 3603,” *ApJ* **764**, 73, 73 (2013).
- ¹⁸⁰R. J. Parker and S. P. Goodwin, “Comparisons between different techniques for measuring mass segregation,” *MNRAS* **449**, 3381–3392 (2015).
- ¹⁸¹F. I. Pelupessy, A. van Elteren, N. de Vries, S. L. W. McMillan, N. Drost, and S. F. Portegies Zwart, “The Astrophysical Multipurpose Software Environment,” *A&A* **557**, A84, A84 (2013).
- ¹⁸²T. Peters, R. Banerjee, R. S. Klessen, and M.-M. Mac Low, “The Interplay of Magnetic Fields, Fragmentation, and Ionization Feedback in High-mass Star Formation,” *ApJ* **729**, 72, 72 (2011).
- ¹⁸³S. Pflanzner and T. Kaczmarek, “The expansion of massive young star clusters - observation meets theory,” *A&A* **559**, A38, A38 (2013).
- ¹⁸⁴J. Pflamm-Altenburg and P. Kroupa, “The two-step ejection of massive stars and the issue of their formation in isolation,” *MNRAS* **404**, 1564–1568 (2010).

- ¹⁸⁵D. J. Pinfield, R. F. Jameson, and S. T. Hodgkin, "The mass of the Pleiades," *MNRAS* **299**, 955–964 (1998).
- ¹⁸⁶J. M. Pittard, T. W. Hartquist, and J. E. Dyson, "Self-similar evolution of wind-blown bubbles with mass loading by hydrodynamic ablation," *A&A* **373**, 1043–1055 (2001).
- ¹⁸⁷Planck Collaboration et al., "Planck intermediate results. XVII. Emission of dust in the diffuse interstellar medium from the far-infrared to microwave frequencies," *A&A* **566**, A55, A55 (2014).
- ¹⁸⁸Plotly Technologies Inc., *Collaborative data science*, Montreal, QC, 2015.
- ¹⁸⁹S. F. Portegies Zwart and F. Verbunt, "Population synthesis of high-mass binaries.," *A&A* **309**, 179–196 (1996).
- ¹⁹⁰S. F. Portegies Zwart, S. L. W. McMillan, and M. Gieles, "Young Massive Star Clusters," *ARA&A* **48**, 431–493 (2010).
- ¹⁹¹S. Portegies Zwart and S. McMillan, *Astrophysical recipes*, 2514-3433 (IOP Publishing, 2018).
- ¹⁹²S. Portegies Zwart et al., "A multiphysics and multiscale software environment for modeling astrophysical systems," *New Astronomy* **14**, 369–378 (2009).
- ¹⁹³A. Poveda, J. Ruiz, and C. Allen, "Run-away Stars as the Result of the Gravitational Collapse of Proto-stellar Clusters," *Boletín de los Observatorios Tonantzintla y Tacubaya* **4**, 86–90 (1967).
- ¹⁹⁴M. S. Povich et al., "The Extended Environment of M17: A Star Formation History," *ApJ* **696**, 1278–1306 (2009).
- ¹⁹⁵M. Preto and S. Tremaine, "A Class of Symplectic Integrators with Adaptive Time Step for Separable Hamiltonian Systems," *AJ* **118**, 2532–2541 (1999).
- ¹⁹⁶D. J. Price and M. R. Bate, "The effect of magnetic fields on star cluster formation," *MNRAS* **385**, 1820–1834 (2008).
- ¹⁹⁷D. Rahner, E. W. Pellegrini, S. C. O. Glover, and R. S. Klessen, "Winds and radiation in unison: a new semi-analytic feedback model for cloud dissolution," *MNRAS* **470**, 4453–4472 (2017).
- ¹⁹⁸D. Rahner, E. W. Pellegrini, S. C. O. Glover, and R. S. Klessen, "WARPFIELD 2.0: feedback-regulated minimum star formation efficiencies of giant molecular clouds," *MNRAS* **483**, 2547–2560 (2019).
- ¹⁹⁹M. C. Ramírez-Tannus, L. Kaper, A. de Koter, F. Tramper, A. Bik, L. E. Ellerbroek, B. B. Ochsendorf, O. H. Ramírez-Agudelo, and H. Sana, "Massive pre-main-sequence stars in M17," *A&A* **604**, A78, A78 (2017).
- ²⁰⁰M. Reggiani, M. Robberto, N. Da Rio, M. R. Meyer, D. R. Soderblom, and L. Ricci, "Quantitative evidence of an intrinsic luminosity spread in the Orion nebula cluster," *A&A* **534**, A83, A83 (2011).

- ²⁰¹M. Reina-Campos and W. E. Harris, “RESCUER: cosmological K-corrections for star clusters,” *MNRAS* **531**, 4099–4107 (2024).
- ²⁰²F. Renaud, F. Bournaud, O. Agertz, K. Kraljic, E. Schinnerer, A. Bolatto, E. Daddi, and A. Hughes, “A diversity of starburst-triggering mechanisms in interacting galaxies and their signatures in CO emission,” *A&A* **625**, A65, A65 (2019).
- ²⁰³F. Renaud, “3 things they don’t tell you about star clusters,” in *Star clusters: from the milky way to the early universe*, Vol. 351, edited by A. Bragaglia, M. Davies, A. Sills, and E. Vesperini (Jan. 2020), pp. 40–46.
- ²⁰⁴F. Renaud, O. Agertz, and M. Gieles, “The origin of the Milky Way globular clusters,” *MNRAS* **465**, 3622–3636 (2017).
- ²⁰⁵T. S. Rice, A. A. Goodman, E. A. Bergin, C. Beaumont, and T. M. Dame, “A Uniform Catalog of Molecular Clouds in the Milky Way,” *ApJ* **822**, 52, 52 (2016).
- ²⁰⁶P. M. Ricker, “A Direct Multigrid Poisson Solver for Oct-Tree Adaptive Meshes,” *ApJS* **176**, 293–300 (2008).
- ²⁰⁷F. Rico-Villas, J. Martín-Pintado, E. González-Alfonso, S. Martín, and V. M. Rivilla, “Super Hot Cores in NGC 253: witnessing the formation and early evolution of super star clusters,” *MNRAS* **491**, 4573–4589 (2020).
- ²⁰⁸E. Rosolowsky, “The Mass Spectra of Giant Molecular Clouds in the Local Group,” *PASP* **117**, 1403–1410 (2005).
- ²⁰⁹E. Sabbi, D. J. Lennon, M. Gieles, S. E. de Mink, N. R. Walborn, J. Anderson, A. Bellini, N. Panagia, R. van der Marel, and J. Maíz Apellániz, “A Double Cluster at the Core of 30 Doradus,” *ApJ* **754**, L37, L37 (2012).
- ²¹⁰E. E. Salpeter, “The Luminosity Function and Stellar Evolution.,” *ApJ* **121**, 161 (1955).
- ²¹¹H. Sana, Y. Momany, M. Gieles, G. Carraro, Y. Beletsky, V. D. Ivanov, G. de Silva, and G. James, “A MAD view of Trumpler 14,” *A&A* **515**, A26, A26 (2010).
- ²¹²H. Sana, S. E. de Mink, A. de Koter, N. Langer, C. J. Evans, M. Gieles, E. Gosset, R. G. Izzard, J. B. Le Bouquin, and F. R. N. Schneider, “Binary Interaction Dominates the Evolution of Massive Stars,” *Science* **337**, 444 (2012).
- ²¹³H. Sana et al., “Southern Massive Stars at High Angular Resolution: Observational Campaign and Companion Detection,” *ApJS* **215**, 15, 15 (2014).
- ²¹⁴H. Sana et al., “The VLT-FLAMES Tarantula Survey. Observational evidence for two distinct populations of massive runaway stars in 30 Doradus,” *A&A* **668**, L5, L5 (2022).

- ²¹⁵D. Seifried, R. Banerjee, R. S. Klessen, D. Duffin, and R. E. Pudritz, "Magnetic fields during the early stages of massive star formation - I. Accretion and disc evolution," *MNRAS* **417**, 1054–1073 (2011).
- ²¹⁶F. J. Selman and J. Melnick, "The central density of R136 in 30 Doradus," *A&A* **552**, A94, A94 (2013).
- ²¹⁷C. M. Simpson, G. L. Bryan, C. Hummels, and J. P. Ostriker, "Kinetic Energy from Supernova Feedback in High-resolution Galaxy Simulations," *ApJ* **809**, 69, 69 (2015).
- ²¹⁸L. J. Smith, M. Pettini, J. E. Dyson, and T. W. Hartquist, "The remarkable kinematics of the WR wind-blown bubble RCW 58.," *MNRAS* **211**, 679–693 (1984).
- ²¹⁹M. C. Sormani, R. G. Trefß, R. S. Klessen, and S. C. O. Glover, "A simple method to convert sink particles into stars," *MNRAS* **466**, 407–412 (2017).
- ²²⁰J. Spitzer Lyman, "Equipartition and the Formation of Compact Nuclei in Spherical Stellar Systems," *ApJ* **158**, L139 (1969).
- ²²¹M. Stoop, A. Derkink, L. Kaper, A. de Koter, C. Rogers, M. C. Ramírez-Tannus, D. Guo, and N. Azatyan, "The early evolution of young massive clusters. II. The kinematic history of NGC 6618/M 17," *A&A* **681**, A21, A21 (2024).
- ²²²M. Stoop et al., *subm.*, 2024.
- ²²³P. A. Strittmatter, "Gravitational collapse in the presence of a magnetic field," *MNRAS* **132**, 359 (1966).
- ²²⁴A. M. Stutz, "Slingshot mechanism for clusters: Gas density regulates star density in the Orion Nebula Cluster (M42)," *MNRAS* **473**, 4890–4899 (2018).
- ²²⁵A. M. Stutz and A. Gould, "Slingshot mechanism in Orion: Kinematic evidence for ejection of protostars by filaments," *A&A* **590**, A2, A2 (2016).
- ²²⁶K.-Y. Su, P. F. Hopkins, C. C. Hayward, X. Ma, M. Boylan-Kolchin, D. Kasen, D. Kereš, C.-A. Faucher-Giguère, M. E. Orr, and C. Wheeler, "Discrete effects in stellar feedback: Individual Supernovae, Hypernovae, and IMF Sampling in Dwarf Galaxies," *MNRAS* **480**, 1666–1675 (2018).
- ²²⁷J. Sun et al., "Molecular Cloud Populations in the Context of Their Host Galaxy Environments: A Multiwavelength Perspective," *AJ* **164**, 43, 43 (2022).
- ²²⁸L. J. Tacconi, R. Genzel, and A. Sternberg, "The Evolution of the Star-Forming Interstellar Medium Across Cosmic Time," *ARA&A* **58**, 157–203 (2020).
- ²²⁹T. M. Tauris, "Maximum speed of hypervelocity stars ejected from binaries.," *MNRAS* **448**, L6–L10 (2015).

- ²³⁰*The restaurant at the end of the universe* (Pan Books, 1980).
- ²³¹M. Trenti, P. Padoan, and R. Jimenez, “The Relative and Absolute Ages of Old Globular Clusters in the LCDM Framework,” *ApJ* **808**, L35, L35 (2015).
- ²³²R. G. Tress, R. J. Smith, M. C. Sormani, S. C. O. Glover, R. S. Klessen, M.-M. Mac Low, and P. C. Clark, “Simulations of the star-forming molecular gas in an interacting M51-like galaxy,” *MNRAS* **492**, 2973–2995 (2020).
- ²³³J. K. Truelove, R. I. Klein, C. F. McKee, I. Holliman John H., L. H. Howell, and J. A. Greenough, “The Jeans Condition: A New Constraint on Spatial Resolution in Simulations of Isothermal Self-gravitational Hydrodynamics,” *ApJ* **489**, L179–L183 (1997).
- ²³⁴J. L. Turner, S. C. Beck, D. J. Benford, S. M. Consiglio, P. T. P. Ho, A. Kovács, D. S. Meier, and J. H. Zhao, “Highly efficient star formation in NGC 5253 possibly from stream-fed accretion,” *Nature* **519**, 331–333 (2015).
- ²³⁵E. Vanzella et al., “Massive star cluster formation under the microscope at $z = 6$,” *MNRAS* **483**, 3618–3635 (2019).
- ²³⁶E. Vanzella et al., “Early Results from GLASS-JWST. VII. Evidence for Lensed, Gravitationally Bound Protoglobular Clusters at $z = 4$ in the Hubble Frontier Field A2744,” *ApJ* **940**, L53, L53 (2022).
- ²³⁷E. Vanzella et al., “High star cluster formation efficiency in the strongly lensed Sunburst Lyman-continuum galaxy at $z = 2.37$,” *A&A* **659**, A2, A2 (2022).
- ²³⁸E. Vanzella et al., “JWST/NIRCam Probes Young Star Clusters in the Reionization Era Sunrise Arc,” *ApJ* **945**, 53, 53 (2023).
- ²³⁹E. Vázquez-Semadeni, G. C. Gómez, A. K. Jappsen, J. Ballesteros-Paredes, and R. S. Klessen, “High- and Low-Mass Star-Forming Regions from Hierarchical Gravitational Fragmentation. High Local Star Formation Rates with Low Global Efficiencies,” *ApJ* **707**, 1023–1033 (2009).
- ²⁴⁰E. Vázquez-Semadeni, A. González-Samaniego, and P. Colín, “Hierarchical star cluster assembly in globally collapsing molecular clouds,” *MNRAS* **467**, 1313–1328 (2017).
- ²⁴¹F. Verbunt and P. Hut, “The Globular Cluster Population of X-Ray Binaries,” in *The origin and evolution of neutron stars*, Vol. 125, edited by D. J. Helfand and J. H. Huang (Jan. 1987), p. 187.
- ²⁴²J. S. Vink, A. de Koter, and H. J. G. L. M. Lamers, “New theoretical mass-loss rates of O and B stars,” *A&A* **362**, 295–309 (2000).
- ²⁴³S. Walch et al., “The SILCC (Simulating the LifeCycle of molecular Clouds) project - I. Chemical evolution of the supernova-driven ISM,” *MNRAS* **454**, 238–268 (2015).

- ²⁴⁴J. E. Wall, M.-M. Mac Low, S. L. W. McMillan, R. S. Klessen, S. Portegies Zwart, and A. Pellegrino, “Modeling of the Effects of Stellar Feedback during Star Cluster Formation Using a Hybrid Gas and N-Body Method,” *ApJ* **904**, 192, 192 (2020).
- ²⁴⁵J. E. Wall, S. L. W. McMillan, M.-M. Mac Low, R. S. Klessen, and S. Portegies Zwart, “Collisional N-body Dynamics Coupled to Self-gravitating Magnetohydrodynamics Reveals Dynamical Binary Formation,” *ApJ* **887**, 62, 62 (2019).
- ²⁴⁶L. Wang, M. Iwasawa, K. Nitadori, and J. Makino, “PETAR: a high-performance N-body code for modelling massive collisional stellar systems,” *MNRAS* **497**, 536–555 (2020).
- ²⁴⁷L. Wang, K. Nitadori, and J. Makino, “A slow-down time-transformed symplectic integrator for solving the few-body problem,” *MNRAS* **493**, 3398–3411 (2020).
- ²⁴⁸R. Weaver, R. McCray, J. Castor, P. Shapiro, and R. Moore, “Interstellar bubbles. II. Structure and evolution,” *ApJ* **218**, 377–395 (1977).
- ²⁴⁹L. Wei, C. A. Theissen, Q. M. Konopacky, J. R. Lu, C.-C. Hsu, and D. Kim, “The 3D Kinematics of the Orion Nebula Cluster. II. Mass-dependent Kinematics of the Inner Cluster,” *ApJ* **962**, 174, 174 (2024).
- ²⁵⁰L. H. Wei, E. Keto, and L. C. Ho, “Two Populations of Molecular Clouds in the Antennae Galaxies,” *ApJ* **750**, 136, 136 (2012).
- ²⁵¹C. Weidner, P. Kroupa, and I. A. D. Bonnell, “The relation between the most-massive star and its parental star cluster mass,” *MNRAS* **401**, 275–293 (2009).
- ²⁵²J. C. Weingartner and B. T. Draine, “Photoelectric Emission from Interstellar Dust: Grain Charging and Gas Heating,” *ApJS* **134**, 263–281 (2001).
- ²⁵³B. C. Whitmore, C. Brogan, R. Chandar, A. Evans, J. Hibbard, K. Johnson, A. Leroy, G. Privon, A. Remijan, and K. Sheth, “ALMA Observations of the Antennae Galaxies. I. A New Window on a Prototypical Merger,” *ApJ* **795**, 156, 156 (2014).
- ²⁵⁴B. C. Whitmore et al., “PHANGS-JWST First Results: Massive Young Star Clusters and New Insights from JWST Observations of NGC 1365,” *ApJ* **944**, L14, L14 (2023).
- ²⁵⁵M. J. C. Wilhelm, S. Portegies Zwart, C. Cournoyer-Cloutier, S. C. Lewis, B. Polak, A. Tran, and M.-M. Mac Low, “Radiation shielding of protoplanetary discs in young star-forming regions,” *MNRAS* **520**, 5331–5353 (2023).
- ²⁵⁶M. G. Wolfire, C. F. McKee, D. Hollenbach, and A. G. G. M. Tielens, “Neutral Atomic Phases of the Interstellar Medium in the Galaxy,” *ApJ* **587**, 278–311 (2003).

- ²⁵⁷M. Wrigge, “X-ray emission from wind blown interstellar bubbles. II. ROSAT PSPC observations of S 308,” *A&A* **343**, 599–607 (1999).
- ²⁵⁸M. Wrigge, H. J. Wendker, and L. Wisotzki, “X-ray emission from wind blown interstellar bubbles I. ROSAT observations of NGC 6888,” *A&A* **286**, 219–230 (1994).
- ²⁵⁹R. Wunsch, S. Walch, F. Dinnbier, D. Seifried, S. Haid, A. Klepitko, A. P. Whitworth, and J. Palouš, “Tree-based solvers for adaptive mesh refinement code FLASH - II: radiation transport module TreeRay,” *MNRAS* **505**, 3730–3754 (2021).
- ²⁶⁰F. Xu et al., “The ALMA Survey of Star Formation and Evolution in Massive Protoclusters with Blue Profiles (ASSEMBLE): Core Growth, Cluster Contraction, and Primordial Mass Segregation,” *ApJS* **270**, 9, 9 (2024).
- ²⁶¹Z. Yan, T. Jerabkova, and P. Kroupa, “The most massive stars in very young star clusters with a limited mass: Evidence favours significant self-regulation in the star formation processes,” *A&A* **670**, A151, A151 (2023).
- ²⁶²M. Zamora-Avilés and E. Vázquez-Semadeni, “An Evolutionary Model for Collapsing Molecular Clouds and their Star Formation Activity. II. Mass Dependence of the Star Formation Rate,” *ApJ* **793**, 84, 84 (2014).
- ²⁶³S. van den Bergh, “How Did Globular Clusters Form?” *ApJ* **559**, L113–L114 (2001).